Spring 2017

Numerical and experimental study of new designs of all-vanadium redox flow batteries for performance improvement

Mohammed Abdulkhabeer Ali Al-yasiri

Department: Mechanical and Aerospace Engineering

NUMERICAL AND EXPERIMENTAL STUDY OF NEW DESIGNS OF ALL-VANADIUM REDOX FLOW BATTERIES FOR PERFORMANCE IMPROVEMENT

By

MOHAMMED ABDULKHABEER ALI AL-YASIRI

A DISSERTATION

Presented to the Faculty of the Graduate School of the

MISSOURI UNIVERSITY OF SCIENCE AND TECHNOLOGY

In Partial Fulfillment of the Requirements for the Degree

DOCTOR OF PHILOSOPHY

in

MECHANICAL ENGINEERING

2017

Approved
Jonghyun Park, Advisor
Kelly Homan
Frank Liou
Cheng Wang
Joseph Guggenberger

PUBLICATION DISSERTATION OPTION

This dissertation contains the following three articles, formatted in the style used by the Missouri University of Science and Technology:

Paper I: Pages 33-78 “Study on Channel Geometry of All-Vanadium Redox Flow Batteries” have been submitted to Journal of Renewable energy.

Paper II: Pages 79-111 “New Single Cell Design of Vanadium Redox Flow Battery” are intended for submission to Applied Energy Journal.

Paper III: Pages 112-139 “Development of a Distributed Vanadium Redox Flow Battery for Transport Systems” are intended for submission to Energy, the international Journal.

ABSTRACT

Energy storage is envisioned as a key part of a renewable energy solution incorporated in a grid that overcomes two critical limits of renewable energy: intermittency and uncertainty. Among various technologies, a vanadium redox flow battery (VRFB) offers a promise because of its unique features such as long cycle life, separation of energy and power ratings, and capability of a deep discharge. The remaining challenges, however, include the limited application due to low energy density and complicated geometries. The complex geometry makes it difficult to optimize the performance and can cause a serious concern about leakage of the liquid. The goal of this dissertation is to resolve these challenges through modeling and experimental studies for newly-designed VRFB. The topic can be divided into three main efforts: flow field optimization by optimizing channels, new design for stability improvement and cost reduction, and a new concept of distributed VRFB.

First, the effects of channel and length on battery performance were investigated based on 3D electrochemical models validated by experimental measurements. Second, to address the drawbacks of traditional VRFB, a new design has been introduced to increase reliability, reduce costs, and ease assembly. This battery has a small number of parts, which can more effectively prevent electrolyte leakage. Based on PVC (polyvinyl chloride) material, it solves the problem caused by electrolyte penetration by replacing existing graphite plate. Third, the development of a new distributed VRFB for transport systems addresses the problem of insufficient power, one of the main challenges of the flow system. This new technology is more efficient for space utilization, equal weight distribution, and fueling like a gasoline vehicle, reducing charge time.

ACKNOWLEDGMENTS

First, I would like to express my sincere gratitude to my academic advisor, Prof. Jonghyun Park, for his mentorship, patience, support, and encouragement during my PhD study. The work that I have done for my PhD would never have been possible without his consistent support and guide throughout my research. I must also thank my sponsor of study, the higher committee for education development in Iraq (HCED), for giving me such a wonderful opportunity of pursing my PhD study in the United States, and for the full financial support and funding during these years. In addition, I would like to appreciate Prof. Terry Bone's effort in the Dept. of Chemistry, who helped me at the very beginning of my research in preparation for the experimental chemical solution and provided all the required facility services.

I would also like to thank my committee members, Prof. Kelly Homan, Prof. Frank Liou, Prof. Cheng Wang, and Prof. Joseph Guggenberger, for their support and appreciation of my research. My acknowledgments as well to all my colleagues in the Advanced Energy Materials and Systems Lab for their trust and friendship, and I would like to say thanks for all the funny stories and memories.

Last and most of all, I really want to extend my deepest appreciation to my parents and siblings for their prayers and continuous support (material and moral) to pursue my dream and work hard for it. Your encouragement and understanding support me to overcome difficulties and continually move forward. Also, I must not forget my wife, her family, and my lovely kids for their endless support and being with me every step of the way.

DEDICATION

To my big family, ***IRAQ.***

To the people and families of those who have martyred and those currently fighting ISIS ‘‘***The Holy Popular Mobilization***’’.

To my family and friends who stood behind me and prayed for me with deep love and affection.

Mohammed

TABLE OF CONTENTS

Page

PAPER

LIST OF ILLUSTRATIONS

Page

SECTION

PAPER I

PAPER II

LIST OF TABLES

Page

SECTION

1. INTRODUCTION

1.1. NEED FOR ENERGY STORAGE

As the global economy expands into new developing markets such as China and India, the consumption of electricity increases exponentially. Currently, the majority of electrical output is generated from the burning of fossil fuels such as coal, oil, and gas [1]. There is a limited amount of fossil fuels on earth and with the ever-increasing demand for energy, eventually the supply will be diminished. In addition to the limited supply, there are a lot of negative aspects of burning fossil fuels for energy in terms of environmental damage. The burning of fossil fuels produces CO_2 and other greenhouse gasses that cause global warming. In order to combat global warming, many countries have begun phasing out energy production based on fossil fuels in order to reduce the amount of greenhouse gasses produced. This has presented researchers with an opportunity to develop new "clean" electrical energy producing technologies to replace current technology based on fossil fuels [2].

Among these clean and renewable energy sources utilized increasingly in recent years are wind, sun, wave, and tides. While the energy production of renewable energy sources is still quite low (less than 1% of total energy consumption), the growth rate is approximately 30% annually [3]. This means that the renewable sources could produce a highly significant percentage of global energy output in the not-so-distant future. One slight downfall of these sources is the dependence on variable factors such as weather and sunlight. These dependencies produce strong intermittency in power production, which

introduces the grid to a highly variable and disruptive electrical feed that causes frequency and voltage instabilities.

The base load, which is the nearly constant amount of power drawn by consumers in non-peak times, is typically produced by coal and nuclear power plants. The additional power required during peak times is produced by power plants that have an easily variable output. A European law designed to encourage renewable energy sources gives grid priority to clean and renewable energy sources, especially if the marginal cost is zero like in the case of the wind and photovoltaic sources [4]. These power sources also have a much smaller output variation time-scale in comparison to traditional power plants, which may have to be completely powered off to adequately adjust output after a large variation in power. In the scenario where base load power plants cannot be turned down, the companies would have to pay grid managers to store the additional power, which would greatly change the current business model. Distributed power generation such as the use of photovoltaic cells on commercial buildings can cause significant problems due to the existing power grid not being designed for distributed sources. The current power grids can become unstable if distributed power sources produce more than 20% of the total power output without technology to compensate [5].

Due to an increase in the presence of distributed and renewable power sources alongside large power plants, the power grid needs to be redesigned in order to allow for better control and more accurate management. Electrical energy storage systems (EESS) are an effective solution that allow excess power to be stored and used when the demand is greater than the output capabilities of active generators. EESS provide energy services such as power quality where EESS have short time-scale in a range of minutes or

seconds. A second energy service is energy management, where EESS contribute to load leveling, power balancing, and peak shaving. An advantage of EESS in both power quality and energy management is the possibility to delay the usage of generated electricity. The appropriate technology of EESS is chosen based on the available power and time of operation. The time scale ranges from less than a second to several hours, with the fastest EESS having a response time of one millisecond and available power on the scale of a kilowatt to gigawatt [5].

1.2. ENERGY STORAGE METHODS

Energy storage requires energy conversion such as potential to kinetic, kinetic to electric, or chemical to electric. The usage of energy generally fluctuates with time, so energy storage is required to increase security and efficiency, especially in applications where there is no access to a constant supply of energy (electric cars, portable devices). Energy storage methods are listed below.

1.2.1. Pumped Hydroelectric Power. Pumped hydroelectric energy storage uses the gravitational energy of water to store energy, where excess energy (during times of low energy demand, or excess energy from distributed sources) is used to pump water from a lower reservoir to an upper reservoir. A schematic of this process is shown in Figure 1.1. At times of high energy demand, water is allowed to flow from the upper reservoir through a turbine to the lower reservoir, which generates electricity. These pumped hydroelectric energy systems have low operating costs with little maintenance and can store and reliably supply large amounts of energy with trip efficiencies up to 80% [6]. The energy stored in water is given by Eq. (1):

$$E = mgh \tag{1}$$

where m is the mass of water, g is the gravitational acceleration, and h is the average height.

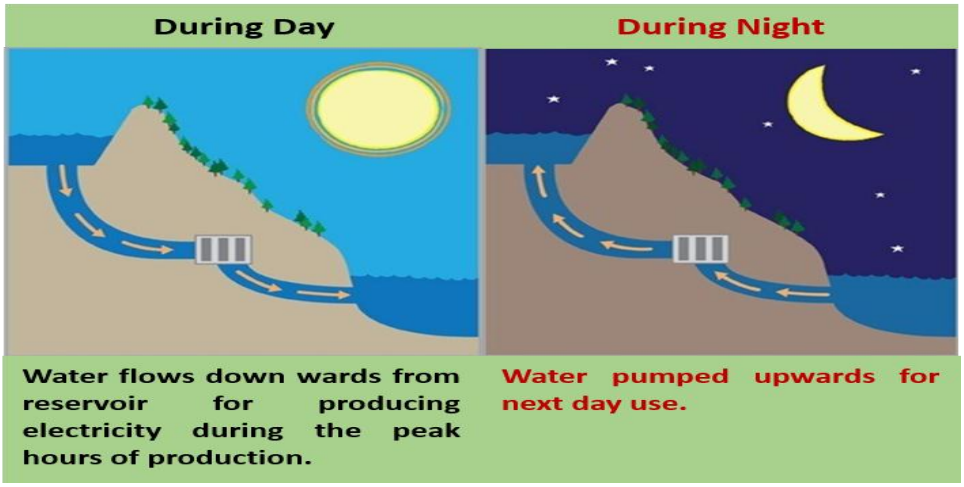

Figure 1.1. Hydroelectric power system during day and night times [7].

1.2.2. Compressed Air. In compressed air storage facilities, excess energy is used to drive a compressor in order to store energy in the compressed gasses. When the energy is needed, the compressed gasses are released through a turbine, which generates electricity. A schematic of this process is shown in Figure 1.2. This energy storage method has low energy density compared to batteries, which makes it not ideal for small applications such as vehicles [8], but it can be easily used in large-scale energy storage systems similar to pumped hydroelectric systems.

The energy stored in compressed air (in kJ/m^3) is approximated by Eq. (2):

$$\frac{E}{v} = 100 * ln\left(\frac{p_f}{p_i}\right) \quad (2)$$

where p_f and p_i are the pressures of gas, E is the energy, and v is the volume.

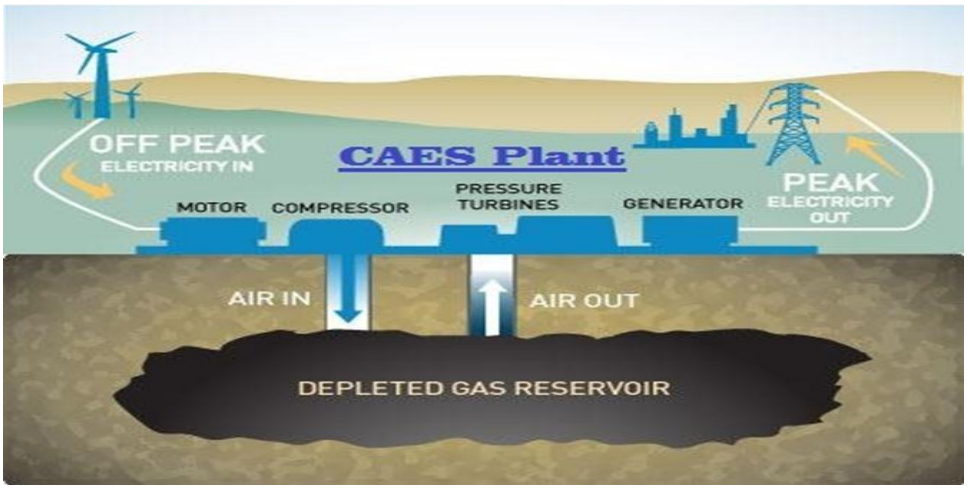

Figure 1.2. Schematic of a compress air storage system [7].

1.2.3. Flywheels. A flywheel is a rotating mechanical system used to store energy in the form of rotational kinetic energy. Excess energy is used to drive a motor that applies torque to the flywheel, causing it to accelerate and store more kinetic energy. Energy can then be released in the form of mechanical energy by allowing the flywheel to apply torque and drive a shaft. A flywheel energy storage system is shown in Figure 1.3. Flywheels are used to supply energy to a system between loading cycles of a discontinuous source. Flywheels can also be used in vehicles to store braking energy to be used at a later time. Flywheels can be compact and used in conjunction with other flywheels to store more energy, and they have a high efficiency of 80–90% [8].

The energy storage in a flywheel system depends on the geometry, mass, and rotational frequency of the device. The energy stored in flywheels can be calculated with Eq. (3):

$$E = \frac{1}{2} I w^2 \tag{3}$$

where $E = 2\pi f$ is the angular velocity and I is the moment of inertia, which depends on the geometry and mass of the device.

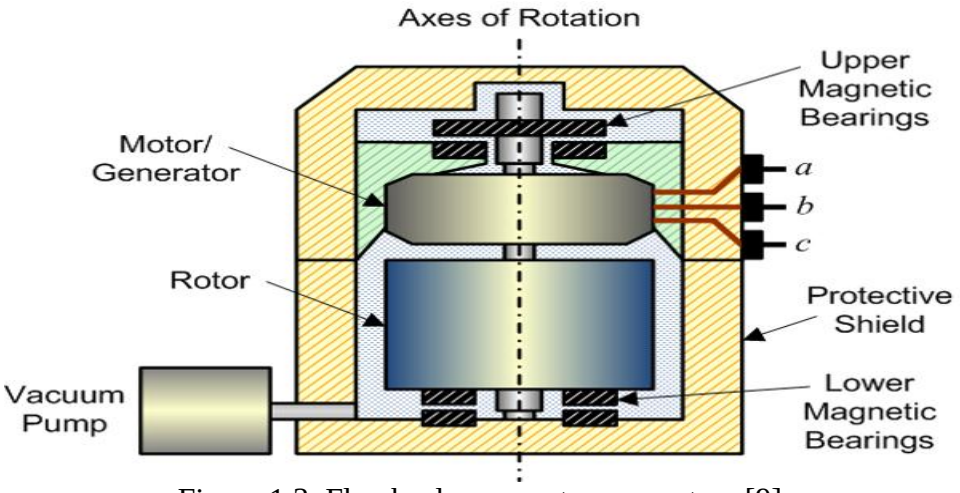

Figure 1.3. Flywheel energy storage system [9].

1.2.4. Superconducting Magnetic Energy Storage (SMES). These systems inject currents into superconducting coils where the current loops indefinitely and creates a magnetic field in which energy is stored. Energy can be released by discharging the coil, which happens in a very short amount of time. Due to technological limitations, this method is not viable for large-scale application, though it has a high energy efficiency of 95% [8]. A basic SMES system is depicted in Figure 1.4. Superconducting magnets have

a critical temperature at which the electrical resistivity is zero. High-temperature superconducting materials are popular because they do not require such a low temperature to obtain zero resistivity, which allows for the use of less advanced equipment. SMES provide direct current (DC), so conversion is required in applications that require alternative current (AC).

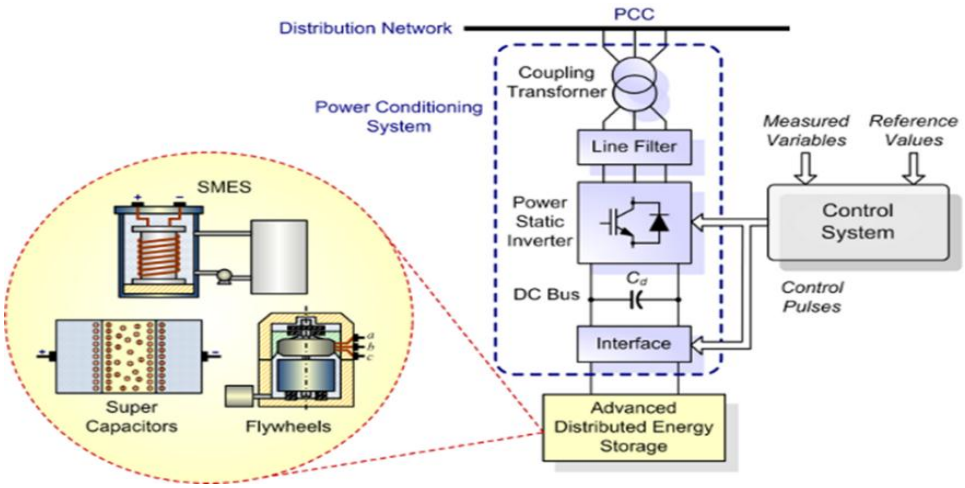

Figure 1.4. Basic structure of SMES device [10].

The energy stored in a coil is given by the following equation:

$$E = \frac{1}{2} L I^2 \tag{4}$$

where L is the inductance of the coil (which depends on the coil dimension, number of turns of wire, and material) and I is the current.

1.2.5. Batteries. Batteries are devices that convert stored chemical energy into electrical energy and contain one or more cell, each having three components: anode, cathode, and electrolyte. They can be rechargeable or non-rechargeable, where non-

rechargeable batteries are suitable for devices that draw little power, such as watches and flashlights. Rechargeable batteries are suitable for mobile systems that draw large amounts of power, such as electric vehicles and laptop computers [8]. The capacity of a battery depends on its chemistry and dimensions. Batteries have a very high energy cost compared to a typical power outlet, where one kWh delivered by non-rechargeable AAA batteries costs $900, which is 8000 times the cost of energy from the outlet. The main advantage of batteries is that they have high energy densities that enable the mobility of significant amounts of energy that can be used to power mobile devices such as cell phones and cameras [8]. Figure 1.5 shows multiple batteries for size comparison.

Figure 1.5. A side by side comparisons of several batteries [11].

1.3. ELECTROCHEMICAL ENERGY STORAGE

Electrochemistry is frequently used for energy storage, especially in mobile applications. Batteries, the most common form of electrochemical energy storage, generally fall into two main categories: primary batteries that produce electrical energy through an irreversible chemical reaction that make them non-rechargeable, and secondary batteries that utilize a reversible chemical reaction, allowing them to be recharged. Batteries can abruptly adjust to changes in power demand and typically have low standby losses and high energy efficiency, especially advanced batteries designed for a specific application. The majority of batteries use toxic chemicals in their electrochemical reactions, so special precautions must be taken regarding their disposal in order to prevent environmental pollution and other adverse effects.

1.3.1. Lead–Acid Batteries. Lead–acid batteries, first invented by Gaston Plantè in 1859, are one of the oldest battery technologies and the first known batteries capable of being recharged. Plantè's battery consisted of alternating layers of lead metal and lead oxide electrodes placed a sulfuric acid electrolyte solution. Since neither lead nor sulfur is particularly expensive, the lead–acid battery is a relatively inexpensive energy storage solution capable of high power quality and UPS [12]. Lead–acid batteries are unable to withstand deep discharges and have short cycle lives, which limits application.

1.3.2. Sodium Sulfur Batteries. Sodium sulfur batteries are still a relevant research topic even though they were first developed in the 1970s. The main advantage of sodium sulfur batteries is that the materials are much less expensive than those used in lithium-ion batteries, and they still have fairly high energy density [13]. These batteries

use liquid sodium and liquid sulfur for the anode and cathode, which require an operating temperature of 300^{0}C. These high operating temperatures cause the battery to be fairly impractical.

1.3.3. Lithium-Ion Batteries. Lithium-ion batteries are popular in applications that require high levels of battery performance, such as electric vehicles and mobile electronics. Lithium-ion batteries have extremely high energy densities that allow them to be much smaller than batteries made of other materials for the same storing amount of energy. This is due to lithium, which is the lightest metallic material that has very high electrochemical potential allowing for cells with specific energies ranging from 100-150 Wh/kg [14]. The main limitation of lithium-ion batteries is that the materials are very expensive, leading to a high cost per kWh and making large-scale lithium-ion storage systems not cost-effective.

1.3.4. Redox Flow Batteries. Redox flow batteries (RFBs) have recently been the topic of extensive research and have very promising prospects for stationary energy storage. This system utilizes redox reactions of fluid electrolytes to provide and store electrochemical energy. The fluid electrolytes are stored in an external tank that allows for large-scale systems and easy expansion. RFB technology is further described in the following section [15].

1.4. FLOW BATTERIES

Flow batteries, as previously mentioned, are currently a popular topic in battery research area, which are relatively new technology. Flow batteries are a very promising solution to large-scale energy storage such as backup power systems and excess energy storage from the power grid due to the electrolyte storage tanks being easily expanded [15]. The battery's charging and discharging is driven by redox reactions between the electrolyte solutions, where the properties of the two solutions and the size of the storage tanks determine energy capacity. The size of the electrodes determines the power capacity of the battery. The electrolyte solutions are pumped from the storage tanks through cell stacks where the redox reactions store or release electrochemical energy. The electrolyte solutions are also pumped through heat exchangers to maintain the optimal operating temperature of the device. A schematic of a flow battery can be found in Figure 1.6.

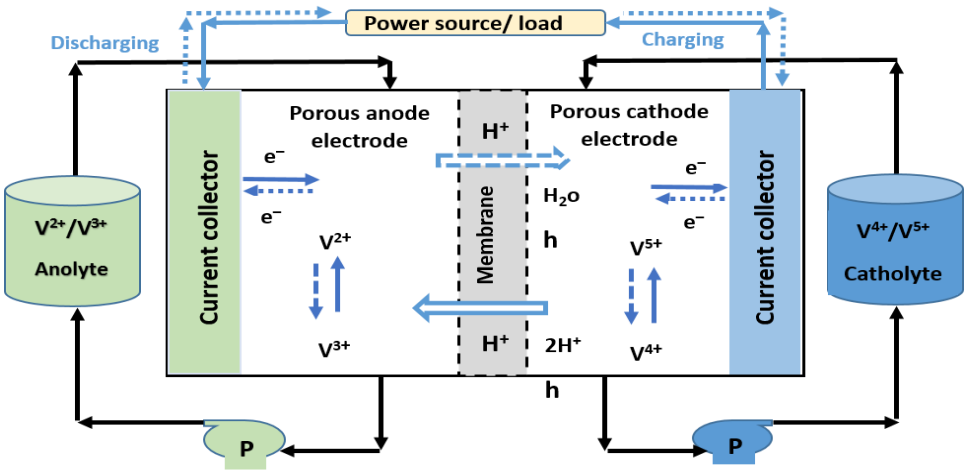

Figure 1.6. Schematic diagram of flow battery.

Table 1.1 shows a comparison of the flow battery and other energy storage systems in terms of parameters such as typical power and duration of discharge [16]. It can be seen that flow batteries are suitable for both medium and large-scale operations with a typical power range of 100 kW–10MW and an energy capacity of up to 100 MWh.

1.4.1. Advantages and Disadvantages. Like all methods of energy storage, flow batteries have advantages and disadvantages, though the benefits greatly outweigh the drawbacks. These advantages and disadvantages are listed below [17].

Table 1.1. Characteristic of flow batteries compared to other storage systems.

Battery type	**Typical Power**	**Typical Energy**	**Typical duration discharge**	**Maturity**
Batteries (lead-acid, NiCd, NiMH, Li-ion)	1–500 kW	MWh–100 MWh	1 h–8 h	Mature
Flywheels	500 kW–1 MW	100 kWh–100 MWh	< 5 minutes	Mature
Pumped hydro	100–4000 MW	500 MW–15 GWh	4–12 h	Mature
CAES	25–3000 MW	200 MWh–10 GWh	1–20 hours	Developed, the first generation demonstrated
NaS	1 MW	1 MWh	1 hour	Developed, commercially available
SMES	10 kW–10 MW		1–30 minutes	Developed, not commercial yet
Supercapacitors	< 250 kW	10 kWh–1 MWh	< 1 minute	Developed
Flow batteries	100 kW–10 MW	1–100 MWh	10 hours	Developed, stage of demonstration projects
Hydrogen storage	10 MW	unlimited	> 5 hours	Developing

1.4.1.1. Advantages. Flow batteries have the following advantages:

- Flexibility and scalability. The power capacity (which depends on the size of electrodes), and the energy capacity (which depends on the size of the external storage tanks) of flow batteries are independent, which allows the design to meet the specific needs of applications.
- Durability and stability. The electrodes only collect current and are not involved in chemical reactions.
- High round-trip efficiency.
- High depth of discharge (DOD).
- Long durability. Because RFBs operate by changing the valence of the metal ion, the components of the electrolyte solution are not consumed.
- Fast responsiveness (small electrical time constant ~ [ms]).
- Reduced environmental impact.
- Long standby periods on full discharge without ill effects.
- Rapid refueling by solution exchange if needed.
- Low maintenance.

1.4.1.2. Disadvantages. Flow batteries have some disadvantages too:

- Low power and energy density (10–50 Wh/kg) compared to other technologies. This makes them unsuitable for mobile applications.
- Limited range of operating temperature [15–35^{0}C] to avoid solution precipitation.
- Shunt currents, due to the conductivity of the electrolyte solution, that cause additional losses and reduce the efficiency.

1.4.2. Types of Flow Batteries. There are three popular types of flow batteries: vanadium redox flow batteries, polysulfide bromide batteries (PSBs), and zinc bromine (ZnBr). PSB is generally used for high power output systems on the scale of multiple megawatts, while VRFB and ZnBr have typical ranges below 1 megawatt. Table 1.2 shows the comparison of those types of flow batteries based on the current status [18].

Table 1.2. Comparison of flow batteries based on current status.

	All-vanadium	**Zinc-bromine**	**PSB**
Typical power range (MW)	< 3	< 1	< 15
Typical size range (MWh)	0.5–5	0.01–5	0–120
Energy density (Wh/liter)	16–33	60–90	20–30
Cycle efficiency [Wh_{out}/Wh_{in}]	70–85%	65–75%	60–75%
Cycle life (cycles)	>12,000	>2000	n/a
Life time (years)	5–10	5–10	15
Stage of development	Demonstration/ commercial units	Demonstration/commercial units	Demonstration
Companies involved	VRB, SEI, Pinnacle, Cellenium	ZBB, Premium Power	TVA, VRB (using Regenesys technology)

1.4.3. Applications of Flow Batteries. Flow batteries are ideal for large-scale energy storage due to being easily expandable, providing high-power outputs and having a large energy capacity. They also have low operating costs; for instance, the battery can be charged and discharged up to 10,000 times without the need to replace the

separation membrane, and the electrodes should never need to be replaced [19]. They are also capable of being rapidly charged, which makes them suitable for applications such as load balancing, storing renewable energy, and peak saving.

Load balancing is the storage of excess energy from the power grid and distributed power generators, which is then released at times of high demand, increasing the reliability of the electrical distribution system [5]. Distributed energy generators such as the wind and solar energy systems have dependencies on variable sources such as the sun or weather, which leads to fluctuations in energy output. Therefore, energy storage is required to supply continuous power. Peak saving is also an application of flow batteries, which is the process of storing energy during non-peak times in order to avoid the higher costs during peak times. Another potential application of flow batteries is the powering of electric vehicles, where flow batteries have an interesting advantage over other battery systems. Flow batteries can be instantly "recharged" by replacing the depleted electrolyte solution with charged solution, which can be compared to filling the gas tank in a combustion-powered vehicle. Flow batteries also may have lower operating costs per kilometer than lithium-ion [20].

1.5. FUNDAMENTAL PRINCIPLES OF VRFB

A simple schematic of a VRFB system during the charge and discharge processes is shown in Figure 1.6. In both charge/discharge processes, the VO^{2+}/VO_{2+} couple is defined as positive, whereas the V^{2+}/V^{3+} couple is defined as negative for convenient explanation in the following sections. The reactions of VRFB systems at the anode and cathode are shown below in Eqs. (5) and (6) respectively. Nitrogen gas is generally circulated through the negative storage loop to prevent V^{2+} from reacting with oxygen. In

an ideal system, there is no consumption of the electrolyte solutions during the charge/discharge cycle, though in reality complicated side reactions occur and change the composition of the electrolyte solutions to an extent. Eqs. (7) and (8) show side reactions of H_2 and O_2 produced from water molecules [21].

$$V^{3+} + e^- \underset{discharge-charge}{\longleftrightarrow} V^{2+} \quad (Negative\ \ half\ side) \tag{5}$$

$$V^{4+} + H_2O \underset{discharge-charge}{\longleftrightarrow} V^{5+} + 2H^+ + e^- \quad (Positive\ half\ side) \tag{6}$$

$$2H_2O + 2e^- \rightarrow H_2 + 2OH^- \quad (Hydrogen\ evolution) \tag{7}$$

$$2H_2O \rightarrow O_2 + 4e^- + 4H^+ \quad (Oxygen\ evolution) \tag{8}$$

During the charging process, H^+ ions are transported from the positive half-cell to the negative half-cell through a hydrogen permeable membrane that separates the positive and negative half-cells, while electrons are externally supplied through a connection to an electrical power source. During the discharging process, H^+ ions pass back through the permeable membrane to the positive half-cell. The hydrogen permeable membrane is composed of a polymeric film that is not electrically conductive. Therefore, the electrons involved in the redox reaction must travel through the bipolar plate and through the external load to get to the cathode. The electrolyte solution is pumped through the positive and negative half-cells from storage tanks in order to provide fresh ions to drive the redox reaction until the desired state of charge is reached.

Energy is carried by the electrolyte solution in the form of dissolved vanadium redox couples, meaning that the stability and concentration of vanadium ions in the sulfuric acid solution greatly impact the performance of VRFBs. All VRFBs employ VO^{2+}/VO_{2+} (V^{4+}/V^{5+}) as the positive electrolyte and V^{2+}/V^{3+} as the negative electrolyte. The supporting electrolytes are generally 1–2 M vanadium ion solutions using 2–5 M sulfuric acid as a solvent [22], where the sulfuric acid increases vanadium solubility and enhances conductivity. It is possible to increase the energy density of VRFBs by increasing the concentration of vanadium, though concentrations above 2 M present issues with vanadium precipitation [23]. The supersaturation of the solution can cause V^{2+}/V^{3+} and V^{4+} solutions to precipitate at low temperatures and V^{5+} solutions will precipitate at elevated temperatures. Therefore, methods must be developed to stabilize highly concentrated vanadium solutions in order to prevent precipitation and increase energy density [23].

The most common materials used in the hydrogen permeable separator membranes are Nafion® 115 and 117. The membranes have an approximate dry thickness of 51 to 183 microns [24] and, ideally, prevent the transfer of electrons and cross-contamination of water molecules and vanadium ions. However, during the charging and discharging processes, some water molecules and vanadium ions are able to pass through the membrane and change the concentration of the electrolyte solutions, causing the battery to be less efficient. Researchers have attempted to reduce cross-contamination by modifying the polymer film with SiO_2, which was successful in reducing cross-contamination and also significantly increased the self-discharge time [25].

The electrode material generally used in VRFBs is porous carbon or graphite due to it being electrically conductive and resistant to chemical and electrochemical corrosion [26-29]. The porous structure increases surface area relative to a solid structure, which helps promote vanadium redox reactions and improves mass transport capabilities by allowing internal space for electrolyte convection. Polyacrylonitrile (PAN) based graphite or carbon felt is typically used as the electrode material in VRFBs due to their wide operation potential range, their stability as both an anode and a cathode, and their high surface areas at relatively low costs [30]. Thermal treatments and the addition of a catalyst have both been shown to enhance the kinetic reversibility of the graphite felt electrode, which reduces activation loss [31]. The addition of Na_2S_x catalyst coatings on the graphite felt electrodes has shown to increase the energy efficiency of the sodium polysulfide/ bromine flow battery (PSB) by approximately 20% compared to uncoated electrodes. Though the kinetics of the reactions inside the VRFB are different than those used by the PSB, the coated electrode will likely also have positive effects in the VRFB [32].

Each half-cell of the flow frame consists of a carbon felt electrode backed by a graphite bipolar plate. The graphite bipolar plate in a cell stack acts as a current collector and connects the electrodes to an external circuit in order to provide power. It is important for the bipolar plate to be impermeable to both the electrolyte solutions and air in order to prevent electrolytes from escaping the system and air penetration. It is also important for the current collector to be resistant to electrolyte corrosion in order to increase the life of the battery and also its reliability. In the flow-by cell architecture, flow channels are engraved in the face of the current collector. This allows for the

electrolyte solution to be more easily distributed throughout the electrodes, but also presents issues in the form of mechanical stability. Because the engraved structures cause stress concentrations and graphite is relatively delicate, the plates must be designed in a way that can withstand the pressure and frictional forces exerted by the flowing electrolyte solution [28, 29]. When designing the electrolyte storage and transport system, certain design considerations must be taken into account; otherwise, the performance of the battery will be greatly affected. In order to prevent atmospheric oxygen from interfering with the redox reactions that drive the battery, the electrolyte solutions must be contained in a sealed and oxygen-free environment. This is especially important for the negative electrolyte solution due to it containing V^{2+}, which is especially sensitive to air oxidization. Nitrogen gas is used to purge the system and establish an inert atmosphere inside the system to prevent unwanted oxidization, which causes capacity loss. The electrolyte solutions use 2–5 M sulfuric acid as a solvent; therefore, the components that come into contact with the solution must be chemically stable. This is an important factor in increasing the life of the battery, where components such as the storage tanks, transport tubing, and pumps must be able to properly contain the electrolyte as well as not contaminate it. Several polymeric materials meet these stability requirements such as polypropylene (PP) and polytetrafluoroethylene (PTFE). During charging and discharging the electrolyte solutions are continuously pumped through loops connecting the storage tanks to the cell stack; therefore, an optimal flow rate must be used in order to balance battery performance and pump pressure loss [28].

1.5.1. Electrochemistry. Vanadium redox flow batteries are driven by redox (reduction-oxidation) reactions. These reactions involve the four oxidation states of vanadium Eqs. (5) and (6), where the species that loses an electron is said to be oxidized and the species that gains an electron is reduced. An oxidizing agent (also called an oxidant) is a species that takes electrons from another substance in order to become reduced [5].

$$oxidant + e^- \rightarrow product \tag{9}$$

A reducing agent (or reductant) gives electrons to other substances and is oxidized in the process.

$$reductant \rightarrow product + e^- \tag{10}$$

A battery is a device that converts chemical energy into electrical energy and vice versa through utilization reactions. Therefore, it is possible to write the formulas of the two simultaneous chemical reactions occurring during the charging and discharging processes of the VRFB. During the discharge, the electrons move from the anolyte to the catholyte by flowing through the external load, as follows:

$$\begin{cases} oxidation & V^{2+} \rightarrow V^{3+} + e^- \\ reduction & V^{5+} + e^- \rightarrow V^{4+} \end{cases} \tag{11}$$
$$V^{5+} + V^{2+} \rightarrow V^{3+} + V^{4+}$$

During the discharge, V^{5+} takes an electron from V^{2+}, while during the charge, the reversed flow of electrons gives the following redox reaction:

$$\begin{cases} reduction & V^{3+} + e^- \rightarrow V^{2+} \\ oxidation & V^{4+} \rightarrow V^{5+} + e^- \end{cases}$$
$$V^{3+} + V^{4+} \rightarrow V^{2+} + V^{5+} \quad (12)$$

Previous equations are simplified versions of the reactions that actually occur in the VRFB, where V^{4+} and V^{5+}exist as oxides. The redox equation must therefore be modified to guarantee the balancing of charges, stoichiometry, and the dissociation of H_2O, as shown in Eq. (5) and Eq. (6).

1.5.2. Nernst Equation. The individual potential of an electrode E_0^s with respect to the standard hydrogen electrode (SHE) measured at standard conditions, i.e., 25ºC and 100 kPa with a concentration of 1M. The standard thermodynamic open circuit voltage of the flow VRFB battery cell can be calculated by summing the standard reduction potentials of the half-cell reactions [5].

For the anode,

$$V^{3+} + e^- \underset{discharge-charge}{\longleftrightarrow} V^{2+} \quad \left(E_{0,neg}^s = -0.255\ \text{V}\ vs.\text{SHE}\right) \quad (13)$$

and for the cathode,

$$V^{4+} + H_2O \underset{discharge-charge}{\longleftrightarrow} V^{5+} + 2H^+ + e^- \left(E_{0,pos}^s = 1.004\ \text{V}\ vs.\ \text{SHE}\right) \quad (14)$$

$$E_0^s = E_{0,pos}^s - E_{0,neg}^s = 1.259\ V \quad (15)$$

where the last equation shows the standard potential for the cathode and anode of a VRFB. The relationship of the electrode potential and the operating conditions is given by the Nernst equation when the operating conditions are not standard, where the product ratio of the activity coefficient should be set to 1[5].

$$E = E_0^s + \frac{RT}{F}\left\{\left(\frac{cV^{5+} * (cH^+)^2}{cV^{4+}}\right)_C \left(\frac{cV^{2+}}{cV^{3+}}\right)_A\right\} \quad (16)$$

The equation above can be obtained by considering the thermodynamics. Cell potential can be approximated by examining the Gibbs free energy (which represents the maximum amount of energy that can be obtained from a chemical) in cases where their concentrations of the different species of vanadium are similar relative to one another. Typically, the operating range of the battery does not exceed high charge states, meaning the approximation is acceptable. Therefore, the Nernst equation proves to be a useful relation between standard potential and non-standard operating conditions, which allows the equilibrium voltage to be calculated for any operating condition [5].

1.5.3. Current: The Butler–Volmer Equation. The electrode kinetics and activation overpotential can be understood by starting with some basic principles of chemistry and ending with a comprehensive equation known as the Butler–Volmer equation in a way that considers the thermodynamics of the system and the activation overpotential η_{act} (a detailed explanation can be found in [5]):

$$I = I_o\left[e^{\alpha nF\eta_{act}/RT} - e^{-(1-\alpha)nF\eta_{act}/RT}\right] \qquad [A] \quad (17)$$

where I_o [A] is the exchange current, which is the absolute value of the anodic or cathodic current, and α is the charge transfer coefficient. The charge transfer coefficient is the fraction of interfacial potential that helps lower the activation energy barrier for the electrochemical reaction at the electrode-electrolyte interface [5].

1.5.4. State of Charge. To evaluate the available energy with respect to the maximum stored energy, it is possible to use the state of charge, which is expressed as a ratio between the different vanadium species [5]:

$$SOC = \frac{cV^{2+}}{cV^{2+} + cV^{3+}} = \frac{cV^{5+}}{cV^{4+} + cV^{5+}} \tag{18}$$

This parameter is equal to zero when the battery is completely discharged, and it is equal to one when the battery is completely charged. Since the total concentration of vanadium (cV_t) is equal to the sum of the concentrations of the vanadium species of each electrolyte,

$$cV_t = cV^{2+} + cV^{3+} = cV^{4+} + cV^{5+} \quad [mol/liter] \tag{19}$$

the SOC can be written as

$$SOC = \frac{cV^{2+}}{cV_t} = \frac{cV^{5+}}{cV_t} \tag{20}$$

1.5.5. Cell Voltage and Overpotential. The operating voltage of VRFB cells is dependent on many variables such as operating temperature, operating current density, the degree of reactant crossover, electrolyte flow rate, and membrane conductivity. The performance of any electrochemical device such as VRFB cells is normally characterized by different diagnostic methods to clarify limiting factors (activation, ohmic, or mass transport) in device performance, which are include cycling test, polarization curve, current interruption, and electrochemical impedance spectroscopy measurements [6]. Figure 1.7 shows the main three kinds of loss regions (activation, ohmic, or mass

transport), which are typically quantified using the polarization curve under a range of current densities.

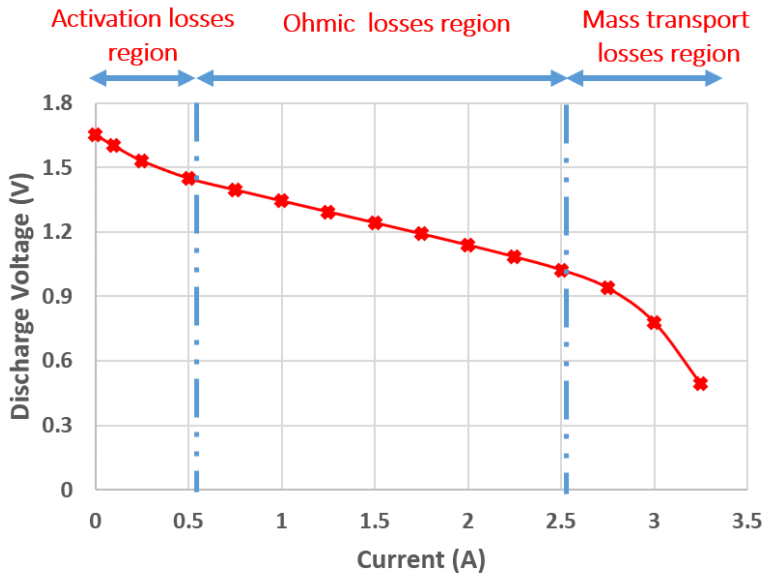

Figure 1.7. Typical polarization curve of a single VRFB cell.

The voltage losses of the cell (overpotential) occur when a current flows into the electrodes, and it is defined as the difference between the equilibrium potential and the potential where the redox reaction occurs. This means that the energy required to force the redox reaction to proceed is given by the overpotential. The equilibrium potential is obtained by the Nernst equation, and the potential that the redox reaction takes place is observed experimentally. Overpotentials are phenomena related only to the electrodes, and since there are many different types, either or both of the electrodes may be affected. The different overpotential losses are listed below.

1.5.5.1. Activation overpotential. Activation overpotential represents the energy needed to start the transferring of charges. Therefore, an applied overpotential causes a change in the equilibrium condition, which leads to electrical currents. The magnitude of this current is limited by the mass transfer of reactants and the rate of electron transfer between the electrodes and the reactants. The magnitude of the overpotential depends on the rate of the redox reaction taking place, where a fast reaction requires lower overpotential than a slow reaction. This overpotential is the energy required to overcome the activation energy barrier of the redox reaction [5]. Therefore, if the concentration of reduced and oxidized species is equal, then the activation barrier is symmetric; however, that is not the case with unequal concentrations. This means that the activation energy required for the cathode and anode reactions is not equal.

1.5.5.2. Concentration overpotential. Concentration overpotential is related to the difference in concentration between the solution near the surface of the electrode and the remaining solution. The electroactive species can have different concentrations near the surface of the electrodes, which causes concentration overpotential. To maintain a steady current, the surface of the electrode must be exposed to fresh solution because this is where the reaction takes place. If the reaction rate is high, the species may not come into contact with the electrode fast enough to maintain a steady reaction and therefore a steady current causes an overpotential [5]. There are three mechanisms that drive the movement of species into the electrolyte solution, and each has specific characteristics and associated velocities. The mechanisms are diffusion, migration, and convection [5].

1.5.5.3. Ohmic and ionic overpotentials. Other overpotentials, which are analytically determinable, are the ohmic and the ionic overpotentials.These overpotentials provide another way to consider the losses caused by the electrical resistance of the carbon felt electrodes, the bipolar plates, and the carbon collector plates. Therefore, the ohmic overpotential, η_{ohm}, can be seen as [5].

$$\eta_{ohm} = R_{ohm}\, I \quad [V] \tag{21}$$

where R_{ohm} is the sum of the resistances, as described above.

Furthermore, the current flow is hindered by the resistance of the electrolyte itself and by the resistance of the membrane. To consider this effect, it is possible to refer to an ionic overpotential η_{ion}, analogously to the ohmic overpotential. The conductivity of the electrolyte is a function of the number of charges and the mobility of the ions dissolved in it. This parameter can therefore be written as

$$\sigma_{ion} = F \sum |z_i| c_i k_i \qquad [S/m] \tag{22}$$

where $F = 96480\ [C/mol]$ is the Faraday constant, z_i is the charge of the ion i, and k_i is the mobility. Also, depending on the size of the ion and its interactions with the other components of the electrolyte, it is possible to write the ionic overpotential as

$$\eta_{ion} = R_{ion}\, I = \left(\frac{1}{\sigma_{ion}} \frac{L}{A} + R_m\right) I \quad [V] \tag{23}$$

where $L\ [m]$ is the length, $A\ [m^2]$ is the cross section, and $R_m\ \ [Ohm]$ is the resistance of the membrane. Given the operating conditions of the cell or the stack, it is possible to determine the operating voltage of the stack, E_{tot}, as

$$E_{tot} = N\left(E - \sum \eta_i\ \right)\quad [V] \tag{24}$$

where N is the number of cells that compose the stack, and i refers to the various overpotentials mentioned above.

1.5.5.4. Other losses of VRFBs. The cross-contamination of vanadium ions and water molecules can cause side reactions and therefore energy losses during the VRFBs cell operation [33]. Vanadium crossover through the separator is mainly caused by the difference in vanadium concentrations in the negative and positive half-cells. Each species of vanadium ion has a different diffusion coefficient through the membrane. Vanadium and hydrogen ions drag water molecules through the membrane during crossover during both charge/discharge and self-discharge cycles. Osmosis is the main force driving water crossover contamination and is responsible for 75% of the water molecules transferring through the membrane [33]. During charge/discharge cycles, additional protons diffuse through the barrier and form an internal electric circuit in the solution.

Side reactions consume electrolyte and current, which impacts the efficiency of the flow battery. Two essential side reactions in VRFBs are oxygen and hydrogen evolutions from water molecules. The hydrogen reaction consumes current from the cathode, while the oxygen reaction consumes current from the anode during the charging process [34]. These side reactions form gas bubbles approximately 25–100 μm in

diameter on the surfaces of the electrodes, which reduces the effective area of the electrodes. Complex side reactions take place in the vanadium electrolyte, and these reactions are complicated due to there being may species of vanadium such as HVO_3 and $H_2VO_4^-$, which exist in the solutions and will react with water and other vanadium species [35].

1.6. TECHNICAL SPECIFICATIONS OF VRFB

The technical specifications of VRFBs, including capacity, energy density, current density, and power density, are presented in the following sections. These quantities show how the basic performance of the battery is measured.

1.6.1. Capacity. Since VRFB is a secondary battery type that can be recharged, the total capacity, the charge density of the anolyte/catholyte, and the state of charge (SOC) are important parameters. The total capacity of an electrolyte to pass electrons is a function of the electroactive species concentration, vanadium solution (C), the number of electrons transferred (n), and the volume of vanadium solution in each tank (V). The capacity Q_p of a VRFB can be expressed as

$$Q_p = nFCV \quad [Ah] \tag{25}$$

1.6.2. Energy Density. Energy density is dependent on the chemistry of the battery and is determined by the solubility of active materials in the electrolyte solution. Energy density has the unit of watt-hour/liter as it is defined as the amount of energy that can be delivered per unit volume of the cell [36]. It is used to determine the appropriate size of a storage tank required to achieve a given energy capacity. In applications where

the availability of space to store electrolyte is limited, the energy density should be as high as possible in order to reduce size.

1.6.3. Current Density. Current density is defined as the available current per surface area of the electrode. The redox chemical reactions take place near the surfaces of the electrodes; therefore, a steady flow of electrolyte solution allows for more reactions to occur. This increases the amount of reactions per unit area and thus results in higher current densities [37].

1.6.4. Power Density. Power density is defined as the maximum amount of power that can be delivered per unit volume and has the unit of watt/liter or watt/kg. Power density is dependent on the chemistry of the battery and determines the sizes of the cell required to meet a specified level of power performance. Increasing the surface area of a cell's electrodes can increase the cell's current at a specified current density and therefore delivers more power for a given cell chemistry [36].

1.7. MULTIPHYSICS MODELS OF VRFB

In last decade, numerous 2D and 3D VRFB modeling studies have successfully integrated the electrochemical reactions and the transport phenomena with computational fluid dynamics (CFD) [5, 21, 34, 38-40]. The electrochemical reactions in a VRFB involve various transport phenomena, including the dissociation and association of molecules, ions, and electrons. The VRFB model involves various governing equations, including flow and electrochemistry physics. Commonly, the set of governing equations used in VRFB model are mass conservation, momentum conservation, energy conservation, species conservation, and charge conservation. In this work, a 3D model of

VRFB is presented by studying different geometric parameters under various operating conditions.

1.8. MOTIVATION AND THESIS OBJECTIVE

There is an increasing need for efficient large-scale electrical energy storage systems to meet the demands of the ever-expanding sources of intermittent renewable energy such as solar and wind farms. Flow batteries are attractive for load leveling and stabilization applications for power companies as well as consumers who require increased capacities, uninterrupted supply, and backup power. VRFBs among other flow battery systems are currently being extensively researched due to their numerous desirable factors such as quick response, deep discharge tolerance, long cycle life, high energy efficiencies of over 80% in large-scale systems, and active thermal management with ultimate goals of improving the performance and reducing the operational costs to help their commercialization.

VRFBs lack flow field design parameters and are expensive, heavy, large, and have less mechanical strength components such as porous flow field graphite plates that make them unable to be used in mobile and distributed power applications due to insufficient power. These issues currently prevent economic feasibility despite the many advantages. This PhD study aims to address these critical challenges through the use of 3D electrochemical models and the design and fabrication of new cell geometries in order to conduct experiments. The fundamental mechanisms responsible for species transport will be explored through the 3D electrochemical modeling of a single cell with the addition of serpentine flow channels. New cell geometries will also be explored through the use of physical experimentation. The overall objective is to better understand flow

battery performance by investigating the impact of channel flow geometry and operating conditions on flow battery performance at a system level through a 3D numerical model. Also, new experimental designs will be utilized in order to solve issues such as cost, size, weight, and limited power, which will increase the commercialization of the VRFB technology.

The main body of this dissertation is comprised of five chapters.

- Chapter 1 summarizes the types of energy storage systems and explains why energy storage systems are needed. VRFBs are an attractive solution for large-scale energy storage in terms of both economics and system capabilities. The fundamental electrochemistry, component materials, and the system design of the VRFB are also discussed.
- Chapter 2 details of the model generation and development of the vanadium flow battery systems. There are numerous physical and chemical phenomena that must be taken into consideration due to electrochemical reactions in flow systems, such as the transport of various species and the association and disassociation of molecules, ions, and electrons. Generally, the convective mass transport increases with flow velocity; therefore, VRFB performance should improve as the flow velocity increases. This can be obtained from changing channel height while keeping the same inlet flow rate (same pumping power). A 3D multiphysics single pass model (which is verified with the fully serpentine flow field model at different ranges of operating conditions, volumetric flow rates, and applied currents) has been developed in order to investigate the impact of channel height and load conditions on the overall battery performance. The effect of flow

channel thickness on the mass flow penetration into the porous layer is also discussed.

- Chapter 3 introduces a new lab-scale single cell battery design that has serpentine flow channels at less cost compared to the traditional design. The design has been fabricated and tested experimentally in our laboratory. The new design is safe (zero electrolyte permeation), easy to assemble (having far fewer components), and more compatible in harsh environment (constructed of PVC material as a flow field plate compared to the brittle and porous graphite flow plate in traditional designs). Tests such as cycling, polarization with a range of currents and flow rates, and electrochemical impedance spectroscopy (EIS) have been conducted in order to compare this design performance with the conventional one, which is normally based on using graphite flow field.
- Chapter 4 develops a new type of distributed flow battery capable of being installed in transport systems such as electric vehicles or any other type of transport system that requires a clean power source. These cells have high aspect ratios and can be looped throughout the transport system in a serpentine configuration. A membrane within the reaction cell has a length substantially equal to the length of the reaction cell such that the surface area of the membrane is maximized relative to the volume of the reaction cell to increase electrical power provided to an electrical load of the transport system.
- Chapter 5 summarizes the major findings of this dissertation study along with a discussion on the future work.

PAPER

I. STUDY ON CHANNEL GEOMETRY OF ALL-VANADIUM REDOX FLOW BATTERIES

ABSTRACT

Flow field in a vanadium redox flow battery, which is determined by flow rate and geometry of flow channel, is one of main components that determine performance of flow battery. Therefore, flow rate and flow channel must be carefully controlled and designed to provide a smooth supply of electrolyte to the area where the electrochemical reactions take place. Through a verified three-dimensional electrochemical model involving fluid motion, we have found that channel height is an important geometric parameter that determines battery performance. We investigated its impact on pressure drop and penetration of the electrolyte into the electrode, and then examined how it ultimately played a role in voltage response, energy efficiency, and battery efficiency. To find the optimal channel shape, various operating parameters, including flow rate, current, and state of charge, were investigated at different channel heights. Overall, low-height cells had better energy and battery efficiency, and could operate relatively low flow rates, but there was a trade-off between improved flow field and pumping loss depending on geometry and loading conditions. A judicious balance between them will be useful for finding optimal design and load conditions for the best performance of flow batteries.

1. INTRODUCTION

Energy storage is envisioned as a key part of a renewable energy solution incorporated in a grid that overcomes two critical limits of renewable energy: intermittency and uncertainty [4, 41-43]. Among various technologies, a vanadium redox flow battery (VRFB) offers a promise because of its unique features that include a long cycle life, separation of energy and power ratings, and capability of a deep discharge [44-51]. As evidence, over the last two decades, large numbers of projects concerning VRFBs have been conducted throughout the world [52-54]. As VRFB system costs continue to lower, the commercialization and industrialization of VRFBs will continue to accelerate [55, 56]. Further, battery performance has been continuously improved by introducing new materials (such as membrane, electrodes, and electrolyte) [57-62] and optimizing the system (battery/stack structure and operating conditions) [29, 63].

One unique feature of a flow battery is, as the name implies, a mass flow is involved in performing its function. Accordingly, there has been significant effort expended to improve the mass transport of electrolytes. In the commonly used flow-through battery architecture (without a flow field), electrolyte is directly supplied to electrodes from the lateral side. However, in this case, the in-plane concentration distribution cannot be uniform, which leads to mass transport polarization in the region far from the inlet. One simple way to minimize this mass transport polarization is to increase the flow rate but, unfortunately, this causes a large parasitic pumping loss. This issue can be addressed by introducing a flow field through a channel between the current collector and the porous electrode. This flow field can distribute the electrolyte with reasonable pumping power [64-68]. The importance of this is well introduced in the fuel

cell state of the art [69-71] and many types of flow fields have been proposed in the literature [72-74]. Here, one critical issue in flow field design is to uniformly distribute the electrolyte on the surface of an electrode to minimize the mass transport polarization. However, this requires a higher flow rate, thereby requiring higher pumping power, which reduces the overall efficiency of a flow battery.

There have been several experiments and numerical studies on the VRFB channel. Most of them, however, focused on comparing different types of channels, including serpentine, interdigital, parallel, and spiral. A recent study of the effects of three different flow fields on the performance of VRFB has shown that a serpentine shaped cell offers the best voltage efficiency, pumping power, and battery efficiency [75]. In [76], the mass transport effects of various flow field designs paired with raw and laser perforated carbon paper electrodes in redox flow batteries were investigated. It has been shown that when coupled with perforated electrodes, performance gains (up to 31%) can be achieved in field designs such as serpentine, parallel, and spiral. On the other hand, interdigitated flow fields are adversely affected by the creation of perforations due to the high permeability ‘channels’ in the electrode. In [77], parallel flow field of a VRFB was selected to describe the distribution of electrolyte solution numerically and experimentally. Further, it was shown that an interdigitated flow field configuration has better performance compared with the serpentine pattern in VRFB systems [78]. Comparing a cell with a serpentine channel to a cell without the flow field through the polarization test showed that the kinetic and mass transfer losses were not significant compared to internal resistance losses for the cell with a serpentine flow field [28]. A number of numerical studies have been conducted by focusing on: improvement of

system efficiency [79]; 3D pore scale model [80]; finding the flow distribution in the channel [81]; impact of single-inlet and multi-inlet flow rate of interdigitated flow field [38]; and energy and battery efficiency of different cell configurations.

Despite considerable prior research, the remaining important questions are how to design the cross section of the flow channel itself and how to determine its length. Apparently, small areas allow more flow to the electrodes at higher flow rates, but also increased pumping power is required. In addition, long channels can provide more reaction sites, but pressure losses increase with increasing length. Furthermore, to maximize battery performance, channel design must be considered simultaneously with flow rate and electric current, since mass transport must be balanced with electrochemical reactions.

In order to address this problem, this paper has developed a three-dimension electrochemical model base on the most detailed models in the literature so far. After verification of the developed model, first, the channel length effect was studied by comparing the single channel and the five serpentine channels. After confirming that the five-channel model and the single-channel model do not significantly differ in battery response, channel height effects have been focused. Three different channel heights of a single channel were considered. The effects of different ranges of applied currents, State of Charge (SOC), and flow rates on pressure drop and penetration of electrolyte into electrodes, and eventually on battery performance were investigated. Although this has critical influences on battery performance, there is no evidence that this has been studied and reported in the literature.

2. EXPERIMENTAL SETUP

A schematic diagram of a fabricated VRFB is shown in Figure 2.1a and its experimental setup is shown in Figure 2.1b. The active area of a cell was 5×5 cm^2. In order to minimize ionic and contact resistances between the membrane and electrode, a "zero-gap" configuration is used, which means that the membrane, electrodes, and current collectors are in direct contact. A Nafion 117 (Ion-Power, Inc.) membrane served as the separator. The electrodes are made of a graphite felt (SGL Technologies GmbH) with an uncompressed thickness of 6mm and a specific resistance of 0.12 Ohm-cm. Graphite plates (Fuel cell store), with machined serpentine flow channels, distribute the electrolyte across the active area of the VRFB, while also serving as the current collectors. PTFE (polytetrafluoroethylene) gaskets are applied between the adjacent cell compartments for sealing and the whole assembly is tightly pressed using 12 bolts and nuts to prevent leakage. The fluid inlets and outlets of the cell are constructed on the side of 10 mm- thick polymer insulators.

An all-vanadium electrolyte is prepared by dissolution of 1.04 M $VOSO_4$ (99.9% purity, Alfa Aesar) in a sulfuric acid solution with a total SO_4^{2-} concentration of 4 M. Both electrolyte reservoirs initially consisted of a solution containing only V^{4+} ion. The positive electrolyte volume is initially 200 mL, twice the negative electrolyte volume. This electrolyte is then charged until V^{4+} is converted to V^{2+} (negative electrode electrolyte) and V^{5+} (positive electrode electrolyte), and subsequently, half of the positive electrolyte solution is removed from its reservoir to make the solution volumes in the anode and cathode equal. Both positive and negative electrolytes are supplied to the cell via two diaphragm pumps (SMART Digital DDA7.5-16AR-PVC/V/C, Grundfos,

Bjerringbro, Germany) from reservoirs, as shown in the experimental set up in Fig. 2.1 (b). Purging of nitrogen into the negative and positive electrolyte reservoirs is done at the beginning, before running a test to exclude the air from the reservoirs, and then the lids are tightened well. All experiments are carried out at room temperature. It is assumed that a battery is fully charged when a current of < 20 mA is observed when the battery is held potentiostatically at 1.7 V.

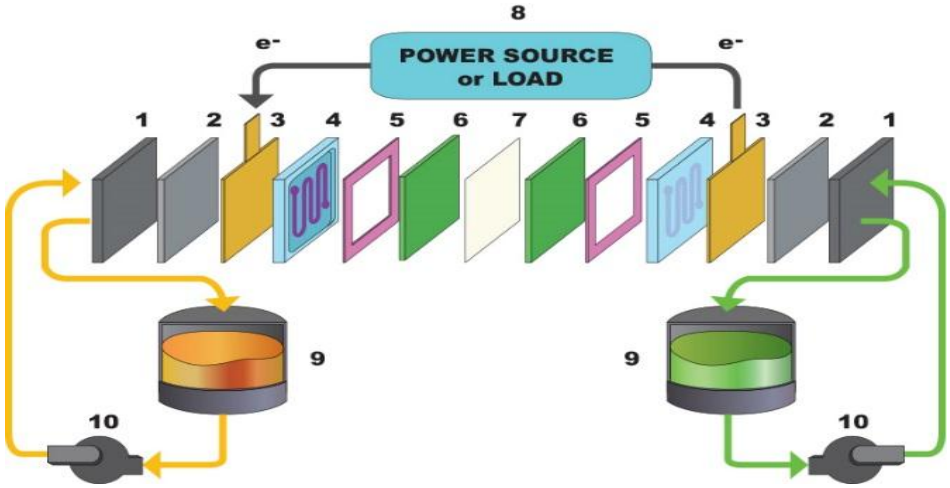

(a)

Figure 2.1. (a) A schematic of a flow cell: (1) end plates, (2) insulators, (3) current collectors, (4) graphite plates with serpentine flow channels, (5) gaskets, (6) porous electrodes, (7) membrane, (8) power source or load, (9) electrolyte tanks, (10) pumps, (b) experimental setup of a VRFB.

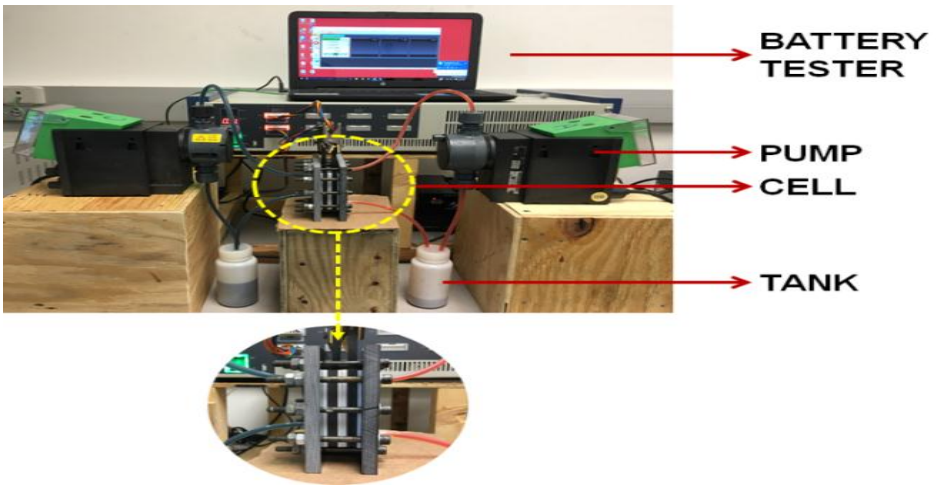

(b)

Figure 2.1. (a) A schematic of a flow cell: (1) end plates, (2) insulators, (3) current collectors, (4) graphite plates with serpentine flow channels, (5) gaskets, (6) porous electrodes, (7) membrane, (8) power source or load, (9) electrolyte tanks, (10) pumps, (b) experimental setup of a VRFB (cont.).

3. MATHEMATICAL MODEL

3.1. GEOMETRY

Two geometric structures, a serpentine channel structure (left in figure) and a single channel path (right in figure) are considered, as shown in Figure 3.1. The entire serpentine channel structure is for studying channel length effect, and it is reduced to one single channel path for studying channel height effect to increase the computational efficiency, after confirming no significant difference in the responses between the two structures. A cell is composed of two flow channels and two porous electrodes for anode and cathode sides, and separator. Three designs of flow single channels of different heights (Ch) are simulated, while all other dimensions remain the same (Table 3.1).

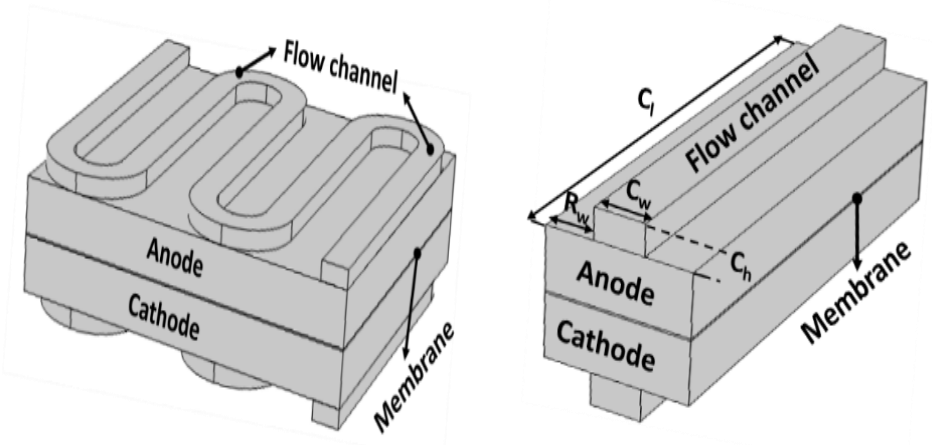

Figure 3.1. A serpentine channel structure (left) and a single channel path (right) of a VRFB.

Table 3.1. Flow field dimensions of the three cells for VRFB models.

Parameters	**Three different cell designs**		
	Cell 1	Cell 2	Cell 3
Channel height (C_h)	1.19 (mm)	1.59 (mm)	1.98 (mm)
Channel length (C_l)	50.00 (mm)	50.00 (mm)	50.00 (mm)
Channel width (C_w)	4.00 (mm)	4.00 (mm)	4.00 (mm)
Rib width (R_w)	7.50 (mm)	7.50 (mm)	7.50 mm)

3.2. MODEL DEVELOPMENT

Several assumptions are made to simplify the model. First, an incompressible fluid is assumed for the electrolyte as the volume change is small. A dilute solution, with liquid water as the dominant species in the electrolyte, is also assumed. The typical concentrations of vanadium species (~1000 mol/m^3) are much lower than water molecule concentration (~55,000 mol/m^3). Also, according to the calculated Reynolds number (Re) for the given channel dimensions and range of flow rates, Re = 86.7 to 2280, so it is reasonable to consider a laminar regime flow. This paper focuses on battery performance with channel structure, not performance degradation, so performance degradation is not considered. That is, the separator can pass only proton ions (H^+) to prevent vanadium ions from crossing with water, and hydrogen and oxygen generation (side reactions) are not considered in this model. In addition, if the reservoir is large enough, a transient process can be treated as a steady state process. This is confirmed by comparing the transient and steady state calculations in the discussion section.

In order to model the flow field, two adjacent regions, a free flow region of the channel and a porous flow region of the electrodes must be considered. For laminar flow,

the flow inside the channel can be represented by the Navier-Stoke (NS) equation with the continuity equation. For the porous electrode, the steady state Brinkman equation for single-phase incompressible flow is used. The details are described in Eqs. (A.1-A.5) in the appendix.

A battery electrode is a porous medium with interconnected pore networks, allowing the flow of electrolyte. The electrochemical reactions occur at the interfaces between the electrolyte and the solid structure. The main reaction in the anode electrode is:

$$V^{3+} + e^- \underset{discharge-charge}{\longleftrightarrow} V^{2+} \quad \left(E^s_{0,neg} = -0.255\ \mathrm{V}\ vs.\mathrm{SHE}\right) \tag{1}$$

In the cathode electrode, the main reaction is

$$V^{4+} + H_2O \underset{discharge-charge}{\longleftrightarrow} V^{5+} + 2H^+ + e^- \left(E^s_{0,pos} = 1.004\ \mathrm{V}\ vs.\mathrm{SHE}\right) \tag{2}$$

where $E^s_{0,neg}$ and $E^s_{0,pos}$ are the standard electrode potentials of anode and cathode electrodes, respectively. Typically, each electrolyte solution is composed of water, sulfuric acid (i.e., H^+, HSO_4^-, and SO_4^-), and charged vanadium species (i.e., V^{2+}, V^{3+}, V^{5+}, and V^{4+}) flowing through the porous graphite electrodes. A steady state mass conservation for each charged species can be formulated through the Nernst–Planck equation. Species conservation equation, which is applied in the whole domain including electrode and channel, can be described as follows [82]:

$$\nabla \cdot \vec{N}_{i,e} = R_i \tag{3}$$

where $\vec{N}$ is the flux of the charged species (species of *i*) in the electrolyte (represented by subscript *e*), and R_i denotes the source term for the species. All the charged species in the electrolyte solution can be applied in Eq. (3), except SO_4^-, which is evaluated from the electroneutrality in the electrolyte solution as follows:

$$\sum_i Z_i C_{i,e} = 0 \tag{4}$$

where $C_{i,e}$ is the species concentration and Z_i is the valence for the species (*i*).

The local reaction current density for both electrodes are expressed by using the Butler-Volmer equations. In literature, many models consider a simple form of Butler-Volmer question without accounting the effect of species transport between the bulk solution and the liquid-solid interface [83]. In the current model, the bulk and surface concentrations are distinguished by considering the mass transport resistance. Details are given in the appendix (Eqs. A-18~A-24).

The separator is designed to prevent cross-over of other species except proton ions to avoid reactant mixing. In separators such as Nafion membranes, fixed sulfonic acid charges are present in local, and remain immobile [84]. Their presence has little effect on the diffusion of mobile sulfonic acid ions, but has an effect on the electric field. For this, the fixed sulfonic acid ions can be treated separately from the mobile sulfonic acid ions. From the electro-neutrality condition, the proton concentration in separators satisfies [84]:

$$C_{H,+} + Z_f C_f = 0 \tag{5}$$

where C_f is the fixed charge site concentration in the membrane and Z_f is the fixed site charge. The value of $C_{H,+}$ is taken as constant in the separator region. Assuming that protons are the only (or dominant) mobile ions, only ionic current exists, and similar to the porous electrode, it is proportional to the flux of proton concentration only. All the parameter values of the separator are listed in Table 3.2.

Table 3.2. Properties of membrane [40].

Symbol	Description	Value and unit	Origin
l_m	Membrane thickness	183 (μm)	Provided by manufacturer
Z_f	Fixed acid concentration	-1	-
C_f	Fixed acid charge	1990 $(mol \cdot m^{-3})$	[85]
$D_{H,+}^m$	Membrane proton diffusion coefficient	3.35×10-9 $(m^2 \cdot s^{-1})$	[86]
σ_m	Electronic conductivity of membrane	24.88 (S $\cdot m^{-1}$)	Calculated

Flow rate has a considerable effect on the pumping power, battery capacity, and efficiency. Battery performance is evaluated by comparing energy efficiency and battery efficiency using various flow rates and current rates. The definitions of energy efficiency, η_E, and battery efficiency, η_B, are defined as below [5]:

$$\eta_E = \frac{E_{disch}}{E_{ch}} \tag{6}$$

$$\eta_B = \frac{P_{disch}^{out} - P_{pump}}{P_{ch}^{in} + P_{pump}} \tag{7}$$

where *E*, *P* are energy and power, the subscripts '*ch'* and *'disch'* represent charging and discharging, respectively. Since input and output power are a function of SOC, efficiency is compared as a function of SOC and an average value is used for overall evaluation. P_{Pump}, the pumping power to supply the electrolyte into VRFBs, is evaluated through pressure drop and electrolyte volumetric flow rate as follows [87]:

$$P_{Pump} = \frac{N_p \,.\mathrm{V_B^0}\,.\,\Delta \mathrm{p}}{\eta_p} \tag{8}$$

where N_p is the number of the utilized pumps, $\mathrm{V_B^0}$ is the provided volumetric flow rate in ml/min, η_p is the pump efficiency ($\eta_p \sim 0.85$), and $\Delta \mathrm{p}$ represents the total pressure drop through the piping and the battery. Large external pipe sizes are assumed so that associated pressure losses are negligible. Thus, only the pressure drops in the porous electrodes are considered.

The governing equations are solved by the COMSOL Multiphysics® package. A Lagrange-quadratic basis is used for all of the simulations. The relative error tolerance is set as 1×10^{-5}.

4. RESULTS

4.1. EFFECT OF NUMBER OF CHANNELS

First, we compared the two geometries shown in Figure 3.1 to investigate the effect of channel length on battery voltage response during discharging at different SOCs, volumetric flow rates, current densities, and channel depths. Figure 4.1 represents the discharge voltage at different SOCs (0.15, 0.55, and 0.95) under different operating conditions and channel heights. Both upper and lower left figures show a mild condition with low flow rate (5 ml/min) and low current density (40 mA/cm^2) while the figures on the right show a severe condition with high flow rate (150 ml/min) and high current density (93 mA/cm^2). The results from different channel height are shown in figures 4.1 (a) and (b) for the lowest and highest channel height, respectively. All the results indicate that there is no significant difference between the single channel and whole serpentine geometry model with a difference less than 0.5%. This is also justifying the sufficiency of using a single model for the channel height study.

4.2. GENERAL BEHAVIOR UNDER DIFFERENT FLOW RATES AND CURRENT DENSITIES

The electrolyte flow rate and current density are two important parameters that determine the overall performance of a VRFB system. A general understanding of the impact of those two key parameters on battery performance is essential to identifying the impact of channel geometry. To understand this, simple galvanostatic discharge simulations are performed with different flow rates from 5 to 150 ml/min and current densities from 40 to 93 mA/cm^2. Figure 4.2 shows the cell voltage responses with different flow rate and current density conditions. The figures 4.2(a) and (b) shows the influence of the flow rate at a constant current density (a: 40 mA/cm^2 and b: 93 mA/cm^2).

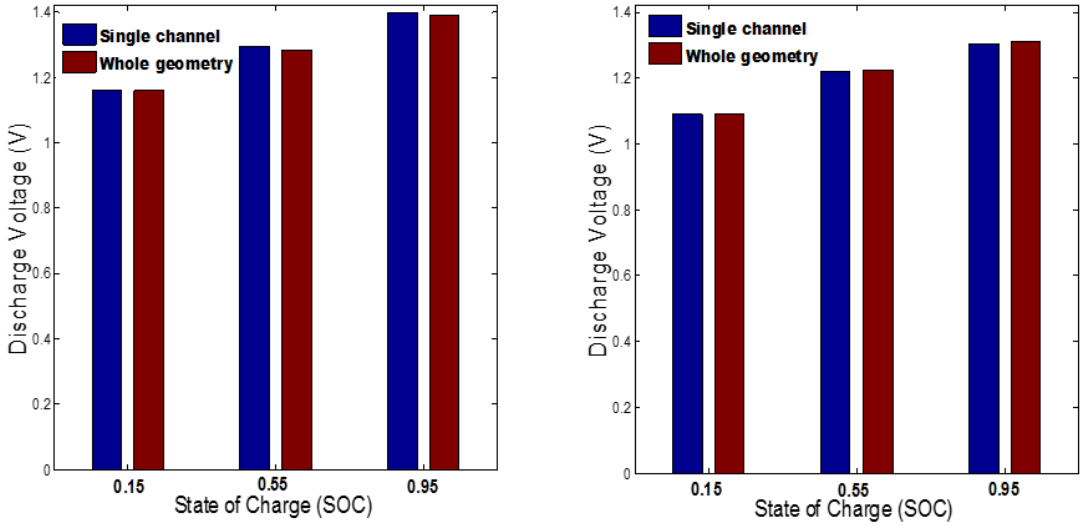

(a)

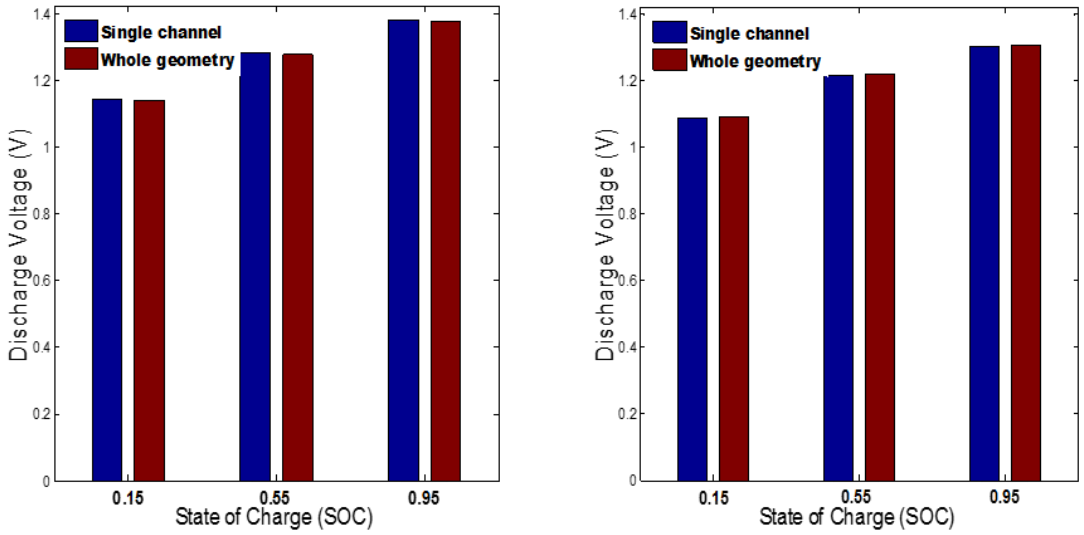

(b)

Figure 4.1. Effect of the single channel pass and whole serpentine geometry models on discharge voltage at different operating conditions. (a) Discharge voltage of cell 1 at current densities (40 mA/cm^2 (left) and 93 mA/cm^2 (right)) and volumetric flow rates (5 ml/min (left) and 150 ml/min (right)), and (b) Discharge voltage of cell 3 at current densities (40 mA/cm^2 (left) and 93 mA/cm^2 (right)) and volumetric flow rates (5 ml/min (left) and 150 ml/min (right)).

The flow rate affects polarization leading to voltage drop, especially at the end of the discharge (at low SOCs). This effect is dominant as the current density increased (Figure 4.2b). This can be interpreted as a result of competition between diffusion and surface reaction. At low flow rates, the diffusion rate limited the process compared to the rate of surface reactions. Due to the poor supply of active species to the electrode surface, a high concentration polarization occurs and the cell voltage is lowered. On the other hand, the mass transfer at sufficiently high flow rates is no longer limiting, and rather, the cell performance is limited by the rate of surface reactions. The mass-transfer-limit phenomenon becomes more dominant when the current density increases. Another observation is that, in general, there is a larger voltage drop when current density is higher. This is mainly caused by an ohmic drop (as seen in Fig. 4.2c and Fig. 4.2d) in which the current density changed at a fixed flow rate (c: 5 ml/min, d: 150 ml/min). One significant difference is observed between the voltage drop due to concentration polarization and ohmic loss. As the discharge process progresses (SOC decreases), the concentration polarization is accumulated, but the ohmic drop is almost instantaneous at all SOCs because it occurs immediately.

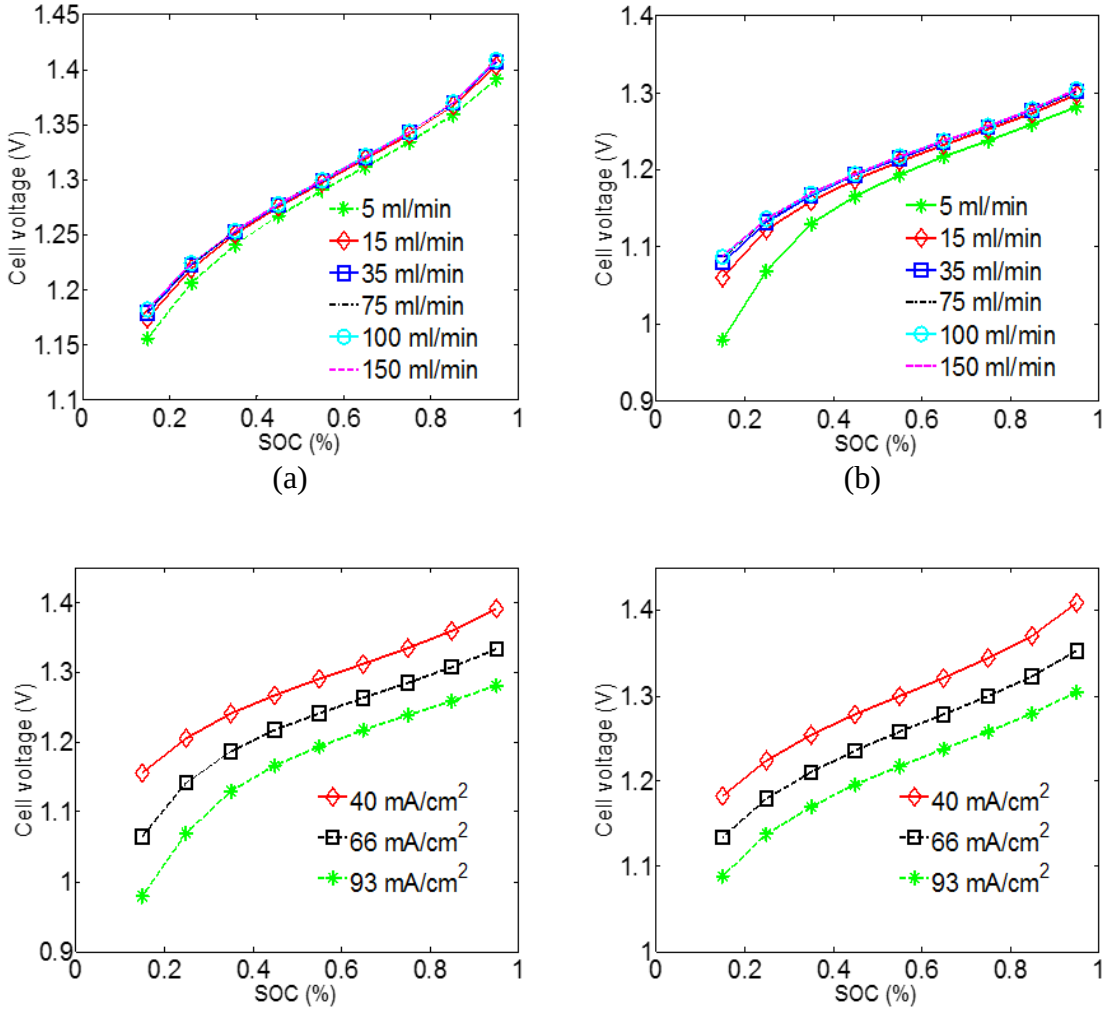

Figure 4.2. Effect of the electrolyte volumetric flow rate and current density on discharge voltage: (a) Current density 40 mA/cm^2, (b) Current density 93 mA/cm^2, (c) Volumetric flow rate 150 ml/min, (d) Volumetric flow rate 5 ml/min.

4.3. CHANNEL GEOMETRY IMPACT

4.3.1. Voltage Responses at Different Geometries. Figure 4.3 shows the voltage responses of different channel heights at different flow rates and current densities. At lower current densities, the geometric impact is stronger at lower flow rates. Also, as the current density increases, the channel impact becomes dominant, but again

weakens at higher flow rates. These differences can be attributed to the different convective diffusion behaviors of ionic reactants depending on the velocity distribution of electrolytes, as stated earlier. Figure 4.3e shows the cell voltage profile for electrolyte flow rates for the three cell designs with an SOC = 0.95 and a current density of 40 mA/cm2. It is noticed that the cell voltage is enhanced as the flow rate increases from 5 to 75 ml/min, but, at higher flow rates, the voltage improvement for all cell designs is less. The effect of flow rate on cell voltage indicates that ionic convective diffusion is the dominating factor affecting VRB performance at low electrolyte flow rates, whereas at higher flow rates, the electrochemical reaction rate is controlled by other factors such as electrode reactivity and reactive surface area, rather than convective mass transfer. In order to analyze the origin of geometry's impact, the pressure drop across the various geometries is calculated and is shown in the next section.

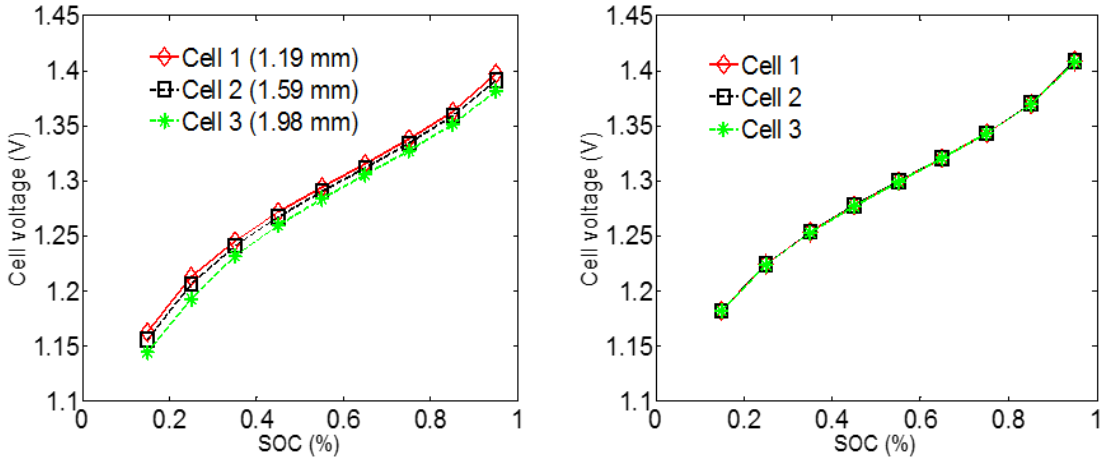

Figure 4.3. Cell voltage during discharge at different volumetric flow rates and current densities: (a) Inlet flow rate at 5 ml/min and current density of 40 mA/cm^2, (b) Inlet flow rate at 150 ml/min and current density of 40 mA/cm^2, (c) Inlet flow rate at 5 ml/min and current density of 93 mA/cm^2, (d) Inlet flow rate at 150 ml/min and current density of 93 mA/cm^2, (e) Range of flow rates and current density of 40 mA/cm^2 at a SOC =0.95.

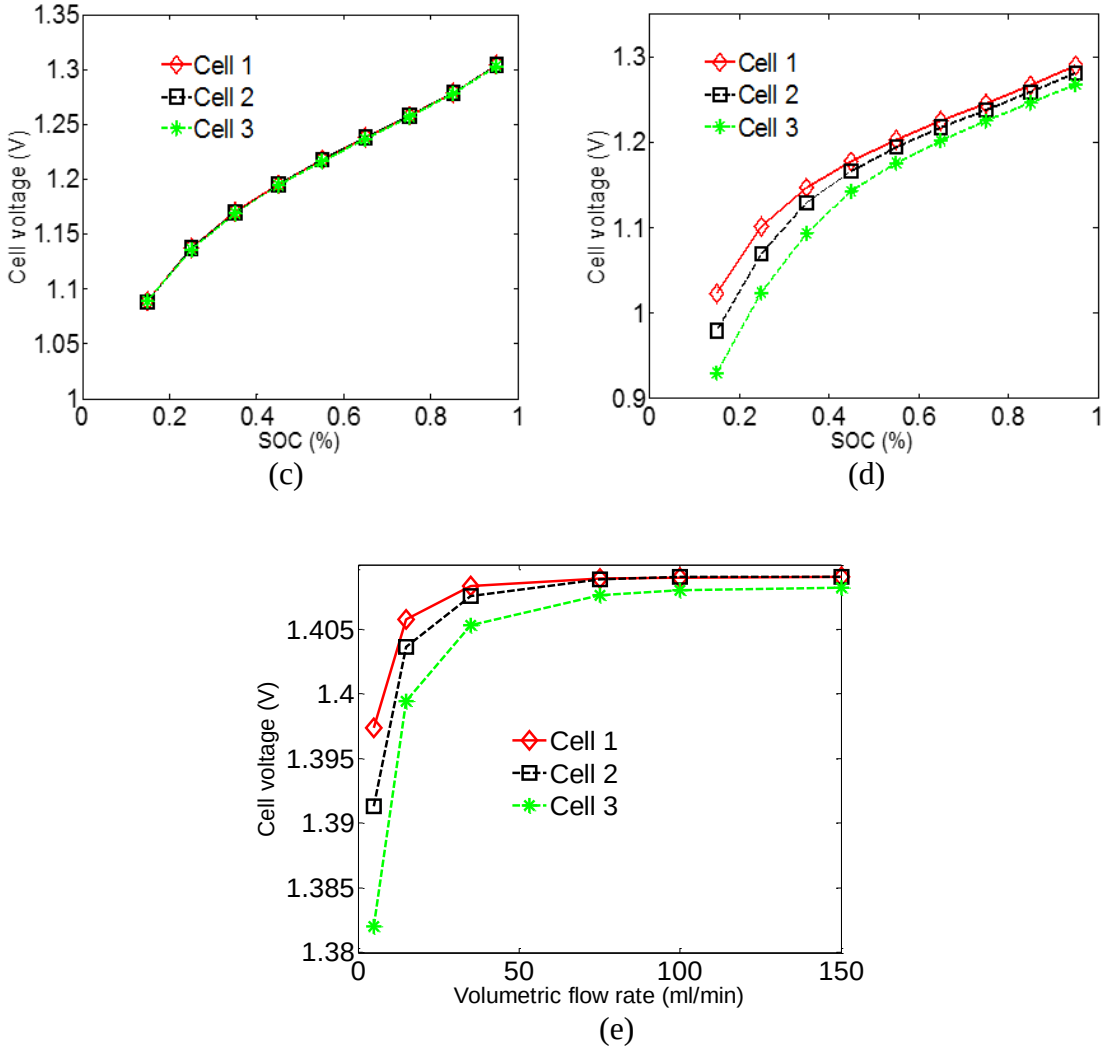

Figure 4.3. Cell voltage during discharge at different volumetric flow rates and current densities: (a) Inlet flow rate at 5 ml/min and current density of 40 mA/cm^2, (b) Inlet flow rate at 150 ml/min and current density of 40 mA/cm^2, (c) Inlet flow rate at 5 ml/min and current density of 93 mA/cm^2, (d) Inlet flow rate at 150 ml/min and current density of 93 mA/cm^2, (e) Range of flow rates and current density of 40 mA/cm^2 at a SOC =0.95 (cont.).

4.3.2. Pressure Drop at Different Geometries. The pressure drop losses in the stack as well as the associated pipes between the stack and storage tanks must be kept to a minimum to minimize pumping power. At the same time, it is necessary to maintain good supply of fresh electrolyte to the reaction sites. In a VRFB, this is achieved by

ensuring good crossflow through the electrode material. Figure 4.4a shows the pressure distribution in the cathode electrode at a 150 ml/min flow rate with different channel designs. The distribution looks generally similar, but there is a big difference in magnitude. The fluid pressure drop of cell 1 is about 52% higher than that of cell 3. This is because the velocity in cell 1 is the highest of the three cells, as the cross sectional area is the smallest. As shown in Figure 4.4b, the pressure drop increases nonlinearly as the flow rate increases. This may be related to the frictional factor, which is approximately proportional to the square of velocity for a fully developed flow in a square channel. This pressure drop is later used to evaluate the pumping power to calculate efficiencies.

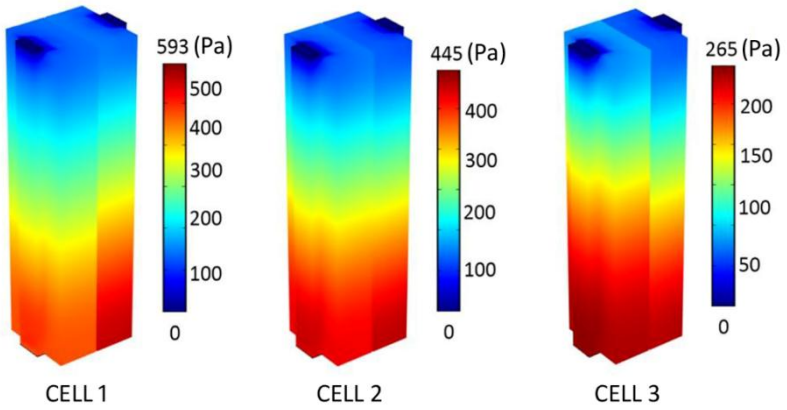

(a)

Figure 4.4. (a) Pressure distribution at 150 ml/min of the three cell configurations, (b) Pressure drop as a function of inlet flow rate.

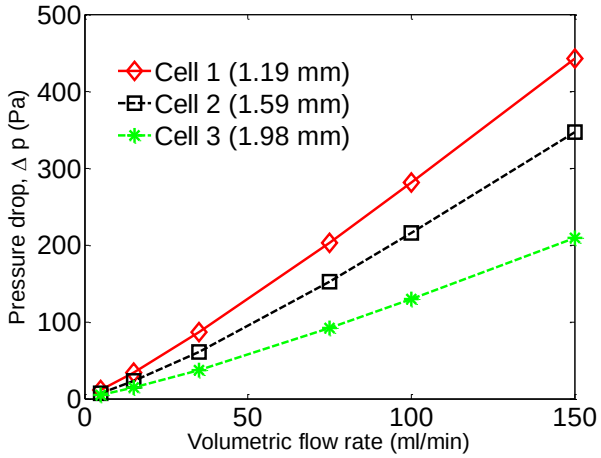

(b)

Figure 4.4. (a) Pressure distribution at 150 ml/min of the three cell configurations, (b) Pressure drop as a function of inlet flow rate (cont.).

4.3.3. Electrolyte Penetration into the Porous Electrode. As the actual electrochemical reaction occurs in porous electrodes, consequently, the transport of the electrolyte to the electrode determines the cell performance. In order to evaluate transport to the electrode, a ratio value (Rp) representing the penetrated electrolytes is introduced, by calculating the flow volume ratio at the electrode to the interface of the channel. The flow volume is estimated by multiplying the average velocity at each point by the area and the input flow rate. Figure 4.5 shows the impact of flow channel height on Rp at different flow rates on cathode side. As shown, cell 1 penetrates more than the other two cells, which can be attributed to the pressure difference across the half-cell geometry resulting from the small cross-sectional area of the cell. This explains the better performance of cell 1 shown Figure 4.3a. However, at a higher flow rate, the impact of channel height becomes weak, as shown Fig. 4.3b. This means that the amount of

electrolyte entering the porous electrode is less influential on performance as it transits into the reaction-limited region, which is consistent with the previous discussion.

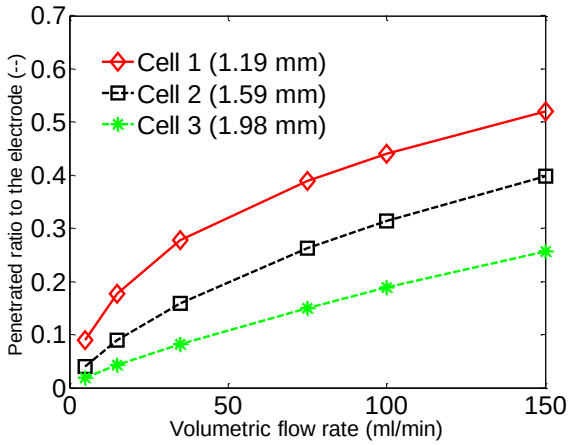

Figure 4.5. Ratio of amount of penetrated electrolyte to the porous electrodes of the three cells.

4.3.4. Energy Efficiency, Battery Efficiency, and Pumping Power. High efficiency is one of the key requirements for energy storage components in all applications. Energy efficiency and battery efficiency are analyzed under various flow rates, based on Eqs. (6) and (7). Energy efficiency of all three cells in Figure 4.6a improves gradually with increased flow rates, and it is obvious that cell 1 is more efficient than the others. The efficiencies of batteries, depicted in Figure 4.6b, reach maximum values of 90.10%, 90.06%, and 89.90% for cell 1, cell 2, and cell 3, respectively, at around 35 ml/min and 40 mA/cm2. Efficiency declines at high flow rates (behind the optimal flow value) due to increasing pump energy consumption, as shown in Figure 4.6c.

Note that the battery efficiency in Figure 4.6c is based on the average charging-discharging voltage calculation in the range of SOCs. Figure 4.6d shows the battery efficiency of cell 2 at each SOC and the highest battery efficiency is around 90.1% at SOC=0.55 for the same applied boundary conditions. This can be attributed to the fact that a minimum over-potential occurs when the SOC=0.55 due to the symmetrical anodic and cathodic coefficients. Besides, there is an equal supply of both oxidized and reduced vanadium active species at the electrodes. As shown in Figure 4.6d, the pumping power increases due to an increased pressure drop with a higher flow rate. Also, as shown in Figure 4.6a, the battery efficiency of cell 3 drops more slowly after reaching maximum efficiency than the others do. This is because the power consumption rate for cell 3 is lower than others due to a smaller pressure drop (see Figure 4.4b). The variation in battery efficiency with an increasing flow rate is mainly caused by non-linear pumping power consumption. As the flow rate becomes higher, the energy loss due to pumping becomes significant. This implies that the flow rate must be tuned to, and depend on, operating conditions.

4.3.5. Effect of the Applied Current on the System Efficiency. The impacts of three different current densities (40, 66, and 93 mA/cm2) on performance are compared. Figure 4.7a shows the battery efficiency for cell 2. It is obvious that an increase in applied current would lead to decreased battery efficiency due to an increment in the corresponding over-potential cathode side (as illustrated in Figure 4.7b). In addition, it is observed in the three battery configurations, that the optimal flow rate (V^{o}_{B}) is not the same for each cell at different applied currents (as listed in Table 4.1).

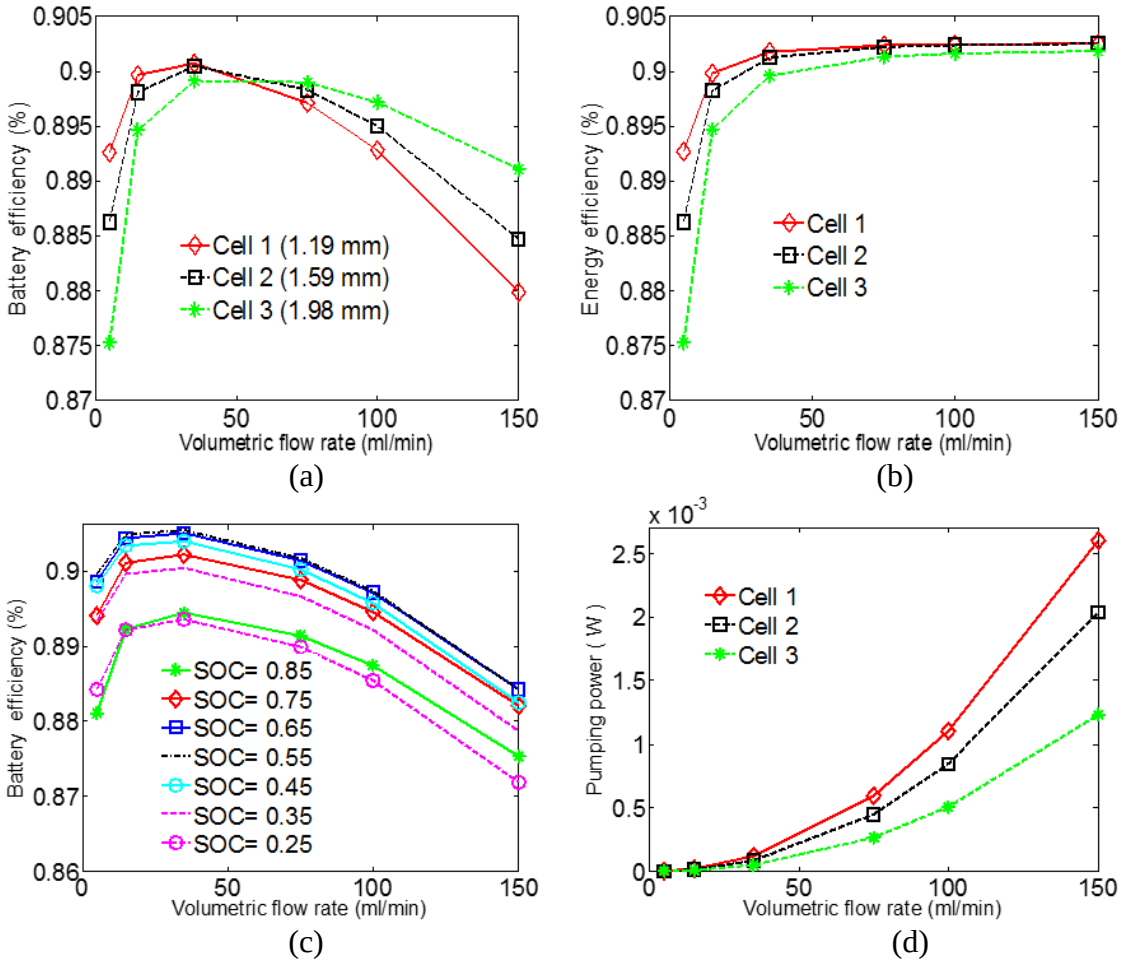

Figure 4.6. Energy, battery efficiency, and pumping power at a current density of 40 mA/cm^2. (a) Energy efficiency, (b) Battery efficiency, (c) Pumping power, (d) Battery efficiency at a range in SOCs.

Especially with cell 3, the optimum flow rate is higher than those of the other two cells. Cell 1 shows the highest efficiency and the corresponding flow rate is lower than that of the other two cells. This is desirable not only in terms of efficiency but also in reducing the risk of leakage. Therefore, from the three battery configurations, cell 1 shows the best performance; better energy, and superior battery efficiency at low flow rates.

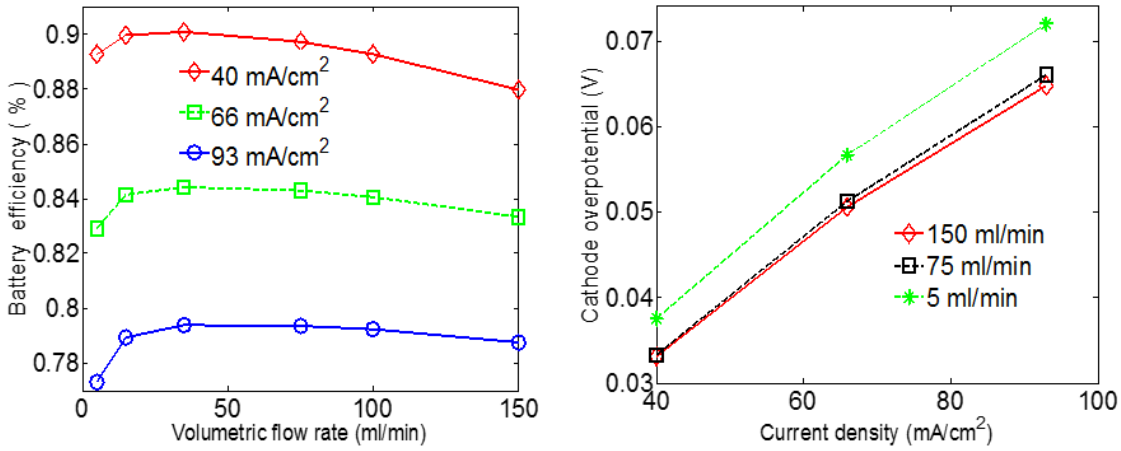

(a) (b)

Figure 4.7. Current density effect on: (a) Battery efficiency, (b) Cathode over-potential at different flow rates.

Table 4.1 Optimal flow rate and corresponding maximum battery efficiency

Cell	**Maximum battery efficiency (η_B, %) with optimal flow rate (V_B^0, ml/min)**					
	40 mA/cm^2		**66 mA/cm^2**		**93 mA/cm^2**	
	η_B	V_B^0	η_B	V_B^0	η_B	V_B^0
Cell 1	91.09	35	85.45	35	80.4	75
Cell 2	90.06	35	84.38	75	79.41	75
Cell 3	89.33	75	83.71	75	78.68	100

5. DISCUSSION

In general, a transient simulation is more costly than a steady-state simulation. In this work, all simulations are conducted with an assumption of the steady-state condition. Consequently, it is necessary to check whether this assumption is reasonable. Figure 4.8(a) compares the results from the steady-state and transient models. Both results match each other well. Since the cell voltage in the transient simulation is measured as a function of time, the time-dependent responses needs to be converted to SOC-dependent data for comparison. The conversion is done as follows [88]:

$$SOC = S_i + \frac{t}{t_t}(S_f - S_i) \tag{9}$$

where t_t is the total charging/discharging operating time, and SOC is the state of charge at the corresponding time t, and S_i, and S_f are the values of SOC at the initial and final status of charge/discharge, respectively. The SOC values can be estimated from the open circuit voltage, V_{OCV}, as follows,

$$V_{OCV} = V^{o}_{OCV} + \frac{RT}{nF} ln \frac{(SOC)^2}{(1 - SOC)^2} \tag{10}$$

where V^{o}_{OCV} is the open circuit voltage at 50% SOC which is 1.4V [89].

Next, it is essential to examine the effect of mesh size on convergence because simulation results are quite dependent on mesh size. In order to investigate mesh-dependent convergence, four different meshes of 626/1,902/2,430/3,520 elements with a total degree of freedom of 8,563/26,015/33,237/48,146, respectively, are compared for cell 2. Figure 4.8b shows a cell voltage with different mesh sizes. All results from the

meshes with more than 1,902 elements are well converged; hence, 1,902 elements are selected for all simulations.

In order to validate the model, cell 2 design (in Table 3.1.) is fabricated and tested. Figure 4.8c shows a comparison of the voltage responses from the model and an experiment with a different SOC under a galvanostatic current density of 40 mA/cm^2 and a 75 ml/min volumetric flow rate during a charge-discharge cycle. In general, they are in good agreement. The average relative error of the simulated results compared to the experimental data is less than1% (4 mV) during charging (SOC 0.15-0.95), and (7.2 mV) during the discharge cycle (SOC 0.95-0.15). Any discrepancies may have resulted from the quick depletion of reactant concentrations at a quite high SOC, during charging, and at a very low SOC, during discharge. Additional factors could be side reactions and ion cross-overs through the membrane, which are not considered in the simulation.

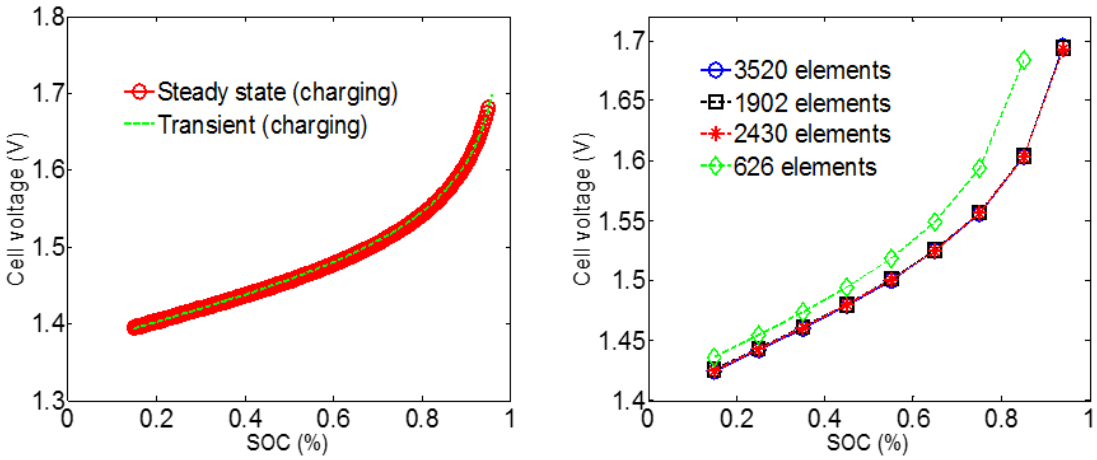

(a) (b)

Figure 4.8. (a) Cell voltage comparison for 2D transient and steady state models at a volumetric flow rate of 35 ml/min and current density of 40 mA/cm2, (b) Mesh-independence of the overall cell voltage at different SOCs, (c) Comparison of simulated and experimental values of the overall cell voltage at a current density of 40 mA/cm^2.

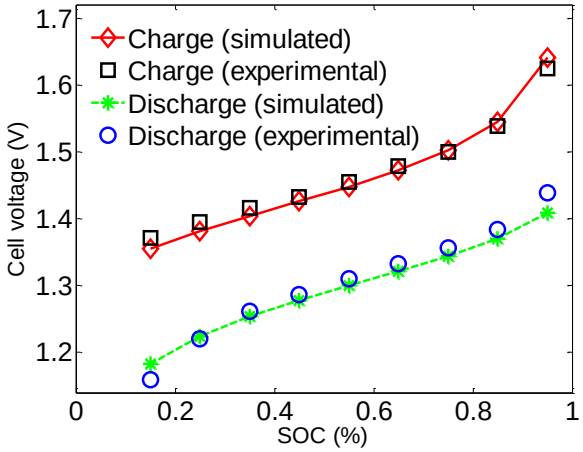

(c)

Figure 4.8. (a) Cell voltage comparison for 2D transient and steady state models at a volumetric flow rate of 35 ml/min and current density of 40 mA/cm2, (b) Mesh-independence of the overall cell voltage at different SOCs, (c) Comparison of simulated and experimental values of the overall cell voltage at a current density of 40 mA/cm^2 (cont.).

6. CONCLUSIONS

A three-dimensional electrochemical model for a vanadium redox flow battery (VRFB) is developed, validated and, then, used to study the impact of the channel height of a VRFB. The study focuses on discovering the relationship between flow rate, SOCs, and current density, along with channel height and battery performance, including voltage response and energy/battery efficiency. Fast flow rates enhance electrochemical responses during the charge/ discharge cycle, while they also degrade overall battery efficiency due to pumping energy losses. As a result, the expected battery efficiency is closely related to flow rates and current density. Generally, energy efficiency improves gradually with increased flow rate, while battery efficiency first increases and then drops due to large pump losses. The effect of channel height on battery performance becomes noticeable as the flow rate decreases and the current density increases. For the three selected representative configurations, there are different optimal flow rates for each cell design, and they change as current is applied. Also, battery efficiency varies as a function of the SOC, which is related to minimal over-potential. Overall, the energy and battery efficiency of cell 1 (smallest height among them) is better than the others. Further, its required optimal flow rate is lower than those of other cells. It is found that an optimal condition is determined by the pressure drop, amount of penetrated solutions to the electrode, and electrochemical reaction rates. This developed model can also be applied to study other factors, such as temperature and other electrode physical properties. Eventually, it can help provide guidance for optimal flow battery design and loading conditions.

APPENDIX

EQUATIONS OF THE MODEL

FLOW FIELD AND POROUS MEDIA:

The flow in the channel can be described by the momentum and continuity equation for laminar flow as follows [38]:

$$\rho\,(\vec{u}\cdot\nabla)\,\vec{u} = -\nabla p + \nabla[\mu\cdot(\nabla\vec{u} + (\nabla\vec{u})^{T})] + \overrightarrow{f} \tag{A.1}$$

$$\rho\,(\nabla\cdot\vec{u}\,) = 0 \tag{A.2}$$

where ρ is the fluid density, u is the velocity, p is the pressure, f is the volume force vector and μ is the dynamic viscosity of the fluid.

The Brinkman equation for single-phase incompressible flow is used for the transport through the porous electrode [38]:

$$\frac{\rho}{\varepsilon}\,(\vec{u}\cdot\nabla)\frac{\vec{u}}{\varepsilon} = -\nabla p + \nabla\cdot\left[\frac{\mu}{\varepsilon}\,(\nabla\vec{u} + (\nabla\vec{u})^{T})\right] - \frac{2\mu}{3\varepsilon}\nabla(\nabla\cdot\vec{u}\,) - \left(\frac{\mu}{K} + Q\right)\vec{u} + \overrightarrow{f} \tag{A.3}$$

$$\rho\,(\nabla\cdot\vec{u}\,) = 0 \tag{A.4}$$

where ε is the electrode porosity, Q is the mass source and K is the permeability of the porous electrode which is normally described by the Carman–Kozeny equation [90]:

$$K = \frac{d_f^2\ \varepsilon^3}{16C_k\,(1-\varepsilon)^2} \tag{A.5}$$

where d_f is the fiber diameter and C_k is the Carman–Kozeny constant, which depends on the type of media and is used as a fitting parameter.

SULPHURIC ACID DISSOCIATION:

To represent the dissociation of H_2SO_4 and other chemical reactions, a source term R_i is introduced in the Nernst-Planck equation, as listed in Table A.1. In general, the dissociation of H_2SO_4 occurs in two steps [82]:

$$H_2SO_4 \rightarrow H^+ + HSO_4^- \tag{A.6}$$

$$HSO_4^- \rightarrow H^+ + SO_4^- \tag{A.7}$$

In Eq. (A.6), fully complete H_2SO_4 dissociation is assumed [82]. For the second step, the following formula is used for the dissociation rate:

$$R_d = K_d \left(\frac{C_{H^+,s} - C_{HSO_4^-,s}}{C_{H^+,s} + C_{HSO_4^-,s}} - \beta \right) \tag{A.8}$$

where K_d denotes the dissociation reaction coefficient, $C_{H^+,s}$ is proton concentration, and β is the degree of dissociation of H_2SO_4.

SPECIES TRANSPORT AND CHARGE GOVERNING EQUATIONS:

Diffusion, migration, and convection are the main three mechanisms of species movement in Eq. (3) [40], which can be expressed as follows:

$$\vec{N}_{i,s} = -D_i^{eff} \nabla C_{i,s} - Z_i M_{i,s} C_{i,s} F \nabla \emptyset_{l,s} + \vec{u_l} C_{i,s} \tag{A.9}$$

where $M_{i,s}$ is the ionic (electrolyte) mobility, $\emptyset_{l,s}$ is the ionic potential, F is the Faraday constant, $\vec{u_l}$ is the velocity of the electrolyte, while D_i^{eff} is the effective diffusion coefficient found by the Bruggeman equation [84]:

$$D_i^{eff} = D_i \, \varepsilon^{1.5} \tag{A.10}$$

The ionic mobility, $M_{i,e}$, can be evaluated under the dilute solution approximation from Nernst- Einstein equation as follows [50]:

$$M_{i,e} = \frac{D_i^{eff}}{R\,T} \tag{A.11}$$

where T is the temperature and R is the universal gas constant.

Since there is no real data in regards to electrolyte viscosity of a VRFB, it is considered a constant value of μ_j for both anolyte and catholyte at 50% state of charge [40]. Table A.2 contains all the electrolyte solution properties in this model.

In the charge conservation equation, porous electrode regions combine all phenomenon of species movement, electrochemical reactions, and current transfer [84]:

$$\nabla \cdot \vec{j_l} = -\nabla \cdot \vec{j_s} = I \tag{A.12}$$

where I is the reaction current, while $\vec{j_l}$ and $\vec{j_s}$ denote the total electrolyte (ionic) and solid (electronic) current density in the porous electrode region, respectively [84]:

$$\vec{j_l} = F \sum_i Z_i \, \vec{N}_{i,e} \tag{A.13}$$

After applying the electroneutrality equation, the total ionic current density in the porous electrode can be expressed as follows:

$$\vec{j_l} = -K^{eff} \, \nabla \emptyset_{l,e} - F \sum_i Z_i \, D_i^{eff} \, \nabla C_{i,e} \tag{A.14}$$

where the effective conductivity, K^{eff}, is given by:

$$K^{eff} = \frac{F^2}{RT} \sum_i Z_i^2 \, D_i^{eff} \, \nabla C_{i,e} \tag{A.15}$$

The electronic potential, $\emptyset_{s,e}$, in the porous electrode is given by Ohm's law:

$$\vec{j_s} = \sigma_s^{eff} \nabla \emptyset_{s,e} \tag{A.16}$$

where σ_s^{eff} is the electrode effective conductivity based on the solid material conductivity σ_s, which can be determined from the Bruggeman equation as follows:

$$\sigma_s^{eff} = (1-\varepsilon)^{3/2}\,\sigma_s \tag{A.17}$$

All the porous electrode properties are shown in Table A.3.

Butler-Volmer equations are used to express the local reaction current density, $i_{a,c}$, for both anode ('a') and cathode ('c') electrodes [84].

$$i_a = a\,F\,K_{neg}\left(C_{2,e}\right)^{(1-\alpha_{neg})}\left(C_{3,e}\right)^{(\alpha_{neg})}\left[\left(\frac{C_{2,s}}{C_{2,e}}\right)exp\left(\frac{\left(1-\alpha_{neg}\right)F\,\eta_{neg}}{R_{con}\,T}\right) - \left(\frac{C_{3,s}}{C_{3,e}}\right)exp\left(\frac{\left(-\alpha_{neg}\right)F\,\eta_{neg}}{R_{con}\,T}\right)\right] \tag{A.18}$$

$$i_c = a\,F\,K_{pos}\left(C_{4,e}\right)^{(1-\alpha_{pos})}\left(C_{5,e}\right)^{(\alpha_{pos})}\left[\left(\frac{C_{4,s}}{C_{4,e}}\right)exp\left(\frac{\left(1-\alpha_{pos}\right)F\,\eta_{pos}}{R_{con}\,T}\right) - \left(\frac{C_{5,s}}{C_{5,e}}\right)exp\left(\frac{\left(-\alpha_{pos}\right)F\,\eta_{pos}}{R_{con}\,T}\right)\right] \tag{A.19}$$

In the Bulter-Volmer equation, $C_{i,e}^{s}$ denotes the species surface concentration at the porous electrode liquid-solid interface. For the anode electrode, these concentrations can be calculated by solving for $C_{2,e}^{s}$ and $C_{3,e}^{s}$ in the following equations [40]:

$$FD_2\left(\frac{C_{2,e}-C_{2,e}^{s}}{R_p}\right) = FK_{neg}\left(C_{2,e}\right)^{(1-\alpha_{neg})}\left(C_{3,e}\right)^{(\alpha_{neg})} \tag{A.20}$$

$$\left[\left(\frac{C_{2,e}^{s}}{C_{2,e}}\right)\exp\left(\frac{\left(1-\alpha_{neg}\right)F\,\eta_{neg}}{R_{con}\,T}\right)-\left(\frac{C_{3,e}^{s}}{C_{3,e}}\right)\exp\left(\frac{\left(-\alpha_{neg}\right)F\,\eta_{neg}}{R_{con}\,T}\right)\right]$$

$$FD_3\left(\frac{C_{3,e}-C_{3,e}^{s}}{R_p}\right)=FK_{neg}\left(C_{2,e}\right)^{(1-\alpha_{neg})}\left(C_{3,e}\right)^{(\alpha_{neg})}$$

$$\left[\left(\frac{C_{3,e}^{s}}{C_{3,e}}\right)\exp\left(\frac{\left(-\alpha_{neg}\right)F\,\eta_{neg}}{R_{con}\,T}\right)-\left(\frac{C_{2,e}^{s}}{C_{2,e}}\right)\exp\left(\frac{\left(1-\alpha_{neg}\right)F\,\eta_{neg}}{R_{con}\,T}\right)\right] \quad \text{(A.21)}$$

where $R_p = d_f/2$ (electrode mean pore radius) represents the average diffusive path length. A similar approach can be developed to find the concentrations in the positive half-cell by using Eq. (A.19). Also, in Eq. (A.18-A.19), K represents the reaction rate constant and (α_{neg} and α_{pos}) are anodic and cathodic charge transfer coefficients, respectively. The surface-to-volume ratio a describes the roughness of porous electrodes, whilst η represents the overpotential and it is defined as follows:

$$\eta_j = \phi_{l,e} - \phi_{s,e} - E_{0,j} \quad \text{(A.22)}$$

where $E_{0,j}$ denotes to the open circuit voltage (OCV) for anode and cathode, which can be obtained from Nernst equations as follows:

$$E_{0,neq} = E_{0,neg}^{s} + \frac{RT}{F}\,ln\left(\frac{C_{3,e}}{C_{2,e}}\right) \quad \text{(A.23)}$$

$$E_{0,pos} = E_{0,pos}^{s} + \frac{RT}{F}\,ln\left(\frac{C_{5,e}\cdot\left(C_{H,pos}\right)^{2}}{C_{4,e}}\right) \quad \text{(A.24)}$$

$E_{0,neg}^{s}$ and $E_{0,pos}^{s}$ represent the standard reduction potentials for the negative and positive electrodes, respectively. Since the proton ion is included in the main reaction of

positive electrode in Eq. (2), the proton concentration, $C_{H,pos}$, is involved in (A.24) as well.

Typically, the proton ions are not equal across the separator, therefore the Donnan potential effect was taken into account, which represents the potential difference between the membrane phase boundaries when the cell is in equilibrium conditions as follows [91]:

$$E_m^k = \frac{RT}{F} ln\left(\frac{C_{H,+}^k}{C_{H,+}^m}\right) \tag{A.25}$$

where k refers to either the anode or cathode electrode and *m* represents the separator. The required parameters for reaction kinetics in addition to the other properties of the electrodes are listed in Tables A.3 and A.4.

BOUNDARY CONDITIONS:

The developed VRFB model consists of a set of governing equations, along with their corresponding boundary conditions, as described below. For the conservation of momentum, velocity and pressure conditions apply to the inlet of inflow channel and outlet of outflow channel, respectively,

$$\begin{cases} V = \mathrm{V_B^0}/A \ \ (inlet) \\ P = P_{out} \ \ (outlet) \end{cases} \tag{A.26}$$

where $\mathrm{V_B^0}$ is the electrolyte volumetric flow rate, A is the cross-sectional area of the inlet channel. The outlet gauge pressure is usually set to zero. The no-slip boundary condition applies to the walls of the inflow/outflow channel, but there is a slip boundary condition

for the walls of electrode. The electrolyte pressure satisfied a Neumann condition at the boundaries of the electrode domain:

$$\nabla p \cdot \vec{n} = 0 \tag{A.27}$$

The concentration of reactant and product are related to SOC at any time, as expressed in [88]. Therefore, the concentration of vanadium species at the inlet of the inflow channel can be treated as constant at any given SOC. The concentration expressions of the vanadium species at the inlet at any given SOC will be:

$$\begin{cases} {C_{i,e}}^{in} = C^0 \cdot SOC\,, \;\; i = 2{,}5 \\ {C_{i,e}}^{in} = C^0 \cdot (1 - SOC), i = 3{,}4 \\ {C_{H+}}^{in} = CH^+_{pos}, in + C^0 \cdot SOC \\ {C_{H-}}^{in} = CH^+_{neg}, in + C^0 \cdot SOC \end{cases} \tag{A.28}$$

where C^0 is the initial vanadium concentration of the negative half-cell, which is equal to 1040 mol·m^{-3} in this paper. At the outlet of the outflow channel, all of the reactant diffusive fluxes are set to zero, based on the so-called fully developed flow approximation:

$$-D_i^{eff}\, \nabla C_{i,e} \cdot \vec{n} = 0 \tag{A.29}$$

All of the other boundaries of the electrode and inflow/outflow channel areset to walls, which meant no flux across the boundaries:

$$\left(-D_i^{eff}\, \nabla C_{i,e} + \overrightarrow{u_j}\, C_{i,e}\right) \cdot \vec{n} = 0 \tag{A.30}$$

In a galvanostatic operation, the flux condition for potential distribution of a porous electrode, along the electrode/collector interface, is written as follows:

$$-\sigma_s^{eff}\,\nabla\emptyset_s\cdot\vec{n}=-I \tag{A.31}$$

where I denotes the applied current density, $\vec{n}$ denotes outward unit normal vector.

During charge, the current was assumed to enter the carbon felt uniformly. For discharge, the signs are reversed. There are zero charge flux conditions for all other surfaces of the electrode. Since the conservation of charge, the charge leaving the solid phase is balanced by one entering the electrolyte. So the flux condition for potential distribution of the electrolyte along the electrode/membrane interface is as follows:

$$-K^{eff}\,\nabla\emptyset_{l,e}\cdot\vec{n}=I \tag{A.32}$$

For discharge, the situations are reversed. Also, there are insulated conditions for the rest of the electrode surfaces.

$$\begin{cases}-\vec{n}\cdot\vec{J_l}=0\\-\vec{n}\cdot\vec{J_s}=0\end{cases} \tag{A.33}$$

The solid potential at the negative electrode boundary is set to zero for electric ground condition, and is used as a reference potential for the remainder of the cell:

$$\emptyset_s=0 \tag{A.34}$$

At the positive electrode interface and along the top and bottom of the membrane, zero species flux conditions are assumed:

$$\begin{cases} -\vec{n} \cdot \vec{N}_{i,e} & (for\ electrodes) \\ -\vec{n} \cdot \vec{N}_{i,m} & (for\ membrane) \end{cases} = 0 \tag{A.35}$$

Consequently, the rest of the cell (top and bottom of the electrode and membrane domains) is taken to be electrically insulated:

$$-\vec{n}\nabla \cdot \overrightarrow{J_{l,e}} = -\vec{n}\nabla \cdot \overrightarrow{J_{s,e}} = -\vec{n}\nabla \cdot \overrightarrow{J_{l,m}} = 0 \tag{A.36}$$

The initial species concentrations and operating conditions for the simulations are given in Table A.5. The initial concentrations in the electrolytes represent a VRFB at 15% state of charge (SOC), where SOC is defined as follows:

$$For\ Anode \quad : SOC = \frac{C_{2,e}}{C_{2,e} + C_{3,e}} \tag{A.37}$$

$$For\ Cathode \quad : SOC = \frac{C_{5,e}}{C_{4,e} + C_{5,e}} \tag{A.38}$$

$$For\ total\ cell \quad : SOC = \frac{C_{2,e} + C_{5,e}}{C_{2,e} + C_{3,e} + C_{4,e} + C_{5,e}} \tag{A.39}$$

Table A.1. Source and sink terms [40].

Term	Description	Cathode	Anode
R_2	Source reaction of V^{2+} ion	-	I/F
R_3	Source reaction of V^{3+} ion	-	- I/F
R_4	Source reaction of V^{4+} ion	I/F	-
R_5	Source reaction of V^{5+} ion	- I/F	-
R_{H^+}	Source reaction of proton H^+	$-R_d$	$-2 * \mathrm{I/F} - R_d$
$R_{HSO_4^-}$	Source reaction of HSO_4^- ion	R_d	R_d

Table A.2. Properties of electrolyte solution.

Symbol	Description	Value and unit	Origin
β	HSO_4^- dissociation degree	0.25	[92]
K_d	HSO_4^- dissociation rate	10^4 (S^{-1})	Fitted parameter
μ_{neg}	Anolyte viscosity	0.0025 $(Pa \cdot s)$	[5]
μ_{pos}	Catholyte viscosity	0.0050 $(Pa \cdot s)$	[5]
ρ_{neg}	Anolyte density	1300 $(kg \cdot m^{-3})$	[5]
ρ_{pos}	Catholyte density	1350 $(kg \cdot m^{-3})$	[93]
D_2	V^{2+} diffusion coefficient	2.4×10^{-10} $(m^2 \cdot s^{-1})$	[94]
D_3	V^{3+} diffusion coefficient	2.4×10^{-10} $(m^2 \cdot s^{-1})$	[94]
D_4	V^{4+} diffusion coefficient	3.9×10^{-10} $(m^2 \cdot s^{-1})$	[94]
D_5	V^{5+} diffusion coefficient	3.9×10^{-10} $(m^2 \cdot s^{-1})$	[94]
D_{H^+}	Proton diffusion coefficient	9.312×10^{-9} $(m^2 \cdot s^{-1})$	[95]
$D_{HSO_4^-}$	HSO_4^- diffusion coefficient	1.33×10^{-9} $(m^2 \cdot s^{-1})$	[95]
$D_{SO_4^{2-}}$	SO_4^{2-} diffusion coefficient	1.065×10^{-9} $(m^2 \cdot s^{-1})$	[95]

Table A.3. Porous electrode properties [40].

Symbol	Description	Value and unit	Origin
ε	Electrode porosity	0.929	[32]
d_f	Fiber diameter	50.3 (μm)	Provided by manufacturer
$\boldsymbol{a}$	Specific surface area	3.5×10^4 (m^{-1})	[32]
C_k	Kozeny-carmen coefficient	180	[96]
H_{cell}	Electrode height	50 (mm)	Measured
W_{cell}	Electrode width	50 (mm)	Measured
l_e	Electrode thickness	6 (mm)	Measured
σ_s^{eff}	Electronic conductivity of electrode	66.7 $(S \cdot m^{-1})$	Provided by manufacturer

Table A.4. Kinetic parameters [40].

Symbol	Description	Value and unit	Origin
K_{neg}	Anode reaction rate constant	7×10^{-8} $(m \cdot s^{-1})$	[97]
K_{pos}	Cathode reaction rate constant	2.5×10^{-8} $(m \cdot s^{-1})$	[94]
α_{neg}	Negative charge transfer coefficient	0.45	Estimated
α_{pos}	Positive charge transfer coefficient	0.55	Estimated
$E^{s}_{0,neg}$	Standard potential for anode	-0.255 (V)	[84]
$E^{s}_{0,pos}$	Standard potential for cathode	1.004 (V)	[84]

Table A.5. Initial species concentrations and operating conditions [40].

Symbol	Description	Value and unit
CV^{2+}, in	V^{2+} initial concentration in anolyte	156 $(mol \cdot m^{-3})$
CV^{3+}, in	V^{3+} initial concentration in anolyte	884 $(mol \cdot m^{-3})$
CV^{4+}, in	V^{4+} initial concentration in catholyte	884 $(mol \cdot m^{-3})$
CV^{5+}, in	V^{5+} initial concentration in catholyte	156 $(mol \cdot m^{-3})$
CH^{+}_{neg}, in	H^{+}_{neg} initial concentration in anolyte	4447.5 $(mol \cdot m^{-3})$
CH^{+}_{pos}, in	H^{+}_{pos} initial concentration in catholyte	5097.5 $(mol \cdot m^{-3})$
$CHSO_4^{-+}, in$	HSO_4^{-} initial concentration in catholyte	3058.5 $(mol \cdot m^{-3})$
$CHSO_4^{--}, in$	HSO_4^{-} initial concentrationanolyte	2668.5 $(mol \cdot m^{-3})$
T	Operating temperature	300 (K)
I	Current range	0.15-0.35 (A)
V_B^0	Volumetric flow rate range	5-150 $(mL \cdot min^{-1})$
P_{out}	Outlet pressure condition	$0(kpa)$

REFERENCES

[1] C. Blanc and A. Rufer, *Understanding the vanadium redox flow batteries*: INTECH Open Access Publisher, 2010.

[2] B. Dunn, H. Kamath, and J.-M. Tarascon, "Electrical energy storage for the grid: a battery of choices," *Science,* vol. 334, pp. 928-935, 2011.

[3] A. Demirbas, "Potential applications of renewable energy sources, biomass combustion problems in boiler power systems and combustion related environmental issues," *Progress in energy and combustion science,* vol. 31, pp. 171-192, 2005.

[4] A. Mostafaeipour and N. Mostafaeipour, "Renewable energy issues and electricity production in Middle East compared with Iran," *Renewable and Sustainable Energy Reviews,* vol. 13, pp. 1641-1645, 2009.

[5] E. Sum, M. Rychcik, and M. Skyllas-Kazacos, "Investigation of the V (V)/V (IV) system for use in the positive half-cell of a redox battery," *Journal of Power sources,* vol. 16, pp. 85-95, 1985.

[6] M. Skyllas-Kazacos, M. Rychcik, R. G. Robins, A. Fane, and M. Green, "New all-vanadium redox flow cell," *J. Electrochem. Soc.;(United States),* vol. 133, 1986.

[7] M. Schreiber, M. Harrer, A. Whitehead, H. Bucsich, M. Dragschitz, E. Seifert, *et al.*, "Practical and commercial issues in the design and manufacture of vanadium flow batteries," *Journal of Power Sources,* vol. 206, pp. 483-489, 2012.

[8] H. L. Ferreira, R. Garde, G. Fulli, W. Kling, and J. P. Lopes, "Characterisation of electrical energy storage technologies," *Energy*, vol. 53, pp. 288-298, 2013.

[9] A. M. Howlader, Y. Izumi, A. Uehara, N. Urasaki, T. Senjyu, A. Yona, *et al.*, "A minimal order observer based frequency control strategy for an integrated wind-battery-diesel power system," *Energy,* vol. 46, pp. 168-178, 2012.

[10] C. W. Tan, T. C. Green, and C. A. Hernandez-Aramburo, "A stochastic method for battery sizing with uninterruptible-power and demand shift capabilities in PV (photovoltaic) systems," *Energy,* vol. 35, pp. 5082-5092, 2010.

[11] P. Arun, R. Banerjee, and S. Bandyopadhyay, "Optimum sizing of battery-integrated diesel generator for remote electrification through design-space approach," *Energy,* vol. 33, pp. 1155-1168, 2008.

[12] V. Virulkar, M. Aware, and M. Kolhe, "Integrated battery controller for distributed energy system," *Energy,* vol. 36, pp. 2392-2398, 2011.

[13] G. Kear, A. A. Shah, and F. C. Walsh, "Development of the all-vanadium redox flow battery for energy storage: a review of technological, financial and policy aspects," *International journal of energy research,* vol. 36, pp. 1105-1120, 2012.

[14] P. Leung, X. Li, C. P. De León, L. Berlouis, C. J. Low, and F. C. Walsh, "Progress in redox flow batteries, remaining challenges and their applications in energy storage," *Rsc Advances,* vol. 2, pp. 10125-10156, 2012.

[15] A. Shibata and K. Sato, "Development of vanadium redox flow battery for electricity storage," *Power Engineering Journal,* vol. 13, pp. 130-135, 1999.

[16] B. K. Bose, "Global energy scenario and impact of power electronics in 21st century," *IEEE Transactions on Industrial Electronics,* vol. 60, pp. 2638-2651, 2013.

[17] M. Y. Suberu, M. W. Mustafa, and N. Bashir, "Energy storage systems for renewable energy power sector integration and mitigation of intermittency," *Renewable and Sustainable Energy Reviews,* vol. 35, pp. 499-514, 2014.

[18] H. Zhang, H. Zhang, X. Li, Z. Mai, and J. Zhang, "Nanofiltration (NF) membranes: the next generation separators for all vanadium redox flow batteries (VRBs)?," *Energy & Environmental Science,* vol. 4, pp. 1676-1679, 2011.

[19] H. Zhang, H. Zhang, X. Li, Z. Mai, and W. Wei, "Silica modified nanofiltration membranes with improved selectivity for redox flow battery application," *Energy Environ. Sci.,* vol. 5, pp. 6299-6303, 2012.

[20] S. Zhong, M. Kazacos, R. Burford, and M. Skyllas-Kazacos, "Fabrication and activation studies of conducting plastic composite electrodes for redox cells," *Journal of power sources,* vol. 36, pp. 29-43, 1991.

[21] V. Haddadi-Asl, M. Kazacos, and M. Skyllas-Kazacos, "Carbon–polymer composite electrodes for redox cells," *Journal of applied polymer science,* vol. 57, pp. 1455-1463, 1995.

[22] S. Zhong, M. Kazacos, M. S. Kazacos, and V. Haddadi-Asl, "Flexible, conducting plastic electrode and process for its preparation," ed: Google Patents, 1997.

[23] W. Wang, Q. Luo, B. Li, X. Wei, L. Li, and Z. Yang, "Recent progress in redox flow battery research and development," *Advanced Functional Materials,* vol. 23, pp. 970-986, 2013.

[24] D. Aaron, Q. Liu, Z. Tang, G. Grim, A. Papandrew, A. Turhan, *et al.*, "Dramatic performance gains in vanadium redox flow batteries through modified cell architecture," *Journal of Power sources,* vol. 206, pp. 450-453, 2012.

[25] M. Skyllas-Kazacos and M. Kazacos, "State of charge monitoring methods for vanadium redox flow battery control," *Journal of Power Sources,* vol. 196, pp. 8822-8827, 2011.

[26] X. Li and I. Sabir, "Review of bipolar plates in PEM fuel cells: Flow-field designs," *International Journal of Hydrogen Energy,* vol. 30, pp. 359-371, 2005.

[27] P. Hamilton and B. Pollet, "Polymer electrolyte membrane fuel cell (PEMFC) flow field plate: design, materials and characterisation," *Fuel cells,* vol. 10, pp. 489-509, 2010.

[28] H. Yang and T. Zhao, "Effect of anode flow field design on the performance of liquid feed direct methanol fuel cells," *Electrochimica Acta,* vol. 50, pp. 3243-3252, 2005.

[29] C. W. Wong, T. Zhao, Q. Ye, and J. Liu, "Experimental investigations of the anode flow field of a micro direct methanol fuel cell," *Journal of Power Sources,* vol. 155, pp. 291-296, 2006.

[30] X. Ma, H. Zhang, C. Sun, Y. Zou, and T. Zhang, "An optimal strategy of electrolyte flow rate for vanadium redox flow battery," *Journal of Power Sources,* vol. 203, pp. 153-158, 4/1/ 2012.

[31] A. Kazim, H. Liu, and P. Forges, "Modelling of performance of PEM fuel cells with conventional and interdigitated flow fields," *Journal of Applied Electrochemistry,* vol. 29, pp. 1409-1416, 1999.

[32] H. Dohle, R. Jung, N. Kimiaie, J. Mergel, and M. Müller, "Interaction between the diffusion layer and the flow field of polymer electrolyte fuel cells—experiments and simulation studies," *Journal of Power Sources,* vol. 124, pp. 371-384, 2003.

[33] W.-M. Yan, C.-H. Yang, C.-Y. Soong, F. Chen, and S.-C. Mei, "Experimental studies on optimal operating conditions for different flow field designs of PEM fuel cells," *Journal of power sources,* vol. 160, pp. 284-292, 2006.

[34] C. Xu and T. Zhao, "A new flow field design for polymer electrolyte-based fuel cells," *Electrochemistry communications,* vol. 9, pp. 497-503, 2007.

[35] P. Suresh, S. Jayanti, A. Deshpande, and P. Haridoss, "An improved serpentine flow field with enhanced cross-flow for fuel cell applications," *International journal of hydrogen energy,* vol. 36, pp. 6067-6072, 2011.

[36] R. J. Kee and H. Zhu, "Distribution of incompressible flow within interdigitated channels and porous electrodes," *Journal of Power Sources,* vol. 299, pp. 509-518, 2015.

[37] S. Kumar and S. Jayanti, "Effect of flow field on the performance of an all-vanadium redox flow battery," *Journal of Power Sources,* vol. 307, pp. 782-787, 2016.

[38] C. Dennison, E. Agar, B. Akuzum, and E. Kumbur, "Enhancing mass transport in redox flow batteries by tailoring flow field and electrode design," *Journal of The Electrochemical Society,* vol. 163, pp. A5163-A5169, 2016.

[39] J. Q. Chen, B. G. Wang, and H. L. Lv, "Numerical simulation and experiment on the electrolyte flow distribution for all vanadium redox flow battery," in *Advanced Materials Research*, 2011, pp. 604-607.

[40] S. Tsushima, S. Sasaki, and S. Hirai, "Influence of cell geometry and operating parameters on performance of a redox flow battery with serpentine and interdigitated flow fields," in *Meeting Abstracts*, 2013, pp. 1664-1664.

[41] D. Aaron, Z. Tang, A. B. Papandrew, and T. A. Zawodzinski, "Polarization curve analysis of all-vanadium redox flow batteries," *Journal of Applied Electrochemistry,* vol. 41, pp. 1175-1182, 2011.

[42] B. J. Koeppel, K. P. Recknagle, D. E. Stephenson, D. Reed, E. Thomsen, and V. Sprenkle, "Redesign of a vanadium redox flow battery for reduced pressure loss using an interdigitated flow field," in *Meeting Abstracts*, 2013, pp. 1660-1660.

[43] G. Qiu, A. S. Joshi, C. Dennison, K. Knehr, E. Kumbur, and Y. Sun, "3D pore-scale resolved model for coupled species/charge/fluid transport in a vanadium redox flow battery," *Electrochimica Acta,* vol. 64, pp. 46-64, 2012.

[44] J. Escudero-Gonzalez and P. A. López-Jiménez, "Methodology to optimize fluid-dynamic design in a redox cell," *Journal of Power Sources,* vol. 251, pp. 243-253, 2014.

[45] C. Yin, Y. Gao, S. Guo, and H. Tang, "A coupled three dimensional model of vanadium redox flow battery for flow field designs," *Energy,* vol. 74, pp. 886-895, 2014.

[46] Y. Wang and S. C. Cho, "Analysis and three-dimensional modeling of vanadium flow batteries," *Journal of The Electrochemical Society,* vol. 161, pp. A1200-A1212, 2014.

[47] M. Vynnycky, "Analysis of a model for the operation of a vanadium redox battery," *Energy,* vol. 36, pp. 2242-2256, 2011.

[48] A. Shah, M. Watt-Smith, and F. Walsh, "A dynamic performance model for redox-flow batteries involving soluble species," *Electrochimica Acta,* vol. 53, pp. 8087-8100, 2008.

[49] K. Knehr, E. Agar, C. Dennison, A. Kalidindi, and E. Kumbur, "A transient vanadium flow battery model incorporating vanadium crossover and water transport through the membrane," *Journal of The Electrochemical Society,* vol. 159, pp. A1446-A1459, 2012.

[50] D. M. Bernardi and M. W. Verbrugge, "Mathematical model of a gas diffusion electrode bonded to a polymer electrolyte," *AIChE journal,* vol. 37, pp. 1151-1163, 1991.

[51] G. Pourcelly, A. Lindheimer, C. Gavach, and H. D. Hurwitz, "Electrical transport of sulphuric acid in nation perfluorosulphonic membranes," *Journal of electroanalytical chemistry and interfacial electrochemistry,* vol. 305, pp. 97-113, 1991.

[52] C. Blanc, "Modeling of a vanadium redox flow battery electricity storage system," 2009.

[53] C. Blanc and A. Rufer, "Optimization of the operating point of a vanadium redox flow battery," in *Energy Conversion Congress and Exposition, 2009. ECCE 2009. IEEE,* 2009, pp. 2600-2605.

[54] D. You, H. Zhang, and J. Chen, "A simple model for the vanadium redox battery," *Electrochimica Acta,* vol. 54, pp. 6827-6836, 2009.

[55] T. Sukkar and M. Skyllas-Kazacos, "Water transfer behaviour across cation exchange membranes in the vanadium redox battery," *Journal of Membrane Science,* vol. 222, pp. 235-247, 2003.

[56] X. Ma, H. Zhang, and F. Xing, "A three-dimensional model for negative half cell of the vanadium redox flow battery," *Electrochimica Acta,* vol. 58, pp. 238-246, 2011.

[57] K. Knehr and E. Kumbur, "Open circuit voltage of vanadium redox flow batteries: Discrepancy between models and experiments," *Electrochemistry Communications,* vol. 13, pp. 342-345, 2011.

[58] D. Knopf, B. Luo, U. Krieger, and T. Koop, "Thermodynamic dissociation constant of the bisulfate ion from Raman and ion interaction modeling studies of aqueous sulfuric acid at low temperatures," *The Journal of Physical Chemistry A,* vol. 107, pp. 4322-4332, 2003.

[59] G. Oriji, Y. Katayama, and T. Miura, "Investigation on V (IV)/V (V) species in a vanadium redox flow battery," *Electrochimica Acta,* vol. 49, pp. 3091-3095, 2004.

[60] T. YAMAMURA, N. WATANABE, T. YANO, and Y. SHIOKAWA, "Electron-transfer kinetics of Np3/Np4, NpO (/NpO2 2, V2/V3, and VO2/VO 2 at carbon electrodes," *J. Electrochem. Soc,* vol. 152, pp. A830-A836.

[61] J. Newman and K. E. Thomas-Alyea, *Electrochemical systems*: John Wiley & Sons, 2012.

[62] H. Zhou, H. Zhang, P. Zhao, and B. Yi, "A comparative study of carbon felt and activated carbon based electrodes for sodium polysulfide/bromine redox flow battery," *Electrochimica Acta*, vol. 51, pp. 6304-6312, 2006.

[63] P. Xu and B. Yu, "Developing a new form of permeability and Kozeny–Carman constant for homogeneous porous media by means of fractal geometry," *Advances in water resources*, vol. 31, pp. 74-81, 2008.

[64] E. Sum and M. Skyllas-Kazacos, "A study of the V (II)/V (III) redox couple for redox flow cell applications," *Journal of Power sources*, vol. 15, pp. 179-190, 1985.

II. NEW SINGLE CELL DESIGN OF A VANADIUM REDOX FLOW BATTERY

ABSTRACT

Vanadium redox flow battery (VRFB) is a type of electrochemical energy storage device commonly used in stationary applications. In this study, a new single-cell design of VRFB with a serpentine flow channel was designed and built. The introduced design is made with fewer components than the existing VRFB cells, making it very economical and greatly enhancing safety and ease of assembly. In addition, mechanical strength and impermeability are greatly improved by replacing graphite for the flow path, which is fragile and porous, with PVC (polyvinyl chloride) sheet. This makes it possible to expect a longer life, particularly in harsh environments exposed to shocks and vibrations.

Many tests have been conducted to compare this new design with traditional design. These tests include cycling, polarization across the current range with flow range, and electrochemical impedance spectroscopy (EIS) for internal resistance analysis. The results show that the new design has a very stable cycling performance with better columbic and energy efficiency compared to the existing designs.

To evaluate the applicability of this design, cycle tests of different current conditions were performed. The polarization test reaffirmed that a higher output was obtained from the new design than the existing cell for the same external cell dimensions. However, a sharp drop in voltage was observed through the polarization test, which is considered to be due to the high contact resistance between the current collector and the porous electrode. This is solved by introducing a thin graphite film as the current

collector. Finally, according to economic analysis, the new assembly is not only easy to assemble, but also lightweight and cost-effective.

1. INTRODUCTION

Vanadium redox flow batteries (VRFBs) are being widely considered for grid-scale energy storage applications due to them having many attractive features such as system flexibility, uncoupled energy and power capacities, relative safety, and long lives due to the decreased risk of cross-contamination of the electrode compartments [41, 44, 98]. Traditional VRFB cells with flow field design consist of a cathode and anode, a membrane separator, current collectors, gaskets, insulators, and graphite plates engraved with flow channels. All of these components are carefully compressed between two endplates. The schematic diagram of VRFB is shown in Figure 1.1. The electrolyte solutions are stored in external reservoirs; the positive couple (V^{+5}/V^{+4}) (present as VO_{2+}/VO^{2+} in cathode side) and the negative couple (V^{+3}/V^{+2} in anode side) are the vanadium solutions that flow into the battery cell, where redox reactions occur near the surfaces of the electrodes. Electrons leave the anode side to the cathode during the discharge process, whereas a reverse process during the charge occurs. This redox stores or releases electrical energy, allowing the battery to be charged or discharged as described below [62]:

At the positive electrode,

$$V^{4+} + H_2O \underset{discharge-charge}{\longleftrightarrow} V^{5+} + 2H^+ + e^- \left(E^s_{0,pos} = 1.004\ \text{V}\ vs.\ \text{SHE}\right) \quad (1)$$

At the negative electrode,

$$V^{3+} + e^- \underset{discharge-charge}{\longleftrightarrow} V^{2+} \quad \left(E^s_{0,neg} = -0.255\ \text{V}\ vs.\ \text{SHE}\right) \quad (2)$$

Overall reaction:

$$V^{5+} + V^{2+} + 2H^{+} \underset{discharge-charge}{\longleftrightarrow} V^{4+} + V^{3+} + H_2O \quad (3)$$

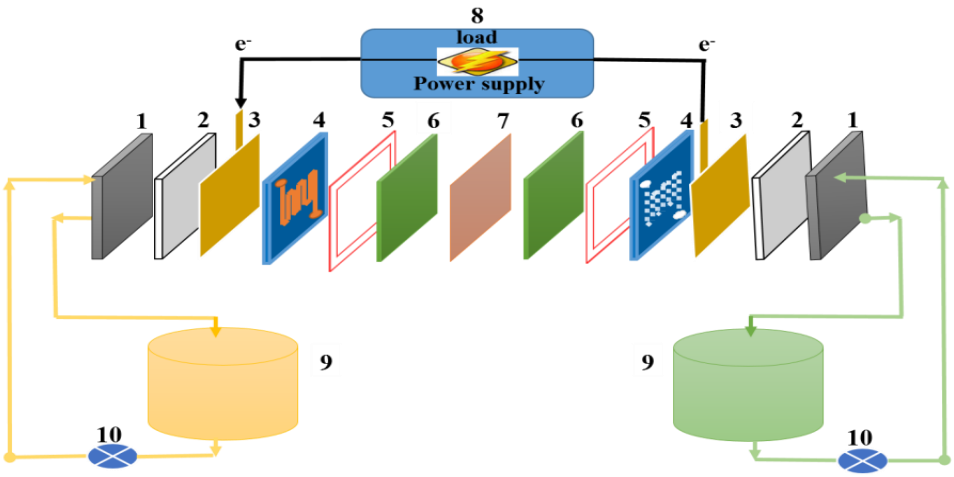

Figure 1.1. A schematic diagram of a traditional VRFB. (1) End plates, (2) Insulators (3) Current collectors, (4) Graphite flow field, (5) Gaskets, (6) Cathode and anode electrodes, (7) Membrane, (8) load/power supply, (9) Electrolyte tanks, (10) Pumps.

All reactants and products of the redox reaction that occurs in the electrodes remain dissolved in the two electrolyte solutions used in VRFBs. If crossover contamination occurs, the two electrolyte solutions will mix together which retrieves the initial system electrolyte, and eventually leads to energy loss [6]. The number and surface area of the electrodes determine the output power of the VRFB, whereas the amount and concentration of the liquid electrolyte at each tank can determine the system capacity and energy. This means that the storage capacity and output power of the VRFB are independent [44].

It is important that redox flow battery systems are optimized in terms of performance and/or cost in order to perform well in the commercial marketplace. It has been reported that the majority of the cost of VRFB systems is the materials required for construction [7]. If new materials are not developed in order to reduce cost, the battery system performance must be improved to make the systems more cost effective. This enables a reduction in the multi-cell battery size and cost coupled with achieving certain output power needs.

In general, vanadium redox flow battery and fuel cell technology share almost the same internal components. Bipolar plate, also called the flow-field plate, is considered as one of the main components. The bipolar plate performs the following functions: distribute the electrolyte solution inside the battery cells, isolate different cells in the multi-cell battery core, convey current into and out of the cell, and dissipate the stack heat [9]. Its main role is to deliver reactants to and from the porous anode and cathode materials via flow field channels. It has been noticed that the way of flow-field design has a partial impact on the success of electrolyte transport [99]. Finding appropriate materials of bipolar plates becomes an important requirement in both VRFB and fuel cell stack development technologies. The bipolar plate materials should have unique features such as high availability, low cost, low permeability to the chemical solution, good chemical compatibility to acids, high corrosion resistance, and reasonable strength [10].

In the literature of fuel cells, three different kinds of bipolar materials have been examined and can be categorized as metals, nonmetals (graphite), and graphite composite materials (polymers) [100]. For mobile applications, metal bipolar plates are considered suitable and safe candidates because they show the major constraints of the required

features of bipolar plates such as very good electrical conductivity, low cost, excellent mechanical strength, easy manufacture, and simple maintenance, though it requires a corrosion-protective coating for lifetime improvement [101-105]. Nonmetal plate (pure graphite) offers excellent chemical resistance for strong acids and high thermal conductivity for heat management, and it works as a good electric conductive material with a high corrosion and lower density as compared to metal ones; nevertheless, engraving the flow field channel is difficult process and requires more time, which results in very high costs [106]. Additionally, graphite plates are porous and brittle by nature, which requires them to be coated to prevent reactant penetration, making them poor candidates for low-cost components [19]. Last of all, polymer composites are specified to improve and achieve the desired properties of bipolar plates. Composites have less bulk density than the other two types and can be shaped into any structure and dimension, which makes them an excellent option for flow battery and fuel cell stacks. Normally, composite plates consist of commercial polymers and work as binders and high loading conductive carbon compounds to enhance the plate conductivity [107]. For VRFB systems, the environment is not the same as in the fuel cell due to using an acidic concentrated vanadium with the bipolar plates, which needs different requirements for bipolar plates to be operated at different applied operating conditions [108].

Despite efforts to create new composite materials to improve the bulk conductivity and the properties of bipolar plates as an alternative to the permeable and brittle graphite plates in traditional VRFB systems, those approaches are still initially complex and costly because they require additional operating equipment at specific environment conditions, e.g., specific conditions for temperature, pressure, and species

ratios. The efforts also require more time to prepare the materials for specific requirements. In this new design, a thermoplastic material, PVC (Polyvinyl chloride), is used to replace the traditional graphite plate in VRFB. This material has great key technical advantages such as light weight, good mechanical strength, impermeability, resistance to weathering, chemical rotting, and corrosion [109]. Also, it can be cut, shaped, and joined easily in a variety of styles, which is important to make the flow field channels for electrolyte distribution in flow systems. Through conducting many tests such as cycling, system efficiencies (columbic, voltage, and energy), polarization, and impedance measurements, the performance of the new cell is compared with the traditional single VRFB cell at different operating conditions.

2. DETAILS OF THE EXPERIMENTAL WORK

Two lab-scale with the single-cell configuration of VRFB have been designed, fabricated and tested in this study. The first one is the traditional design cell, referred as (TD) in the future discussion (the most common flow cell design used among the VRFB community research), which uses a graphite plate to engrave the flow field channels. The cell is assembled from the following components: proton exchange membrane, 50×50 mm^2 area (Nafion 117, and 0.183 mm thickness-Fuel Cell Store, Texas, USA); two symmetric electrodes of graphite felt, GFA6 of 50×50 mm^2 area as cathode and anode (SGL Technologies GbH) with 6 mm total thickness and specific resistance of 0.12 Ohm.cm; electrolyte distributors (flow field channels) to divide the electrolyte uniformly across the active area of the VRFB, which patterned with serpentine pattern on black graphite plate from (McMaster-Carr, USA) that can serve as a current collector too; gaskets and electric insulators are made of PTFE (polytetrafluoroethylene) from (McMaster-Carr, USA) and are, respectively, utilized to avoid electrolyte leakage among the assembled components and to prevent electronic current to go away from flow field plate to endplates; two Garolite sheets from (Fuel Cell Store, Texas, USA) with 120×120 mm^2 outer dimensions offering excellent strength and good electrical insulating qualities were used as endplates with a total of 12 bolts distributed in a uniform way along the endplate boundary to compact the cell components with no leaking; finally, a high-density polyethylene (HDPE) material for tubing, compression fittings (1/8 NPT × 1/4 inches OD tube), and tank, was used to feed the electrolyte solution into the cell stack from external tanks and vice versa by two pumps from (SMART Digital DDA7.5-16AR-PVC/V/C, Grundfos, Bjerringbro, Germany). The second cell refers to the new design

(ND) in which a thermoplastic material, PVC, from McMaster-Carr, 12.7 mm thickness and 120 mm side length, was used to replace the graphite plate. Almost all of the same components that are used in TD were applied in ND except some extra ones. The extra components are as follows: gaskets (which are avoided by making a square pocket at specific depth, 5mm), insulators (as the PVC is a good dielectric material), and end plates (as PVC is hard enough to provide assembling force), all of which makes this design easier to assemble, lighter, more mechanically strong, and more cost-effective. Based on same exterior dimensions of the assembled cells (120×120 mm^2), the utilized electrode area and membrane in ND are larger than in TD (80×80 mm^2 vs. 50×50 mm^2) respectively. All the geometric details of TD and ND are presented in Figure 2.1 (a) and Figure 2.1 (b), respectively, whereas the assembled cells of both designs are shown Figure 2.1 (c).

The flow field plates of each design include flow channels of 4×2 mm^2 cross section area with a land width of 7.5 mm among the channels. Also, one graphite rod material from (McMaster-Carr, 1/4 inches thickness and 2.5 inches side length) was fixed in the new design through each PVC compartment to serve as a current collector. The depth of the PVC pocket (where the felt electrode sits in) was purposely made less than the original thickness of the electrode (6 mm) to accomplish approximately 16.5% compression ratio. Since increasing the compression ratio results in the high-pressure drop (high pumping power) due to the reduction in felt permeability, the graphite felt electrode compression ratio was limited to 1 mm.

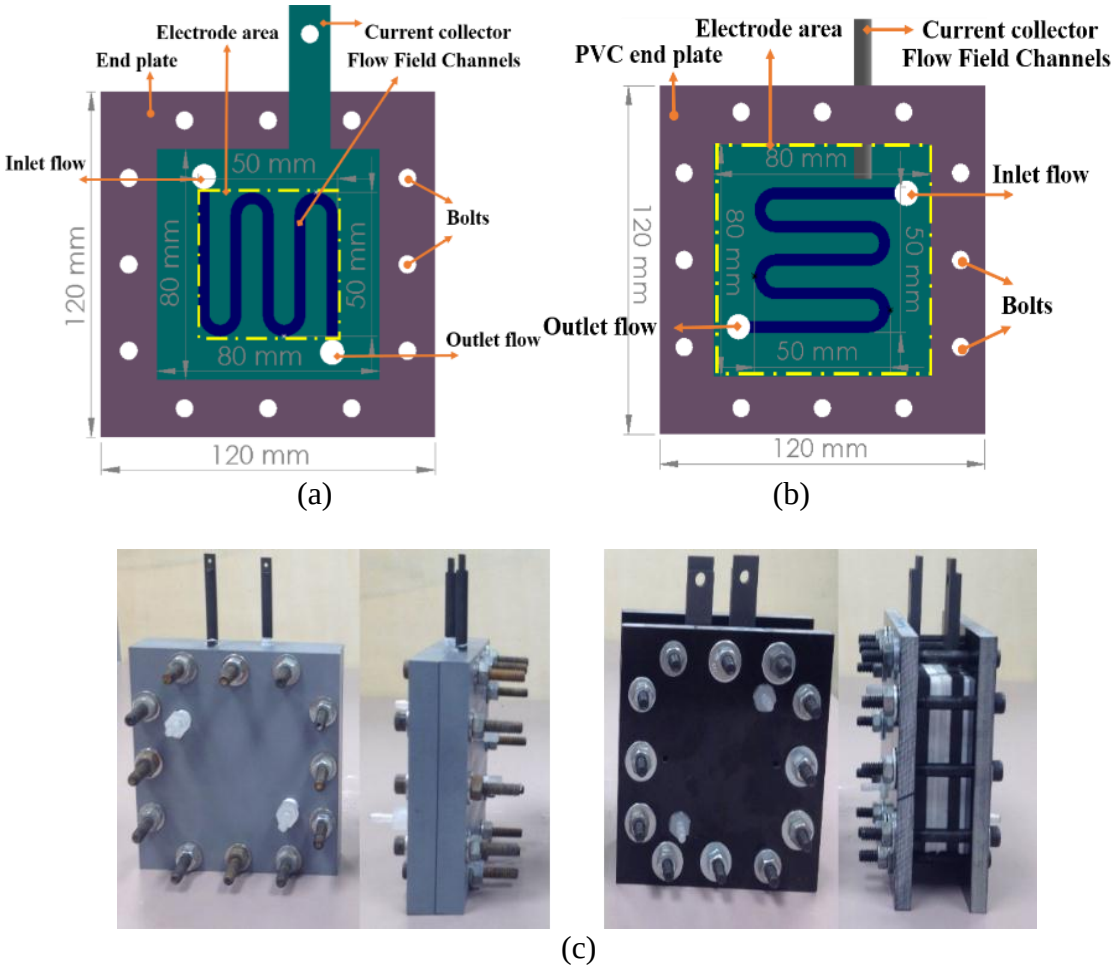

Figure 2.1. Geometrical details of the two single VRFB cells (a) TD cell at 50×50 mm^2 electrode area, (b) ND cell at 80×80 mm^2 electrode area, (c) Cells assembly: ND (left), TD (right).

For both prototypes, the electrolyte solution was prepared by dissolving 1.04 M $VOSO_4.xH_2O$ (99.9% wt. purity, Alfa Aesar) in 4 M sulphuric acid solution to get the electrolyte V^{4+}. Each tank has 100 ml of anolyte and catholyte, which were pumped to the cell electrodes from tanks and vice versa by two pumps. Constant lab temperature, around 24 ^oC, was observed during all tests. The battery was regarded as fully charged after being charged constantly at 1.75 V until the current density dropped to 40 mA/cm^2.

In the first charging (where 100 ml V^{4+} electrolyte solution was placed in anode side tank and 200 ml was placed in cathode side tank), V^{4+} was transformed into V^{5+} and V^{2+} in both solutions (catholyte and anolyte), respectively. Then, half of the catholyte amount was taken away after observing new colors on both sides (i.e., violet in the anode side and yellow on the cathode side).

The cell columbic efficiency, CE, represents the fraction of total current that is produced by the desired reactions (low CE indicates the strong presence of unwanted secondary reactions); the voltage efficiency, VE, reflects all combined voltage losses that reduce the operating voltage of the cell below the theoretical equilibrium voltage of the VRFB cell; and the energy efficiency, EE, was computed from EE = CE×VE. These types of efficiency were measured and compared for the two designs. During discharge, same charge current was applied to reach 1 V voltage value. All the experimental measurements such as cycling plots, polarization curves, and impedance analysis data are conducted with (4 Channel Battery Analyzer, BST8-20A-CST, MTI Corporation, CA 94804, USA) at a range of flow rates and applied currents. During the test time, leaking issues (which can have an impact on the cell performance) were not observed except some amount of electrolyte leakage from the graphite plates was present due to their permeability. Results from these experiments are discussed below.

3. RESULTS

3.1. PERMEABILITY OF PVC AND GRAPHITE BIPOLAR PLATES

One of the main design criteria of the excellent bipolar plate is its low permeability to the electrolyte. As shown in Figure 3.1(a) and Figure 3.1(b), a simple test was done by soaking the PVC and graphite plates (after the test was completed) in distilled water to demonstrate the electrolyte leakage from each plate. For PVC plates, no electrolyte was found in the distilled water after approximately 100 hrs. While the graphite plate showed some amount of electrolyte in the distilled water just after a couple of hours, it was also found that the electric conductivity was much lower after utilizing the graphite plate than before the test started. It is obvious that the PVC plate cannot allow the electrolyte to penetrate in a perfect way. In addition, Figure 3.1(c) and Figure 3.1(d) clearly show how the graphite flow field plate suffers from the electrolyte penetration from the sides and back, respectively.

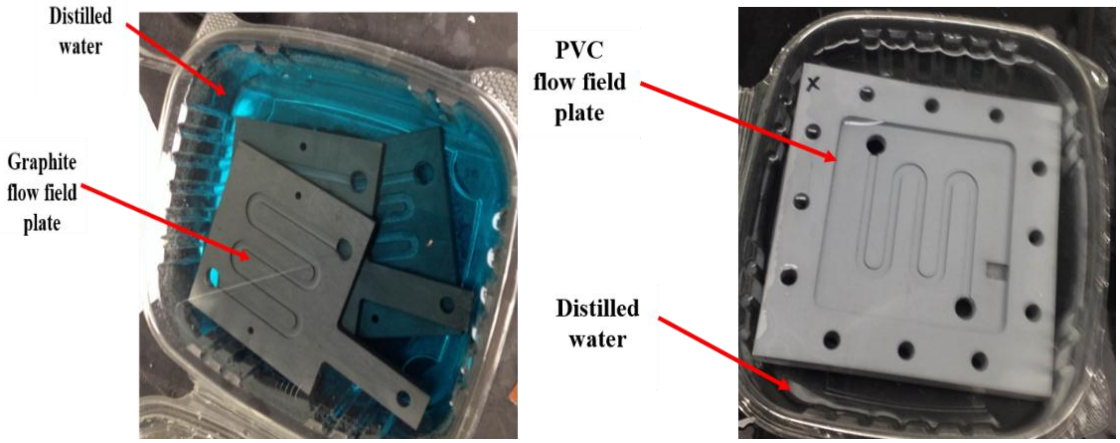

(a) (b)

Figure 3.1. Actual comparison between the graphite and PVC plates (a) Soaked PVC plate in distilled water, (b) Soaked graphite plate in distilled water, (c) Leakage from the graphite sides, (d) Leakage from the graphite back.

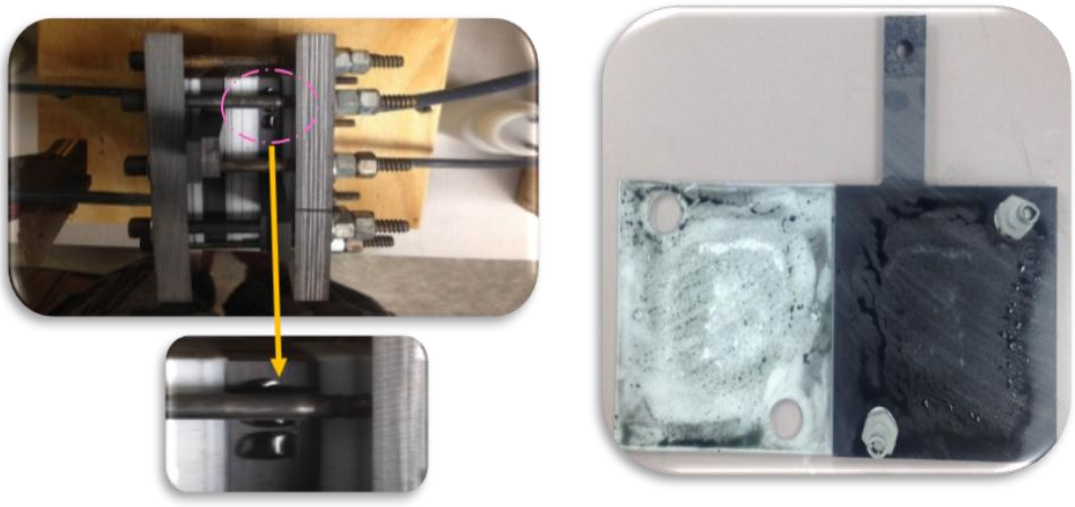

(c) (d)

Figure 3.1. Actual comparison between the graphite and PVC plates (a) Soaked PVC plate in distilled water, (b) Soaked graphite plate in distilled water, (c) Leakage from the graphite sides, (d) Leakage from the graphite back (cont.).

3.2. CHARGE/DISCHARGE CYCLING TEST

Primarily, the cycling test is able to illustrate long term operation stability and can provide performance information including capacity, voltage, and energy efficiencies in VRFBs [110, 111]. The performance of a flow battery is mostly studied by galvanostatic charge/discharge cycles of the redox electrolyte. During the charging process, a slow increment in voltage with time occurs until the remaining uncharged ions become too low. Then, a quick increase in voltage occurs to reach the upper limit voltage, which represents the final status of this process. In a similar way, during the discharging process, there is a slow decrement in voltage with time until not enough ions are available to support the discharging rate. Then, a rapid decrease in voltage appears to reach the lower limit voltage, which is considered the final condition of this process.

Two single VRFB cell configurations (TD and ND) are typically assembled, as described in Section 2 and performed in a constant current mode. During cycling, a constant current of 500 mA was applied at 1.7/1 V of (upper/lower) potential limits and maintained at 35 mL/min volumetric flow rate. The voltage was recorded after each time period (20 seconds) during cycling tests. Four charge/discharge cycles were initially programmed at the aforementioned experimental conditions. The charge/discharge cycles of TD cell (shown in Figure 3.2(a)) exhibited high electrochemical reversibility as anticipated for VRFB systems [112]. Single charge and discharge potential plateaus were observed, indicating that a single reaction occurred in each half-cell of the flow battery.

The charge/discharge behavior of the ND unit cell is shown in Figure 3.2(b), and it also exhibited high electrochemical reversibility with a single charge/discharge potential plateaus. In fact, both cells showed excellent stability over the four cycles; however, the total run time to achieve four cycles in the TD cell is less than the ND cell. The decrease in time was associated with the concentration and capacity loss effects, which come mainly from the shortage in vanadium ions due to electrolyte penetration in TD, whereas longer operating period in ND is observed due to more available vanadium electrolyte.

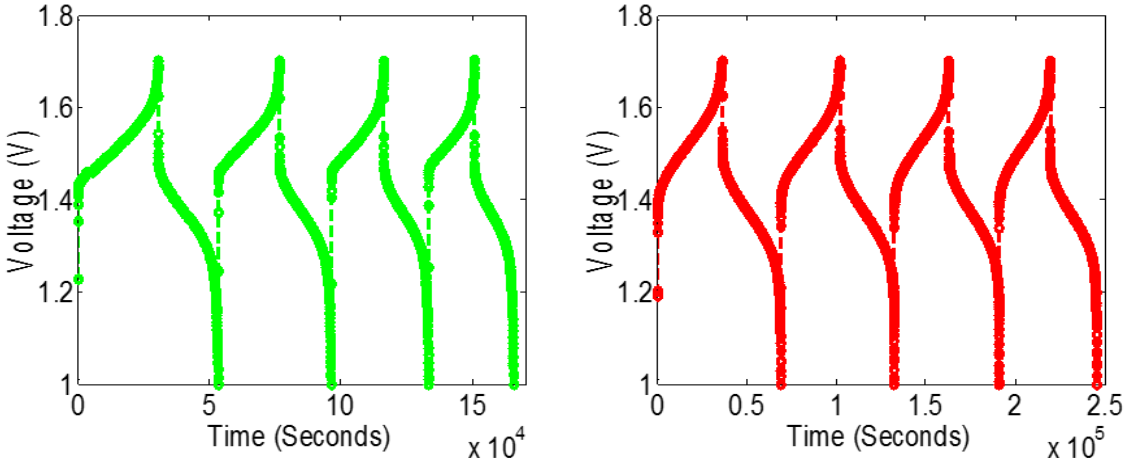

Figure 3.2. Charge/discharge cyclic curves of VRFB. (a) TD cell, (b) ND cell.

Specific information about kinetics, cell overpotential, and battery efficiencies can also be extracted from battery cycling. CE and EE (VE will be presented with impedance analysis in another section) for the TD and ND cells at 500 mA applied charge/discharge current and maintained at 35 mL/min electrolyte flow rate are presented in Figure 3.3. On average, the ND exhibited a CE of ca. 90.57% and EE of ca. 79.03% for four charge/discharge cycles. The loss in CE was likely associated with a decrease in the concentration of active species due to cross-over through the Nafion 117 membrane and also to parallel side reactions inside each electrode. For the TD cell, the average CE and EE efficiencies were ca. 84.53% and ca. 74.84%, respectively, for four cycles at same operating conditions of ND. The CE loss was more noticeable in TD cell as compared to the ND cell (~ 9% vs. ~ 15%), which can be attributed, besides the ion-crossover through the membrane, to the fact that TD has a big chance to lose actual vanadium species due to the permeability of the graphite plate and to the possibility of V^{+2} ion oxidation, which comes from the way of assembling TD cell, thus, leading to a

reduced amount of electrical charge (main factor in finding CE). Since the CE of TD cell is lower than the ND cell and the VE is higher (as will see), the energy efficiency (EE), which is the combination of CE and VE, was lower in TD as compared to the ND cell.

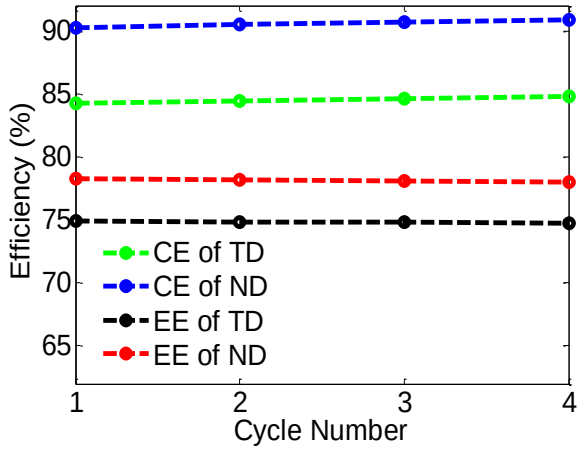

Figure 3.3. Columbic and energy efficiencies for charge/discharge cycles for both designs.

3.3. BATTERY STORAGE CAPACITY

It was reported that continued production of H_2 and O_2 inside electrodes during cycling besides vanadium ions and water crossover through the membrane (which can result in an imbalance of SOC in both sides) are the main reasons for battery fading [21]. For both prototypes and specifically the ND configuration, an acceptable energy efficiency was demonstrated (Figure 3.3). The energy efficiency of the VRFB cells is directly linked to the battery capacity. Capacity is defined as the amount of electrical charge that can be removed from the battery under defined discharge conditions, and it is closely related to the concentration and volume of the redox electrolyte used in the VRFB system. The stability of capacity in a battery is of great importance for the long-time

application. The capacity of the two cells was also investigated over battery cycling in this work. To do so, the ratio of the discharge capacity of each n^{th} cycle to the 1^{st} discharge capacity was considered. The evolution of the relative discharge capacity vs. cycle number plot of both cells was presented in Figure 3.4, where both redox systems exhibited capacity fade over battery cycling. The rapid capacity decay and low columbic efficiency in battery TD were caused by vanadium crossover during its operation, likely V^{+2} ion oxidation, and electrolyte shortage due to its penetration through the graphite plate. It has been proved that the positive and negative electrolyte can become unbalanced due to vanadium crossover and water osmosis [33], thus causing efficiency and capacity loss in the battery. The ND cell exhibited a continuous capacity fade over battery cycling in a similar trend to the TD cell. Nonetheless, the ND cell demonstrated a slower rate of the loss in capacity than the TD cell. For instance, the capacity of the TD cell faded 35% by cycle 4 as compared to 20% in the ND cell by cycle 4 (Figure 3.3). It is important to recall that the charge/discharge cycle experiments were performed using cut-off potential limits; therefore, any cell polarization led to an increase in the total overpotential, thus leading to an apparent reduction of capacity.

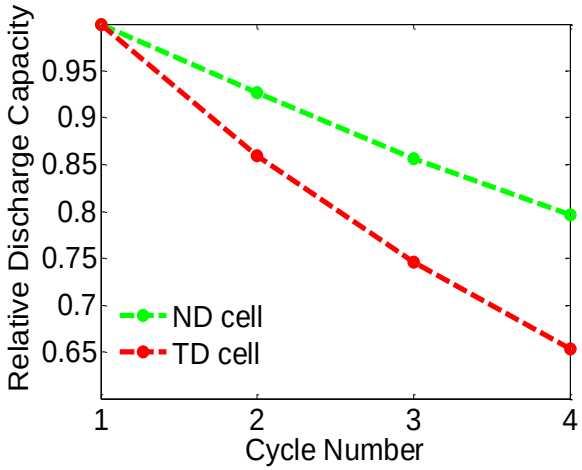

Figure 3.4. The relative discharge capacity of the VRFB ND and TD cells.

3.4. THE NEW BATTERY BEHAVIOR AT DIFFERENT OPERATING CONDITIONS

To further understand the behavior and performance of the new design ND, a typical single charge/discharge cycle tests at three different currents listed in Table 3.1 were performed. It was observed in Figure 3.5(a) that the charge/discharge time (i.e., capacity) decreases dramatically with increasing current. The capacity decay at higher currents can be associated with the increase in overpotential losses as a result of the fast rate of charging and discharging, which lowers the desired potential value.

Figure 3.5(b) shows the corresponding columbic, voltage, and energy efficiencies at the same currents. When the applied current increased, the CE was increased due to the high rate of electrolyte consumption, which in turn minimizes the electrolyte crossover through the membrane. Also, it can be seen that the VE was decreased at higher currents values, which can be attributed to the elevated ohmic overpotential losses [113]. The EE represents the product of CE and VE [114, 115], and since CE is increasing at a rate less than the rate of VE decreasing, EE decreases as current increases.

Table 3.1. Charge/Discharge test conditions.

Properties	Value
Charge /discharge value (V)	1.7-1
Charge /discharge current (mA)	250, 500, and 750
Electrode area of single cell (mm^2)	6400
Thickness of graphite felt electrode (mm)	6
Amount of electrolyte in each tank (ml)	100
Volumetric flow rate (ml/min)	35

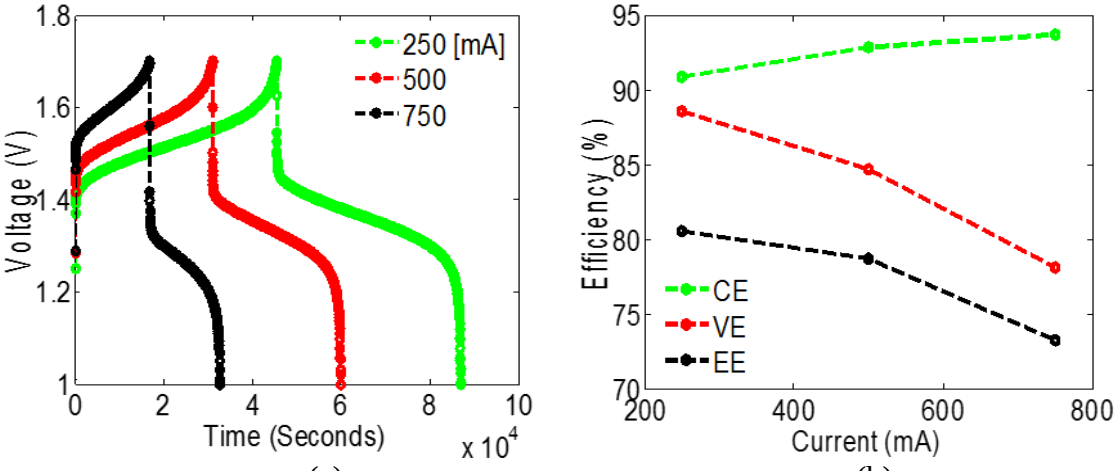

(a) (b)

Figure 3.5. The new cell performance at different currents (a) Single cycle test, (b) Cell efficiencies CE, VE, and EE.

3.5. POLARIZATION CURVES

As mentioned in Section 3.2, cycling tests can provide performance information including capacity, voltage, and energy efficiencies in VRFBs [39]. However, the cycling test is limited to identifying the factors causing performance loss in a VRFB system. The polarization curve is a plot of battery potential vs. it's current/current density under given operating conditions.

The discharging polarization curves of the two designs was measured at 25 ml/min flow rate for comparison purposes to illustrate battery performance under practical conditions, i.e., various ranges of discharge currents. Polarization data were obtained at steady-state under potentiostatic control. The measurements of discharge polarization curves were achieved at fully charged battery condition, where steady current of 40 mA at a cell potential of 1.7 V was maintained. For both designs, the cells were discharged under a range of current values until 0.1 V lower limit voltage was reached. A half-minute was specified for each current during discharge; then, the cell was set up to two minutes as a rest time to represent its open circuit potential (OCP). To get the data points on the polarization curve, the measured voltage over each half-minute was averaged during this period, which represents one point on the curve at the specified current. The generated mass transport limiting currents from the TD and ND were, respectively, 3250 and 6000 mA for the graphite felt electrodes, as shown in Figure 3.6(a). This difference in maximum limiting current can be attributed to the difference in electrochemical surface area in both cells. The ND cell, which is based on the same outer dimensions of the TD cell, can expose more surface area (80×80 mm) as compared to the TD cell (50×50 mm), which results in a more local current. At a given current across the battery, the high surface area in the ND cell can reduce the local current on the surface of the electrode. The lower current density at the electrode surface would lead to lowered activation overpotential loss.

Figure 3.6(b) presents the corresponding output power curves for both cells. The output power has a similar tendency as the cell voltage, where the maximum power was obtained as ~ 2561 mW in the TD and ~2750 mW in the ND (the peak power increases

by 7.38%). Also, a wider range of power was observed in ND than in TD due to the higher produced current.

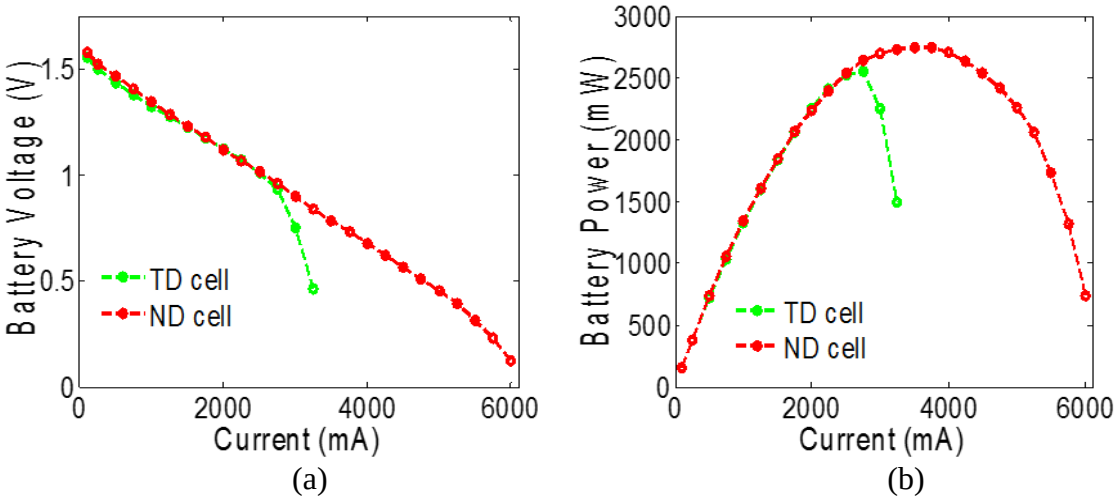

Figure 3.6. Discharge polarization curves of the two designs at 25 ml/min flow rate, (a) Battery discharge voltage, (b) Battery output power.

For the ND cell, the effects of electrolyte transport on polarization were further investigated by systematically varying the electrolyte flow rate. The flow rate was controlled by the setting of dosing pumps ranging from 1 to 45 ml/min.

The results of the multi-voltage polarization curves and their corresponding output powers are shown in Figure 3.7(a) and Figure 3.7(b), respectively. High electrolyte feed rate can obviously improve mass transport in electrodes, which means that concentration overpotentials are substantial and a very swift electrochemical reaction occurs inside each graphite felt. It is reasonable that higher flow rate into the cell can bring more active species onto the electrode surface to support the redox reaction to

generate higher current. It is noticed that the limiting current can be increased (from 425 to 650 mA) at an analog range of flow rates (from 1 to 45 ml/min).

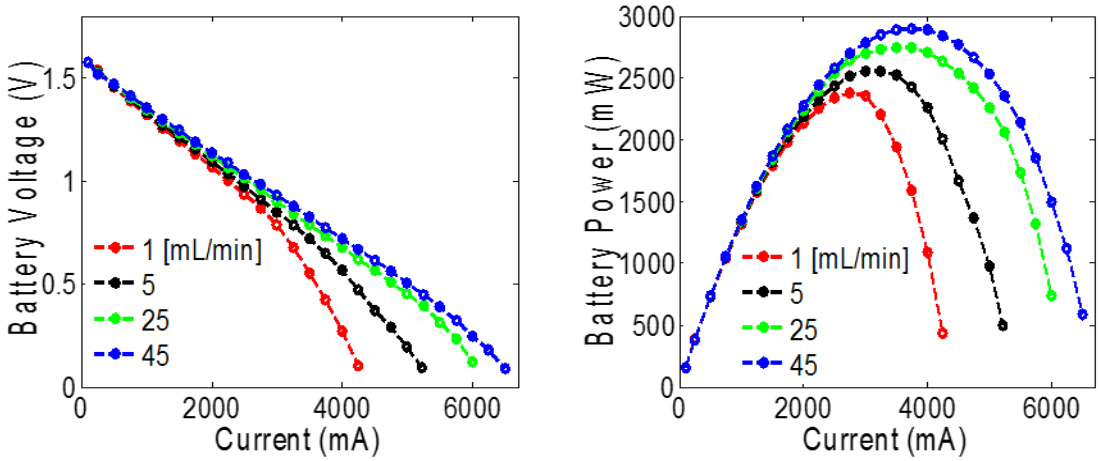

Figure 3.7. Discharge polarization curves of the ND at a range of electrolyte feed rates (a) Battery discharge voltage, (b) Battery output power.

Despite the improvement in the output current and power for the new design, it is important to notice the approximately linear shape of the polarization curves, where the normal mass transport region of polarization curves is not shown clearly as we should expect from the polarization curve due to the sharp slope of potential drop. Such a phenomenon is mainly caused by the rapid change in the ohmic resistance as discussed below.

It was observed that adopting graphite felt as a porous electrode in vanadium redox flow battery systems was the main reason of ohmic resistance that affects the cell performance, which becomes more dominant at higher applied currents due to the relatively high electrode thickness [116]. Generally, the porous electrode, flow field plate

bulk resistivities, and the contact resistance between them (the latter was considered the main source of internal ohmic resistance, IOR, of VRB) were considered the most parameters that affect the cell performance. We guess this new design has high IOR (as can be seen from the Electrochemical Impedance Spectroscopy (EIS) test results next Section) due to the large contact resistance (no much contact) between the small portion of graphite rod (which works as a current collector) inside PVC compartment and the graphite felt electrode. Loose contact between the current collector, graphite rod, and the graphite felt electrode inside the flow field house can lead to significant contact resistance. The sharp potential decay becomes more and more significant at higher polarization currents due to the increased impact of contact resistance, leading to higher overpotentials.

3.6. ELECTROCHEMICAL IMPEDANCE SPECTROSCOPY TEST (EIS)

In order to further study the electrochemical behavior of the ND, an EIS test was conducted under almost fully charged operating conditions at 1.7 V and 35 ml/min. The EIS was conducted with potential-controlled electrochemical impedance spectroscopy over an AC frequency range of 20 kHz to 0.01 Hz and with 10 mV perturbation amplitude. During an EIS measurement, small AC perturbation/signals (potential or galvanic) of varying frequency are applied to the electrochemical (flow battery) device, and the resulting ratios of voltage to current are determined and plotted as implicit functions of signal frequency. [36, 117]. The Nyquist plots for the two prototypes were plotted in Figure 3.8(a), where the original data were fitted by a circuit diagram model R(CR)(CRW) [118]. The high-frequency intercept at Z_1 axis corresponded to the battery internal resistance, which can reveal the ohmic loss during battery operation. It can be seen that the ND cell has higher ohmic resistance (~ twice) compared to the TD (0.27 vs.

0.135 Ω, respectively), which could be mainly due to the high contact resistance, as discussed above. In addition, Figure 3.8(b) demonstrates the voltage efficiency vs. cycle number of ND and TD cells. It can be seen that the average VE over four cycles of ND cell (~86.21%) is lower than the TD cell (~88.55%). This difference can be associated with the ohmic losses registered for each type, where the EIS test showed higher ohmic resistance in the ND cell. Both configuration types also started to exhibit a slight voltaic efficiency decay (associated with the increases in the cell overpotential). The EE fade shown in (Figure 3.4) was related to the increases in the cell overpotential that directly affected the VE of the VRFB cells. Therefore, it was suggested that the storage capacity of the VRFB cells was decreasing over time.

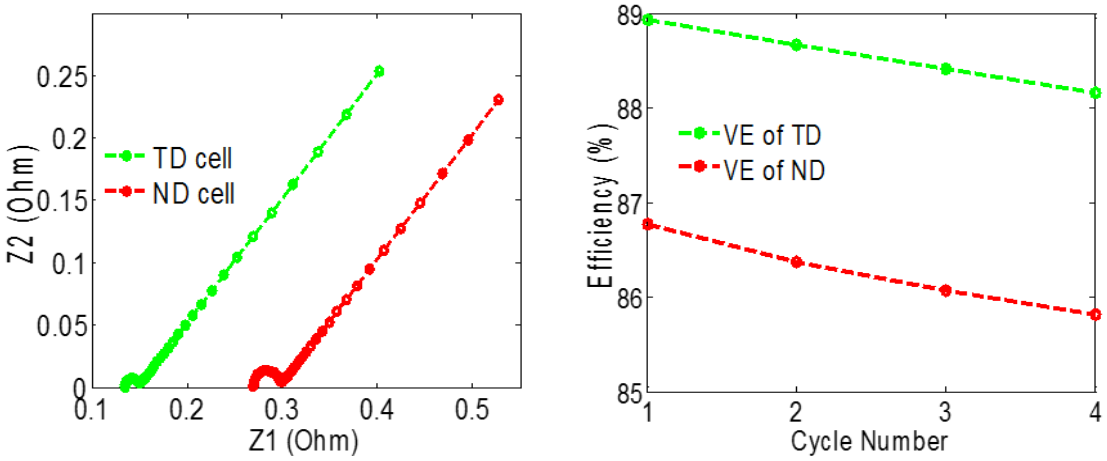

(a) (b)

Figure 3.8. Comparison of the impedance and voltage efficiency of the ND and TD cells (a) EIS measurements, (b) Voltage efficiency vs. cycle numbers.

3.7. CONTACT RESISTANCE IMPROVEMENT

In this section, a second-long PVC cell (LC) has been fabricated and tested with the goal of reducing the contact resistance between the current collector and electrode. This cell shares the same components of the ND cell (described above) except the shape and the size of electrode area (255 × 28 mm^2), as shown in Figure 3.9(a). A pure compressible graphite sheet of 1/16-inch thickness from McMaster-Carr was used to serve as a flow field channel and current collector. Since the electrode area of the ND (64 mm^2) is less than the LC (71.4 mm^2), the polarization potentials and their corresponding powers were measured and compared against the current density (mA/cm^2) at the same practical operating conditions, as shown in Figure 3.9(b). It can be seen that higher current density can be obtained from the modified cell, LC, due to the larger contact area between the current collector and electrode, resulting in lower contact resistance. For instance, the maximum current density of the ND cell at 1 and 45 ml/min volumetric flow rates is 66.41 and 101.56 mA/cm^2, respectively, whereas it is 73.53 and 115.55 mW/cm^2 for the LC cell at the same flow conditions. Also, the maximum obtained power density of the ND cell at the same flow conditions is 37.25 and 45.33 mW/cm^2, respectively, whereas it is 43.59 and 53.67 mA/cm^2 for the LC cell. The improvement in the maximum current density and output power density can be attributed to the new configuration of current collector, which ensures more contact area between the current collector and electrode surface, reducing the internal resistance of the cell. The impedance analysis test of the LC cell was also conducted and compared with the ND cell, as shown in Figure 3.9(c). A lower ohmic resistance in LC than in ND was observed (0.18 vs. 0.27 Ω, respectively).

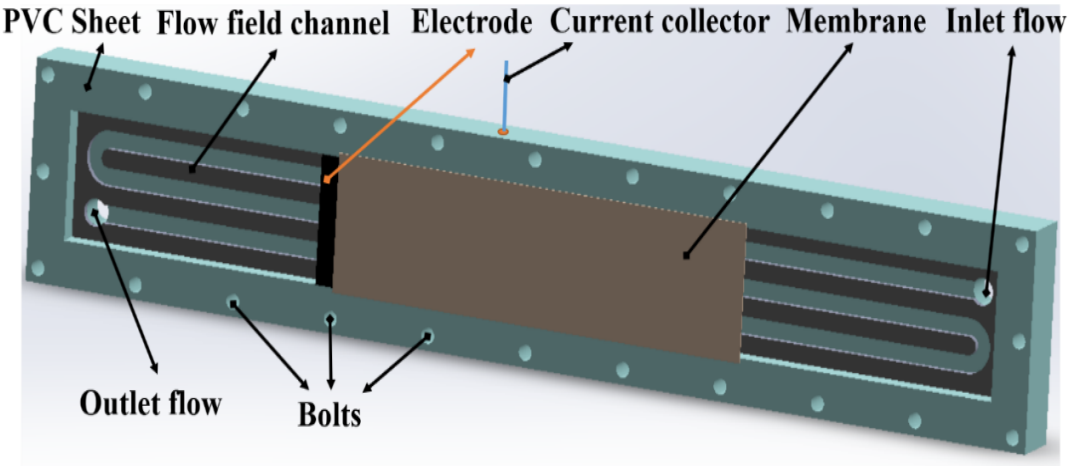

(a)

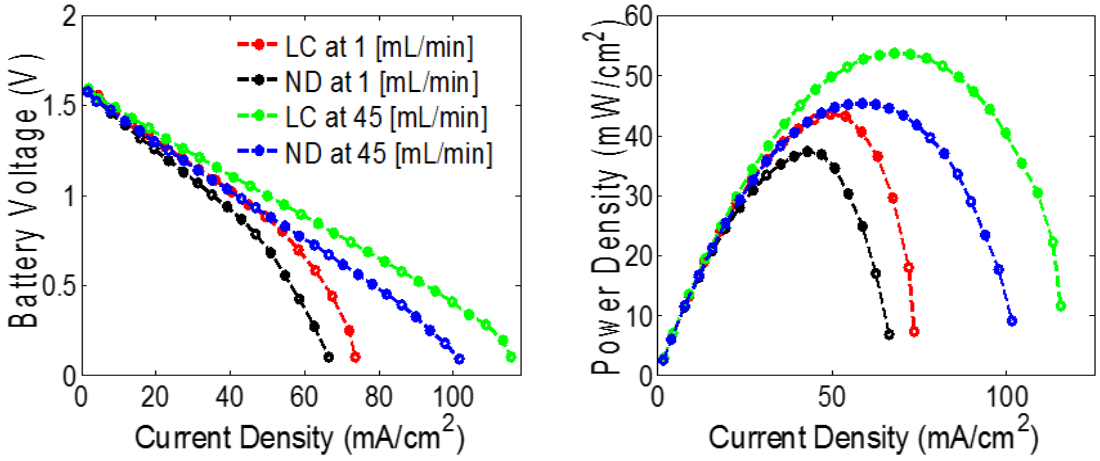

(b)

Figure 3.9. The long PVC cell design (a) The new LC configuration and components, (b) The polarization potential (left) and corresponding power density (right) measurements of LC and ND cells, (c) The impedance analysis data of LC and ND cells.

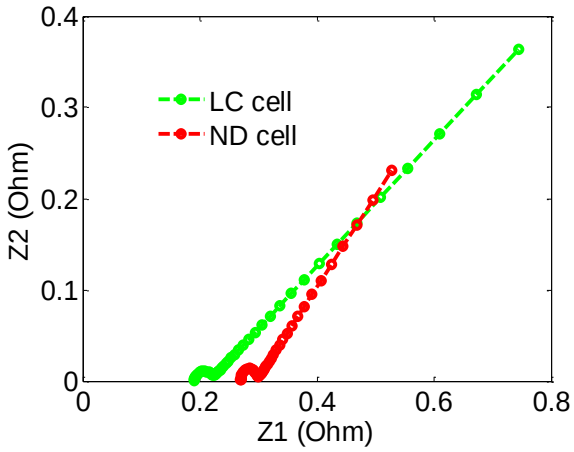

(c)

Figure 3.9. The long PVC cell design (a) The new LC configuration and components, (b) The polarization potential (left) and corresponding power density (right) measurements of LC and ND cells, (c) The impedance analysis data of LC and ND cells (cont.).

3.8. ECONOMIC PERSPECTIVES ANALYSIS

Based on same exterior dimensions of TD and ND designs (i.e., 120×120 mm), a cost comparison has been performed. The ND single VRFB cell (based on PVC material) shares the same initial cost of some components in the TD cell (based on graphite plate material) such as electrolyte solution amount, external tubing, membrane, bolts, electrodes, pumps, labor, molds, and energy consumption to prepare the solution and machine the flow field. However, other components have different costs, and Table 3.2 shows the cost difference between the two designs. It is also worth mentioning that the gross weight of the new single cell design is 0.78 kg without any leaking issues, while the traditional cell weighs 1.1 kg, besides the issues of electrolyte leaking from the graphite plate, as discussed in Section 3.1. As a result, the new design assembly is more cost-effective, requires fewer components, and has less weight than the traditional setup. In

another word, the new design cost represents ~ 17% of the traditional cell for the non-similar components, and ~ 65% including all components.

Table 3.2. Non-similar components cost comparison.

Single cell components	**Traditional design cost in dollar**	**New design cost in dollar**
Graphite plate OR PVC sheet	23.7×2	9.96×2
Gaskets	7	----
Insulators	7	----
End plates	51×2	----
Current collectors	-----	7.47
All other components	-----	----
Total	$ 163.4	$ 27.39

4. CONCLUSIONS

A new cost-effective assembly design for VRFB applications was fabricated and tested in the current work. The new cell shows perfect proof of preventing electrolyte leakage during the 100 hours of permeability test as compared to the traditional cell design. It is also more lightweight, costs less, is easy to assemble, and has more mechanical strength than the brittle graphite plate, which ensures longer lifetime, especially in harsh environments exposed to shocks and vibrations. The performance of this assembly after four cycles showed higher average columbic and energy efficiencies than the traditional cell, which leads to less capacity degradation during cycling at the same operating conditions. Polarization measurements of this new design showed that high feed rate of electrolyte solutions into both sides of a battery cell can immediately increase output capacity of the battery. A higher power was obtained with the new cell as a result of the higher output current due to the larger electrochemical surface area, which is utilized in this design based on the same outer dimensions for both cells.

The single cycle test of the ND cell further demonstrated the applicability of this design in VRFB applications by reflecting the normal qualitative behavior of the traditional VRFB system; however, polarization curves at different flow rates showed a quick drop in voltage before reaching the mass transport region, which could reduce the limiting currents and corresponding output power due to the high IOR. This issue has been treated by introducing a new design, LC, in which the contact resistance between the current collector and electrodes was reduced, and the obtained results showed higher current and power densities compared to the ND cell. Many other approaches can be implemented to minimize the contact resistance, such as utilizing either high electrical

conductive current collectors or covering the rib areas among flow channels with a good electrical conductive deposit, which can provide more active contact areas with graphite felt electrode to carry more electrons into and out of the cell core.

REFERENCES

1. Bartolozzi, M., *Development of redox flow batteries. A historical bibliography.* Journal of Power Sources, 1989. 27(3): p. 219-234.

2. Dunn, B., H. Kamath, and J.-M. Tarascon, *Electrical energy storage for the grid: a battery of choices.* Science, 2011. 334(6058): p. 928-935.

3. Sum, E., M. Rychcik, and M. Skyllas-Kazacos, *Investigation of the V (V)/V (IV) system for use in the positive half-cell of a redox battery.* Journal of Power sources, 1985. 16(2): p. 85-95.

4. Wang, W., et al., *Recent progress in redox flow battery research and development.* Advanced Functional Materials, 2013. 23(8): p. 970-986.

5. De Leon, C.P., et al., *Redox flow cells for energy conversion.* Journal of Power Sources, 2006. 160(1): p. 716-732.

6. Moore, M., et al. *Sensitivity Analysis of Design Variables of an All-Vanadium Redox-Flow Battery*. in *Meeting Abstracts*. 2011. The Electrochemical Society.

7. Ito, H., et al., *Effect of through-Plane Polytetrafluoroethylene Distribution in a Gas Diffusion Layer.* ECS Transactions, 2014. 64(3): p. 501-508.

8. Cooper, J.S., *Design analysis of PEMFC bipolar plates considering stack manufacturing and environment impact.* Journal of Power Sources, 2004. 129(2): p. 152-169.

9. Heinzel, A., et al., *Injection moulded low cost bipolar plates for PEM fuel cells.* Journal of Power Sources, 2004. 131(1): p. 35-40.

10. Heinzel, A., F. Mahlendorf, and C. Jansen, *Bipolar plates.* Fuel Cells—Proton-Exchange Membrane Fuel Cells, Elsevier, New York, 2009.

11. Wind, J., et al., *Metallic bipolar plates for PEM fuel cells.* Journal of Power Sources, 2002. 105(2): p. 256-260.

12. Davies, D., et al., *Stainless steel as a bipolar plate material for solid polymer fuel cells.* Journal of Power Sources, 2000. 86(1): p. 237-242.

13. Wang, H. and J.A. Turner, *Ferritic stainless steels as bipolar plate material for polymer electrolyte membrane fuel cells.* Journal of Power Sources, 2004. 128(2): p. 193-200.

14. Hornung, R. and G. Kappelt, *Bipolar plate materials development using Fe-based alloys for solid polymer fuel cells.* Journal of Power Sources, 1998. 72(1): p. 20-21.

15. Makkus, R.C., et al., *Use of stainless steel for cost competitive bipolar plates in the SPFC.* Journal of power sources, 2000. 86(1): p. 274-282.

16. Cho, E., et al., *Characteristics of composite bipolar plates for polymer electrolyte membrane fuel cells.* Journal of Power Sources, 2004. 125(2): p. 178-182.

17. Kuan, H.-C., et al., *Preparation, electrical, mechanical and thermal properties of composite bipolar plate for a fuel cell.* Journal of Power Sources, 2004. 134(1): p. 7-17.

18. Lee, Y.K., et al., *Activation energy and curing behavior of resol-and novolac-type phenolic resins by differential scanning calorimetry and thermogravimetric analysis.* Journal of applied polymer science, 2003. 89(10): p. 2589-2596.

19. Lee, N.J., et al., *Development of carbon composite bipolar plates for vanadium redox flow batteries.* Bulletin of the Korean Chemical Society, 2012. 33(11): p. 3589-3592.

20. https://en.wikipedia.org/wiki/Polyvinyl_chloride. Available from: https://en.wikipedia.org/wiki/Polyvinyl_chloride.

21. Watt-Smith, M.J., et al., *The importance of key operational variables and electrolyte monitoring to the performance of an all vanadium redox flow battery.* Journal of Chemical Technology and Biotechnology, 2013. 88(1): p. 126-138.

22. Skyllas-Kazacos, M., et al., *Characteristics and performance of 1 kW UNSW vanadium redox battery.* Journal of Power Sources, 1991. 35(4): p. 399-404.

23. Shinkle, A.A., et al., *Electrode kinetics in non-aqueous vanadium acetylacetonate redox flow batteries.* Journal of Applied Electrochemistry, 2011. 41(10): p. 1191-1199.

24. Tang, A., J. Bao, and M. Skyllas-Kazacos, *Dynamic modelling of the effects of ion diffusion and side reactions on the capacity loss for vanadium redox flow battery.* Journal of Power Sources, 2011. 196(24): p. 10737-10747.

25. Sun, C., et al., *Investigations on transfer of water and vanadium ions across Nafion membrane in an operating vanadium redox flow battery.* Journal of Power Sources, 2010. 195(3): p. 890-897.

26. Hwang, G.-J. and H. Ohya, *Crosslinking of anion exchange membrane by accelerated electron radiation as a separator for the all-vanadium redox flow battery.* Journal of Membrane Science, 1997. 132(1): p. 55-61.

27. Chen, D., et al., *Selective anion exchange membranes for high coulombic efficiency vanadium redox flow batteries.* Electrochemistry Communications, 2013. 26: p. 37-40.

28. Chen, D., et al., *Optimizing membrane thickness for vanadium redox flow batteries.* Journal of membrane science, 2013. 437: p. 108-113.

29. Xu, Q., T. Zhao, and C. Zhang, *Effects of SOC-dependent electrolyte viscosity on performance of vanadium redox flow batteries.* Applied energy, 2014. 130: p. 139-147.

30. Yuan, X., et al., *AC impedance technique in PEM fuel cell diagnosis—A review.* International Journal of Hydrogen Energy, 2007. 32(17): p. 4365-4380.

31. Kong, C.S., et al., *Influence of pore-size distribution of diffusion layer on mass-transport problems of proton exchange membrane fuel cells.* Journal of Power Sources, 2002. 108(1): p. 185-191.

32. Song, J., S. Cha, and W. Lee, *Optimal composition of polymer electrolyte fuel cell electrodes determined by the AC impedance method.* Journal of Power Sources, 2001. 94(1): p. 78-84.

III. DEVELOPMENT OF A DISTRIBUTED VANADIUM REDOX FLOW BATTERY FOR TRANSPORT SYSTEMS

ABSTRACT

In general, a vanadium redox flow battery (VRFB) is considered suitable only for stationary applications because of its low energy and power density. With a new design that can generate higher power per cell unit volume without material changes, however, VRFB can also open up the possibility of being applied to other fields such as transportation. This study consists of designing, fabricating, and testing two new types of VRFB configurations that can serve as distributed VRFBs for fully operational transport systems using two vanadium redox couples. The first design assembles into a tubular cell configuration, and the other solves the first design problems with a long rigid flat cell, which is impermeable PVC (polyvinyl chloride) sheet to replace the brittle and porous graphite flow plate. According to a comparative study using conventional flow battery, the new two designs provide significant benefits for transportation applications such as safety, space efficiency, and charge time.

Through tests including cycling, impedance analysis, and polarity under various load conditions for current and flow rate, the proposed design demonstrates that it can function as an energy storage device, comparable to conventional cells. In particular, tubular designs have shown that under certain geometric conditions, larger electrode active areas can be created than in planar shapes, resulting in higher power density. However, some improvements are still required, including the following: (1) reducing contact resistance between components; (2) applying a uniform pressure to the cathode and anode sides and designing a new configuration with different orientations to utilize

the entire electrode area; and (3) using a flow field channel to distribute the electrolyte flow in a uniform manner and minimize mass transport overpotential.

1. INTRODUCTION

The need to find a new source of clean energy with higher efficiency and less overall impact on the environment is growing with the increasing worldwide demand for energy. This has led to the development of high potential energy storage technologies [119-131]. Due to the desirable characteristics of vanadium redox flow battery (VRFB) such as long cycle life, design flexibility, energy and power separation, and tolerance to deep discharge, it is considered a new promising technology among various technologies for large-scale stationary applications [20, 35, 132, 133]. A VRFB can be broken into three main components: the anode, polymer membrane, and cathode. At the anode and cathode sides, the negative/positive couples (anolyte/catholyte) diffuse through a porous graphite felt electrode and they are circulated between the external tanks and the electrodes by a pump. The polymer membrane acts as an electrolyte and an electrical insulator, separating the anode and cathode sides while allowing proton transport. VRFB is an electrochemical energy conversion device that takes energy provided by vanadium redox couples (V^{2+}/V^{3+} in the negative and V^{4+}/V^{5+} in the positive half-cells) to produce a current of electrons (i.e., electricity). During discharge, an oxidation reaction in the anode side occurs and electrons are released. The electrons then move through an external wire to the cathode side, where the reduction process takes place to achieve positive work. During charge, the opposite direction of the redox reaction occurs, as depicted in Figure 1.1.

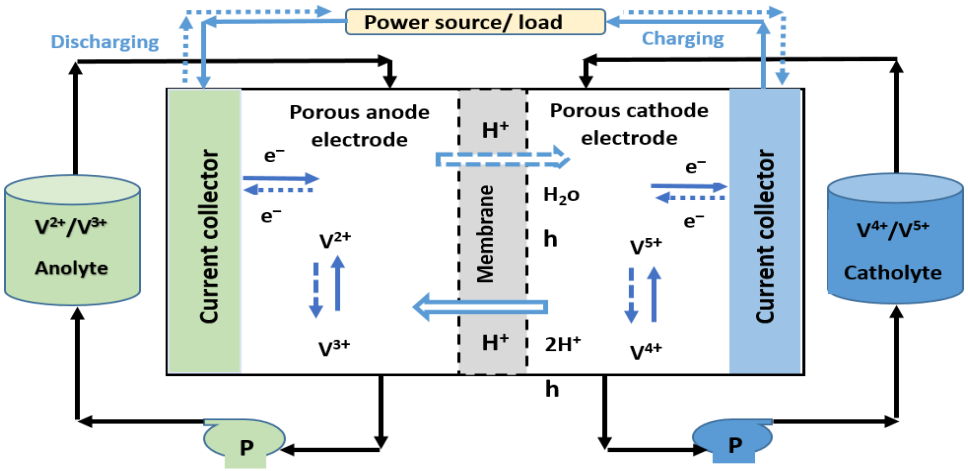

Figure 1.1. Schematic diagram of VRFB.

Despite the advantages of VRFB technology, many challenges still exist, such as effective flow control, cell/stack geometry structure, intrinsically low specific energy, economic efficiency, and improvement of new materials of cell components such as membrane, electrodes, and electrolytes to enhance the battery's system performance and its commercial application [62, 133-137].

Up to now, all research efforts (numerical and experimental work) has been focused on flat VRFB designs (planar geometries) because it is a straightforward design that uses a brittle and porous graphite flow field plate. Corresponding to the documented experimental work, different patterns of flow field channels such as parallel, serpentine, and interdigitated, have been achieved to study the overall VRFB performance, and the results showed that a cell with a serpentine pattern provided the best battery efficiency among them, which can be attributed to the dual impact of better voltage efficiency and lower pumping power losses [75]. The parallel flow field design of a VRFB was selected to describe the distribution of electrolyte solution through an experimental and numerical

study [77], and the simulated results were in good agreement with those obtained from experiment work. Temperature impact on the capacity degradation and columbic efficiency of a single cell VRFB setup has been conducted under different operating conditions [138], and it is found that increasing the temperature from 15 to 55 ^{o}C can increase both voltage efficiency and peak discharge power density, while current efficiency slightly decreases. A polarization study was performed to investigate the performance of two VRFB cells with a serpentine flow channel and without a flow field [28], and it was concluded that the kinetics and mass transport losses are not significant compared to the internal resistance losses for cells with a serpentine flow field.

The goal of this work is to develop a radical new flow battery cell optimized for use in electric vehicles or any other type of transport system that requires a clean power source by designing, fabricating, and experimentally testing novel tubular-shaped and long planar PVC configuration cells. A tubular-shaped VRFB has several advantages compared to a planar-shaped cell, namely (1) it can be performed at any orientation; (2) for specific geometries, it can provide a larger active area without increasing the overall cell volume; (3) it has lower fabrication cost because of decreased volume; and (4) it does not require other components such as gaskets, endplates, and bolts. The new flow battery systems are innovations that will create a new market and a valuable network of energy supplies for transport systems by resolving the key obstacles of current battery technology. The main obstacles involve long charging time, safety concerns, and poor cycle life. The key innovation is to make a looped flow tube (which is currently just being used as an input/output supply path) with larger sites of the active area for electrochemical reactions. This will enable the development of a battery system that can

become an energy distribution system much like what has been used in direct methanol fuel cell (DMFC) systems [139, 140]. This has many advantages over conventional lumped systems such as lithium-ion batteries. The results will be 1) reduction of the charging time for a battery by refueling like a conventional combustion vehicle [141], 2) more efficient utilization of space since the battery system could be embedded into the structure of the vehicle, 3) independent control of power and energy, where power can be increased by using a larger loop that winds through the structure of the vehicle, and energy can be increased by increasing the size of the fuel tank and electrolyte concentration [133, 137, 140, 142], and 4) significantly improved battery cycle life because the system will not involve any mechanical degradation mechanisms such as the large volume change that are characteristic of high-energy lithium-ion batteries [141, 143, 144]. Recently, novel redox species of aqueous and non-aqueous systems have been explored to overcome the issue of low energy density and to improve the cell's potential upper limit [145-148]; these new materials can also be applied in the proposed system. Figures 1.2(a), 1.2(b), and 1.2(c) are the VRFB schematic diagrams of a novel tubular cell, a half PVC planar cell, and a half traditional cell, respectively.

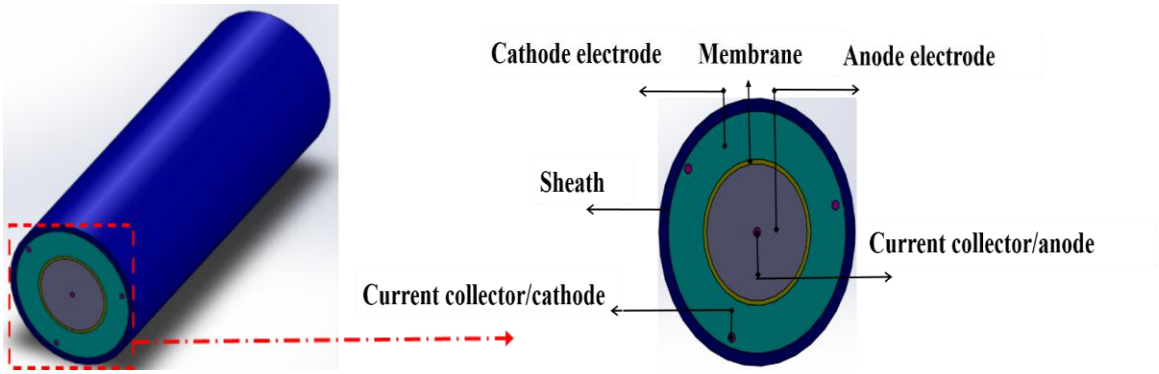

(a)

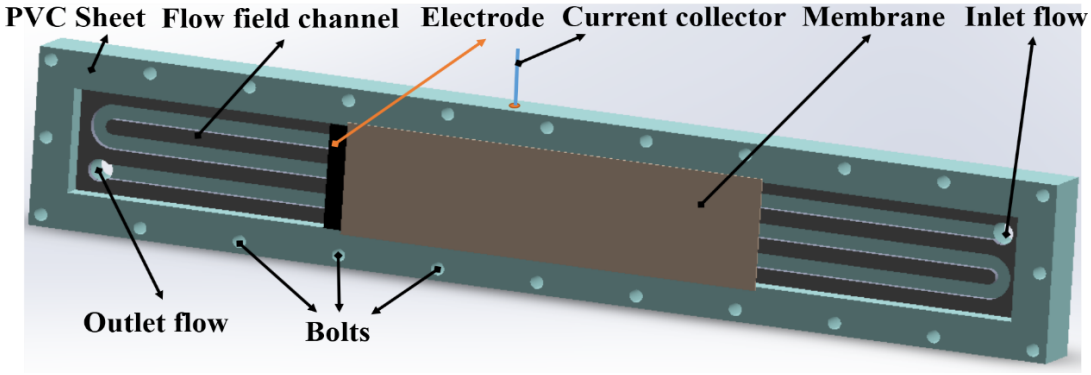

(b)

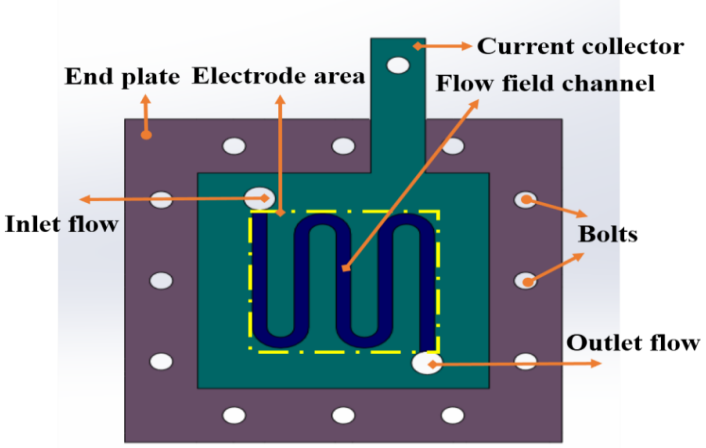

(c)

Figure 1.2. Schematic diagrams of the proposed distributed and traditional flow cells. (a) Tubular cell, (b) Half PVC planar cell, (c) Half traditional cell.

2. ACTUAL ELECTRODE AREA ANALYSIS

A simple analytical analysis of a single VRFB cell is adopted in a similar way to the DMFC system [140]. This analysis reveals that the tubular VRFB cell can have larger electrochemical active area than the planar cell under specific geometry conditions for same total volume, which eventually leads to higher output current and power. Figure 2.1 shows the 2D tubular (left) and planar (right) cells under the assumption of having same characteristic length ($L = L_{tubular} = L_{planar}$) and total volume (V).

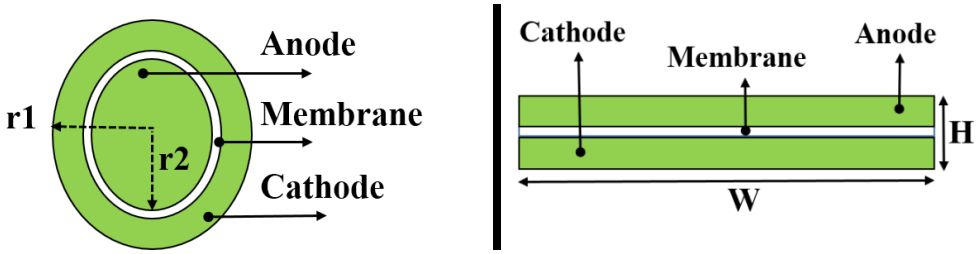

Figure 2.1. A 2D front-view drawing of the active area of two cells (left: tubular cell, right: planar cell).

The total volume of each configuration can be expressed as follows:

$$V = \pi r^2 L = w h L \quad (1)$$

where r is the outer radius of the tubular cell, which can be formulated in the following form:

$$r = \sqrt{\frac{h w}{\pi}} \quad (2)$$

Now, the ratio of the active area to the total volume of the tubular cell to the same ratio of the planar cell is presented as follows:

$$\frac{(A_{active}/V)_{tubular}}{(A_{active}/V)_{planar}} = \frac{2\pi\, r\, L_{tubular}}{w\, L_{planar}} \tag{3}$$

Substituting Eq. (2) into Eq. (3) leads to the following final formula:

$$\frac{(A_{active}/V)_{tubular}}{(A_{active}/V)_{planar}} = 2\sqrt{\pi}\left(\sqrt{\frac{h}{w}}\right) \tag{4}$$

By utilizing Eq. (4), the tubular cell can have larger active surface area than the planar cell under the following specific geometry condition:

$$\frac{w}{h} < 4\pi \tag{5}$$

This geometric condition is reasonable for small-scale cells in portable applications, which reflects the importance of tubular configuration to provide more electrode surface area compared to the planar cell.

3. THE EXPERIMENTAL APPROACH DETAILS

In this study, two single cells as distributed VRFB and a third traditional cell have been experimentally performed. First, the tubular cell (TC) was constructed, which consisted of a proton exchange membrane, electrodes, electrolyte distributors (nozzles), and current collectors. The proton exchange membrane was constructed out of Nafion 212 (15 x 15 cm in area with a thickness of 25.7 μm, Fuel Cell Store, Texas, USA). The electrodes were composed out of graphite felt (GFA6, SGL Technologies GmbH), where the cathode and anode had uncompressed thicknesses of 3 mm and 6 mm respectively. The graphite felt making up the anode has dimensions of 3.5 x 12 cm, while the cathode had dimensions of 7 x 12 cm, making both electrodes the same volume (25.2 cm^3). Two nozzles constructed out of PVC material were used as electrolyte distributors, where one nozzle can separately deliver the catholyte and anolyte to each respective electrode, and the other can return the electrolytes into their tanks. One graphite rod (McMaster-Carr, 1/4 in. thickness, and 2.5 in. side length) was inserted into the anode (inner side), while two rods were inserted into the cathode (outer side), which served as the current collector. Each rod was attached to the polytetrafluoroethylene (PTFE) wrapped copper wires to allow current to leave/enter the cell. These components were then systematically assembled to create the tubular cell. The graphite felt making up the anode was first rolled into a tubular shape and then firmly wrapped in the proton exchange membrane three times to separate the anolyte and catholyte electrolytes. The graphite felt making up the cathode was then rolled around the anode–membrane assembly to form the equivalent of a cell stack. The stack assembly was then inserted into a vinyl tube that would act as the outer wall of the cell. The membrane was then attached to the inner nozzles of the

electrolyte distributors in such a way to prevent electrolyte mixing. The outer vinyl tube was then attached with PVC glue to the outer nozzles of the electrolyte distributors to prevent air penetration, thus forming the completed cell assembly. The second cell refers to the long cell (LC), in which a thermoplastic material PVC from McMaster-Carr was used to replace the graphite plate in traditional VRFB cells. The outer dimension of the half PVC cell was 27.5 × 4.8 cm with 1.27 cm thickness. The graphite felt electrode, 25.5 × 2.8 cm with 6 mm thickness, sat inside an engraved rectangular pocket in the main PVC sheet. Proton exchange membrane (Nafion 117 with 0.183 mm thickness, Fuel Cell Store, Texas, USA) was used to separate the two different electrolytes and to allow only proton passing. Also, a pure compressible graphite sheet of 1/16 in. thickness from McMaster-Carr was used to serve two functions, as flow field channels and current collector. The flow field had three channels of 4 × 1.6 mm^2 cross section areas with a land width of 4 mm among the channels, which was machined by water-jet technique. Each half cell had one copper wire, which was rolled around part of the compressible graphite sheet inside the cell and then wrapped with PTFE tape. Afterwards, the wire was pulled out to connect the battery tester terminals for the measurements. The depth of the PVC pocket was 6.6 mm, and it was purposely made less than the sum of the original electrode and flow channel thicknesses to accomplish approximately 16.5% compression ratio, where the graphite felt electrode compression ratio was limited to 1 mm. The two cell halves were combined together with a total of 24 stainless steel bolts distributed in a uniform way along the PVC boundary to make a compact cell with no leaking. The last cell stood for the traditional design (TD) cell, the most common VRFB cell in literature, where the serpentine flow channels cut in a graphite plate. The cell was composed of

almost the same components of LC design except the electrode and membrane dimensions (5 × 5 cm^2), including PTFE (polytetrafluoroethylene) gaskets and electric insulators from McMaster-Carr, USA to avoid electrolyte leakage among the assembled components and to prevent electronic current to go away from the flow field plate to endplates. Two Garolite sheets from Fuel Cell Store, Texas, USA were used as endplates with 12 × 12 cm^2 outer dimensions to offer excellent strength and good electrical insulation with a total of 12 bolts distributed in a uniform way along the endplate boundary to compact the cell components with no leaking. A high-density polyethylene (HDPE) material for tubing, compression fittings (1/8 NPT × 1/4 in. OD tube), and tanks was used to feed the electrolyte solution into the cell stack from external tanks and vice versa by two pumps. Figures 3.1(a), 3.1(b), and 3.1(c) show the assembled tubular, PVC planar, and traditional cells with their experimental units, respectively.

For all VRFB prototypes, the electrolyte solution of vanadium (V^{+4}) was prepared in lab temperature ~24 ^oC via dissolving 1.04 M $VOSO_4.xH_2O$ (99.9% wt. purity, Alfa Aesar) in 4 M sulphuric acid solution. After fully charging the two cells, the amount of anolyte and catholyte of both cells was 100 ml in each tank. Both the anolyte and catholyte were pumped to the cell electrodes by two pumps (SMART Digital DDA7.5-16AR-PVC/V/C, Grundfos, Bjerringbro, Germany) from tanks and vice versa. The upper and lower limits during charging/discharging operations were set to 1.7 V and 1 V, respectively, by using the constant current method. A fully charged condition was held when the cell was first charged at constant current, 500 mA, until reaching 1.75 V cell voltage, then further charging was conducted at constant voltage 1.75 V until the current dropped to 40 mA. In the first charging (where 100 ml of V^{4+} electrolyte solutions was

placed in anode side tank and 200 was placed in cathode side tank for all cells), V^{4+} was transformed into V^{5+} and V^{2+} in both solutions (catholyte and anolyte for all cells, respectively). Afterwards, half of the catholyte amount was taken away after observing new colors on both sides (i.e., violet in the anode side and yellow on the cathode side). The voltage was recorded after each time period (20 seconds) in cycling tests. All the test measurements, including charging/discharging plots, polarization curves, and impedance analysis data were performed with (4 Channel Battery Analyzer, BST8-20A-CST, MTI Corporation, CA 94804, USA) at different operating conditions. The obtained results are discussed below.

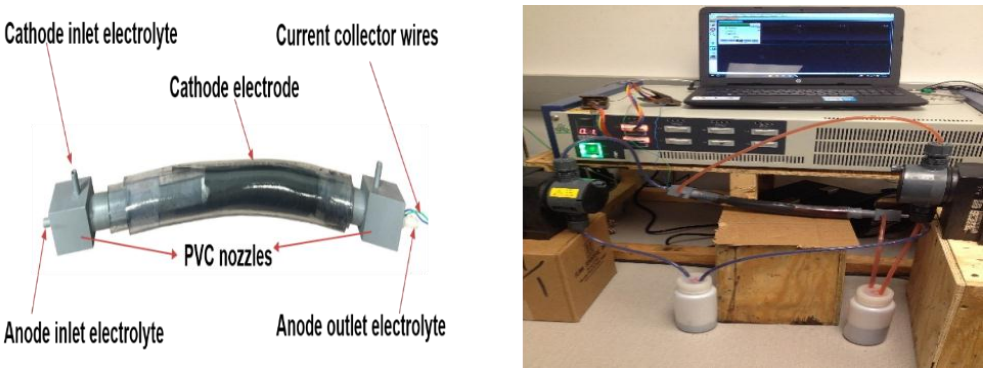

(a)

Figure 3.1. The assembled cells with their experimental units. (a) TC cell, (b) LC cell, (c) TD cell.

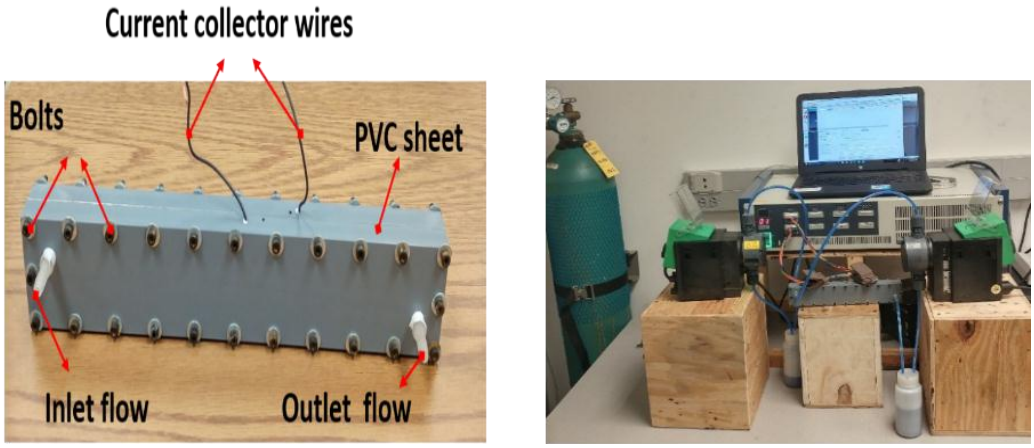

(b)

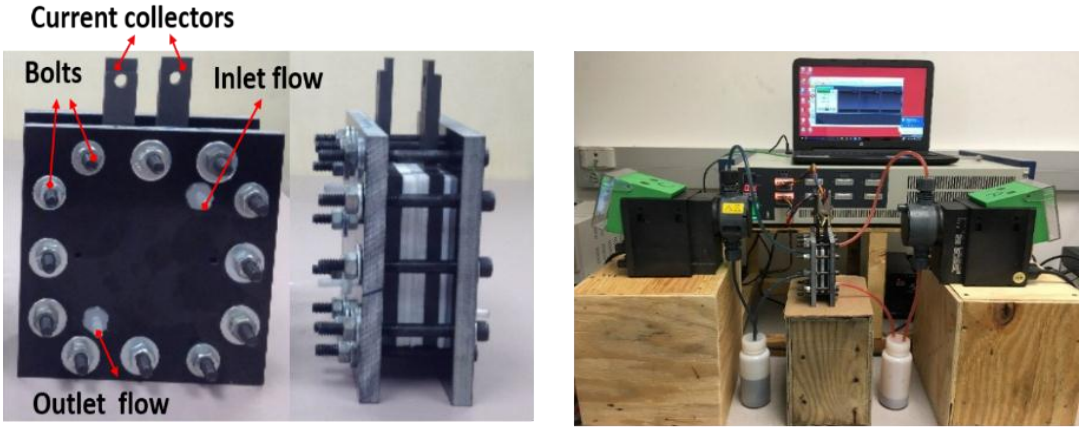

(c)

Figure 3.1. The assembled cells with their experimental units. (a) TC cell, (b) LC cell, (c) TD cell (cont.).

4. RESULTS

4.1. CYCLING PERFORMANCE

The cycling test is able to show the long-term capacity and efficiency loss due to self-discharge and side reactions, and it can also partially reflect battery activation loss [110, 111]. Charging/discharging tests for all cells were conducted using the same test equipment to investigate their performance. The cycling currents were 750 mA for the TC cell and 500 mA for the LC and TD cells at 35 ml/min volumetric flow rate. The charging and discharging voltage limits were 1.7 V and 0.9 V for the TC cell and 1.7 V and 1 V for the LC and TD cells. Figures 4.1(a), 4.1(b), and 4.1(c) present the cyclic behaviors of the units TC, LC, and TD, respectively. All prototypes show stable and high electrochemical reversibility performance under repeated cycles (four cycles) at the aforementioned experimental conditions. A single charge and discharge potential plateau was observed, indicating that a single reaction occurred in each half-cell of the flow battery. However, it was observed that the total run time to achieve four cycles of the TC cell was less than the other cells. The fast decrease in time of TC cell was mainly associated with the higher applied current during cycling, 750 mA, which can reduce the cell capacity, and to the large contact resistance among cell components, leading to higher ohmic resistance. Although the same current, 500 mA, was applied in TD and LC cells, the discharge capacity time of TD was less than LC, which can be attributed to the vanadium penetration (shortage in vanadium concentration) through the porous graphite plate during the four-cycle test.

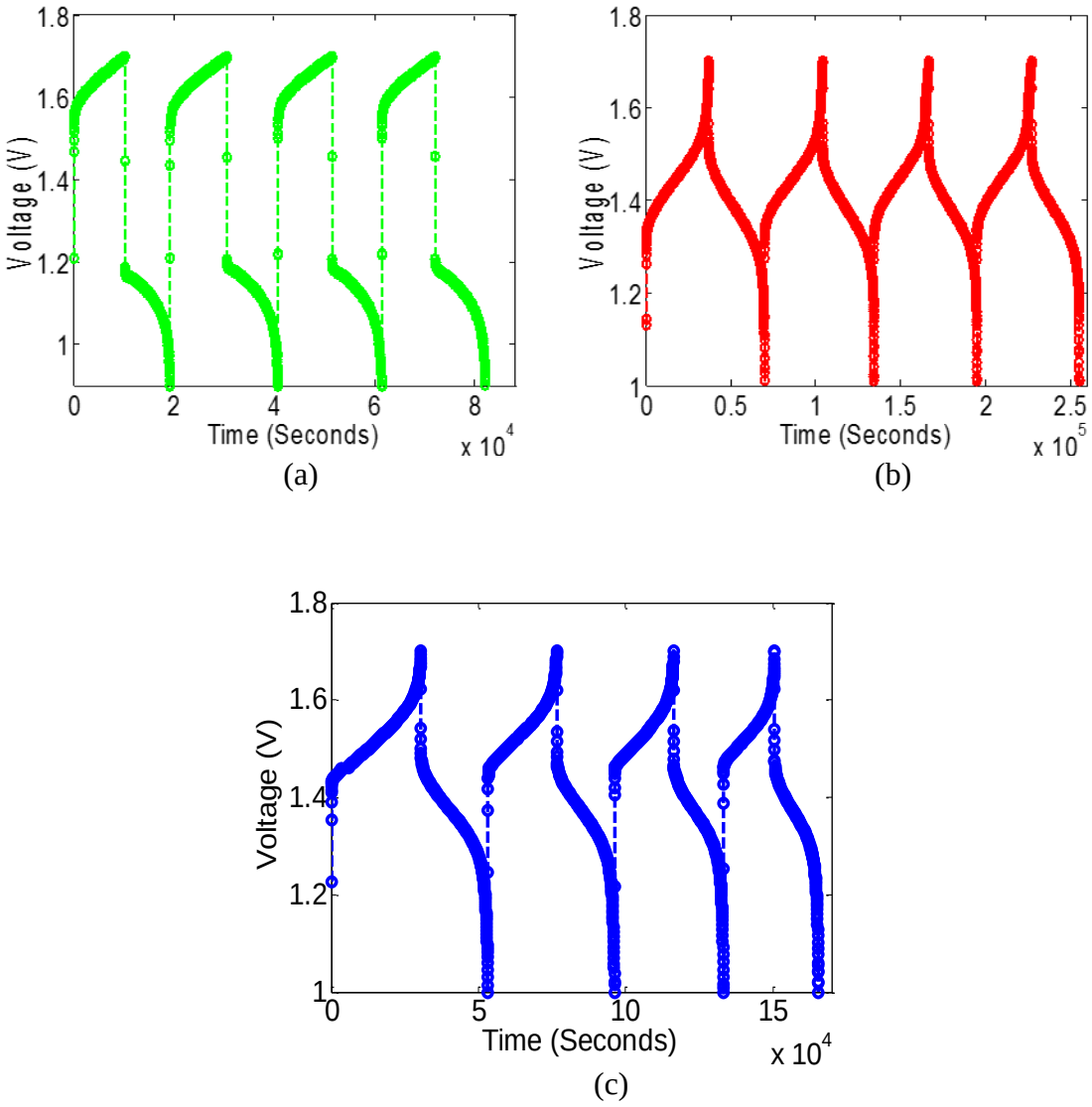

Figure 4.1. Charge/discharge curves over four cycles (a) TC cell, (b) LC cell, and (c) TD cell.

Columbic efficiency (CE), voltage efficiency (VE), and energy efficiency (EE) are considered to be among the common features that can detect the VRFB performance through cycling tests [23, 149-152], which are defined as follows:

The CE represents the ratio of the actual amount of charges used during the discharge process to the actual charges used during the charging process:

$$CE = \frac{\int_0^{t_d} I_{discharge}\, dt}{\int_0^{t_c} I_{charge}\, dt} \quad (6)$$

where t_c is charging time and t_d is discharging time. Having a very low vanadium permeability membrane can lead to ~100% CE [137, 153-157].

The VE represents the ratio of the average discharge voltage to the average charge voltage:

$$VE = \frac{\int_0^{t_d} I_{discharge}\, E_{discharge}\, dt}{\int_0^{t_c} I_{charge}\, E_{charge}\, dt} \quad (7)$$

The EE equals the product of VE and CE:

$$EE = VE \times CE \quad (8)$$

Figure 4.2 illustrates the average CE, VE, and EE of the TC, LC, and TD cells over four cycles at the aforementioned operating conditions. It is obvious that the TC cell has less average voltage and energy efficiencies (70.25% and 64.43%) compared to the other two cells, LC and TD, (90.12%, 83.12% and 88.54%, 74.84%, respectively) due to the high contact resistance among the cell components. In addition, lower CE was obtained in the TD cell (84.52% compared to 92.23% and 91.71% for the LC and TC cells, respectively), due to the lost amount of vanadium penetration through the porous graphite plate.

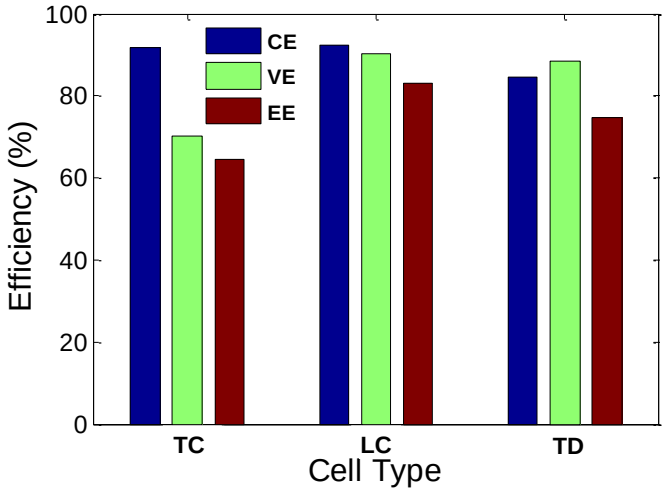

Figure 4.2. Charge/discharge average efficiency over four cycles for LC, TC, and TD cells.

A typical single charge/discharge cycle test at a range of current values was also conducted to further evaluate the applicability of the new distributed VRFB designs, as shown in Figures 4.3(a) and 4.3(b) for the TC and LC cells, respectively. It can be seen for all cells that increasing the current decreases the charge/discharge time (capacity) in a dramatic way, which reflects the normal behavior of all battery systems. At higher currents, the capacity decay can be related to the increase in overpotential losses as a result of the fast charging and discharging rates, which lowers the desired potential value. Table 4.1 also presents the corresponding CE, VE, and EE at each applied current, and it clearly shows that increasing current results in higher CE values due to the high rate of electrolyte consumption, which in turn minimizes the electrolyte crossover through the membrane [137, 142, 150, 152, 155, 157]. Higher ohmic overpotential losses can also be obtained as current increases [113], which results in lower VE values. Since CE increases at a rate less than the decreasing rate of VE, EE decreases as current increases. As discussed above, the values of VE (the main factor in finding EE) and EE in the TC cell

were less than in the LC cell at the applied current range (shown in Table 4.1) of the single charge/discharge test.

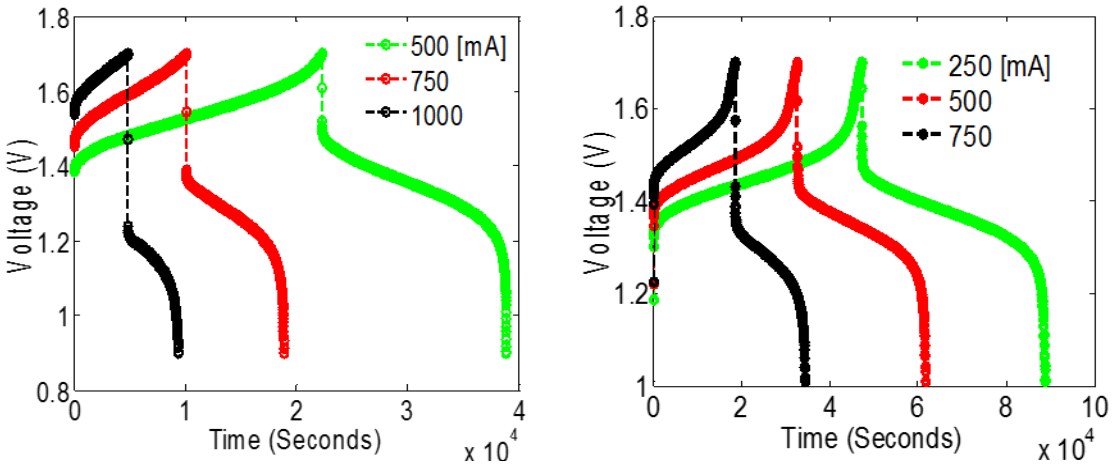

Figure 4.3. Typical single charge/discharge curves as a function of the current for VRFB cells. (a)TC, (b) LC.

Table 4.1. Efficiencies of the single TC and LC VRFB cells.

Current (mA)		**CE (%)**		**VE (%)**		**EE (%)**	
TC	**LC**	**TC**	**LC**	**TC**	**LC**	**TC**	**LC**
500	250	92.891	92.214	72.365	92.865	67.220	83.790
750	500	94.369	94.165	68.124	86.358	64.288	81.319
1000	750	95.956	95.565	63.659	80.963	61.084	77.372

4.2. POLARIZATION MEASUREMENTS

The discharge polarization curves are plots of the flow cell potential under a range of applied currents to identify the main three regions of losses. Figure 4.4(a) (left and right) compares the discharge polarization and corresponding power data, respectively, of the three cells at 1 ml/min flow rate. All the tests were conducted at fully charged conditions (charging the cell at 1.7 V until 40 mA steady state current was obtained). Regardless of the different actual electrode areas used in all cells, it can be seen that the TC cell suffers from a quick potential drop due to the high overpotential losses, which becomes more significant at high current values. Since the LC cell has higher electrode surface area and lower overpotential losses (higher VE), the maximum obtained current (5500 mA) is much higher than the current in the TC and TD cells, 3250 and 2250 mA, respectively.

The new distributed flow cells, TC and LC, were further investigated by studying the electrolyte transport effect on the cell potential and corresponding power measurements under a range of flow rates, as shown in the Figures 4.4(b) and 4.4(c), respectively. A high flow rate can obviously increase the maximum current (reduce the mass transport overpotential effect) by bringing more active species onto the electrode surface to support the redox reaction. It is noticed that the limiting current can be increased (from 3250 to 3750 mA) in the TC cell and (from 5550 to 8250 mA) in the LC cell at an analog range of flow rates from 1 to 45 ml/min.

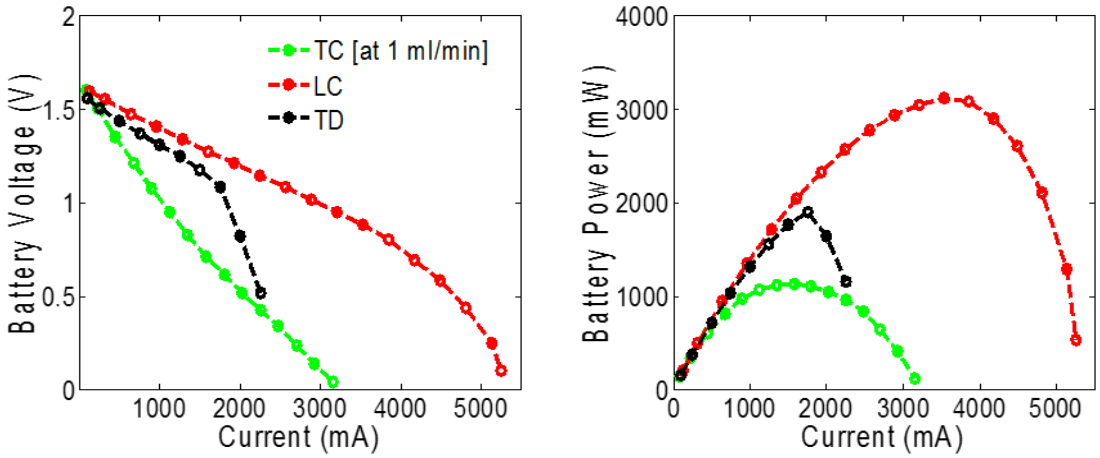

(a)

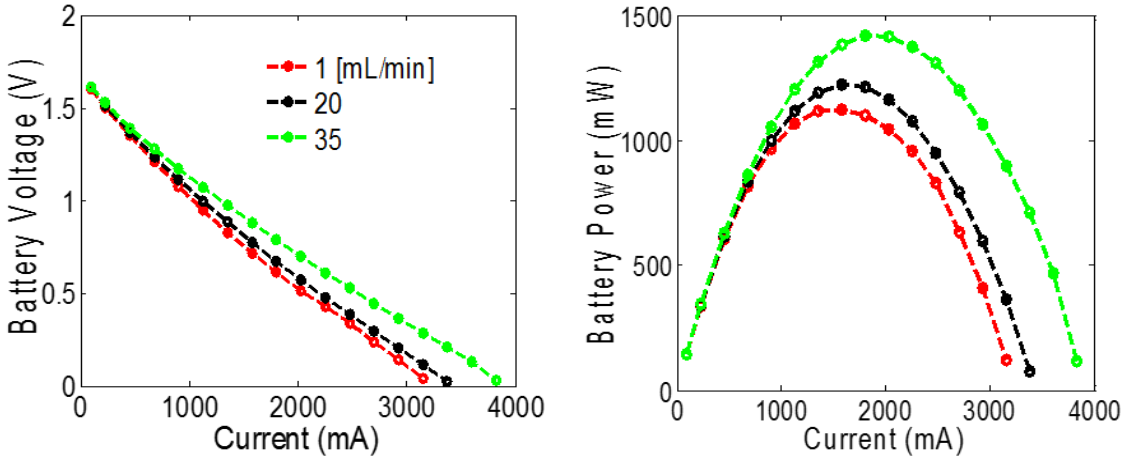

(b)

Figure 4.4. Measured polarization curves. (a) Potential polarization (left) and corresponding power (right) for the TC, LC, and TD cells at 1 ml/min flow rate, (b) Same of (a) but for cell TC at a range of flow rates, and (c) Same of (a) but for cell LC only.

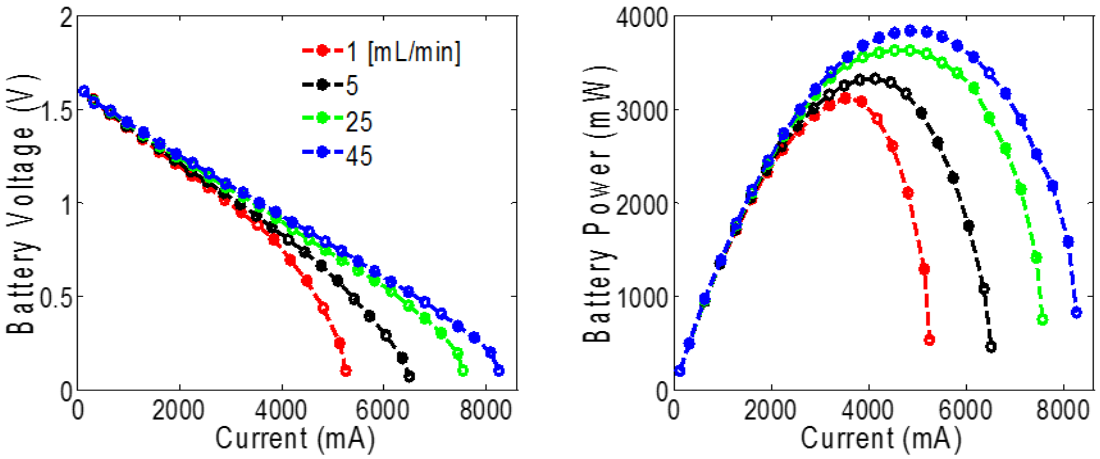

(c)

Figure 4.4. Measured polarization curves. (a) Potential polarization (left) and corresponding power (right) for the TC, LC, and TD cells at 1 ml/min flow rate, (b) Same of (a) but for cell TC at a range of flow rates, and (c) Same of (a) but for cell LC only (cont.).

4.3. ELECTROCHEMICAL IMPEDANCE TEST ANALYSIS

An electrochemical impedance spectroscopy test under fully charged condition at 35 ml/min was conducted to characterize the full voltage losses of the three cells. The Nyquist impedance was plotted in Figure 4.5 over an AC frequency range of 20 kHz to 0.01 Hz and with 10 mV perturbation amplitude, where a circuit diagram model R(CR)(CRW) was implemented to fit the original data [118]. The high-frequency intercept with the real axis (Z_1) corresponded to all ohmic processes in the battery, which includes both the ionic and electronic resistance in the graphite electrode in addition to the ionic resistance from charge transfer through the membrane. It is obvious that the TC cell has higher ohmic resistance (0.5 Ω) compared to LC and TD cells (0.178 and 0.135 Ω, respectively), which explains the lower VE of TC due to the high contact resistance among cell components. The impedance measurement of the TC cell also shows much

higher kinetic overpotential (charge transfer in porous electrode), which is represented by the large semicircle compared to the small semicircle in LC and TD cells likely due to cell assembly.

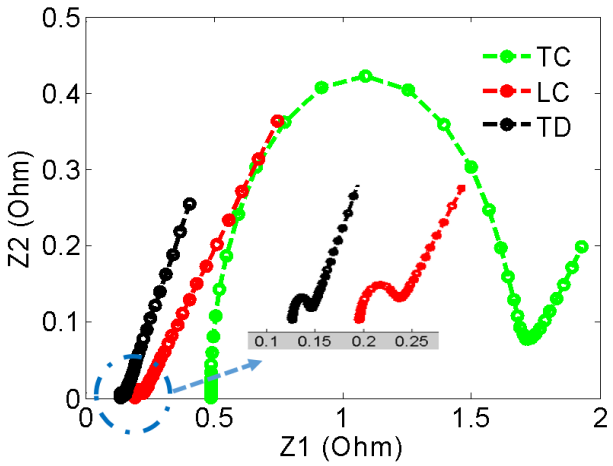

Figure 4.5. Impedance measurements comparison of the TC, LC, and TD cells.

5. CONCLUSIONS

Most flow batteries were targeted for stationary applications, and one of the most important issues in their development was enhancing power density. In this paper, a new concept of distributed VRFB has been introduced through designing and testing two single VRFB cells (tubular and long PVC planar cells) configured for distribution in a transport system. An analytical study has been also performed for the tubular and planar cells and it has shown that under certain geometric conditions, tubular cell can utilize larger electrode active areas than planar shapes, leading to higher power density.

Many tests have been conducted to evaluate the new design's performance compared to the traditional design. The results showed that the tubular cell has lower VE and EE than the other cells in addition to a quick drop of polarization potential, which needs to be further improved by reducing the high contact resistance among cell components, applying uniform pressure to the anode and cathode sides, and using a flow field channel to minimize the concentration overpotential. The tubular design issues were solved by introducing a long PVC planar cell, which shows very stable cycling performance with better VE and EE compared to the existing ones. The flow rate impact in polarization tests has also been investigated, and it shows that a higher circulation rate reduces the mass transport polarization.

REFERENCES

1. Barton, J.P. and D.G. Infield, *Energy storage and its use with intermittent renewable energy.* IEEE transactions on energy conversion, 2004. 19(2): p. 441-448.

2. Blarke, M.B. and H. Lund, *The effectiveness of storage and relocation options in renewable energy systems.* Renewable Energy, 2008. 33(7): p. 1499-1507.

3. Chen, H., et al., *Progress in electrical energy storage system: A critical review.* Progress in Natural Science, 2009. 19(3): p. 291-312.

4. Denholm, P., et al., *The Role of energy storage with renewable electricity generation.* 2010.

5. Divya, K.C. and J. Østergaard, *Battery energy storage technology for power systems—An overview.* Electric Power Systems Research, 2009. 79(4): p. 511-520.

6. Evans, A., V. Strezov, and T.J. Evans, *Assessment of utility energy storage options for increased renewable energy penetration.* Renewable and Sustainable Energy Reviews, 2012. 16(6): p. 4141-4147.

7. Hadjipaschalis, I., A. Poullikkas, and V. Efthimiou, *Overview of current and future energy storage technologies for electric power applications.* Renewable and Sustainable Energy Reviews, 2009. 13(6-7): p. 1513-1522.

8. Sharma, A., et al., *Review on thermal energy storage with phase change materials and applications.* Renewable and Sustainable Energy Reviews, 2009. 13(2): p. 318-345.

9. Yang, Z., et al., *Electrochemical energy storage for green grid.* Chem Rev, 2011. 111(5): p. 3577-613.

10. Kanase-Patil, A.B., R.P. Saini, and M.P. Sharma, *Integrated renewable energy systems for off grid rural electrification of remote area.* Renewable Energy, 2010. 35(6): p. 1342-1349.

11. Hafez, O. and K. Bhattacharya, *Optimal planning and design of a renewable energy based supply system for microgrids.* Renewable Energy, 2012. 45: p. 7-15.

12. Carrasco, J.M., et al., *Power-electronic systems for the grid integration of renewable energy sources: A survey.* IEEE Transactions on industrial electronics, 2006. 53(4): p. 1002-1016.

13. Turner, J.A., *A Realizable Renewable Energy Future.* Science, 1999. 285(5428): p. 687-689.

14. Alotto, P., M. Guarnieri, and F. Moro, *Redox flow batteries for the storage of renewable energy: A review.* Renewable and Sustainable Energy Reviews, 2014. 29: p. 325-335.

15. Fabjan, C., et al., *The vanadium redox-battery: an efficient storage unit for photovoltaic systems.* Electrochimica Acta, 2001. 47(5): p. 825-831.

16. Joerissen, L., et al., *Possible use of vanadium redox-flow batteries for energy storage in small grids and stand-alone photovoltaic systems.* Journal of Power Sources, 2004. 127(1-2): p. 98-104.

17. Kear, G., A.A. Shah, and F.C. Walsh, *Development of the all-vanadium redox flow battery for energy storage: a review of technological, financial and policy aspects.* International Journal of Energy Research, 2012. 36(11): p. 1105-1120.

18. RYCHCIK, M. and M. SKYLLAS-KAZACOS*, *Characteristics of a new all-vanadium redox flow battery.* Journal of Power Sources 1988. 22(1): p. 59-67.

19. Painuly, J.P., *Barriers to renewable energy penetration; a framework for analysis.* Renewable energy, 2001. 24(1): p. 73-89.

20. Leung, P., et al., *Progress in redox flow batteries, remaining challenges and their applications in energy storage.* RSC Advances, 2012. 2(27): p. 10125.

21. Aaron, D.S., et al., *Dramatic performance gains in vanadium redox flow batteries through modified cell architecture.* Journal of Power Sources, 2012. 206: p. 450-453.

22. Wang, W., et al., *Recent progress in redox flow battery research and development.* Advanced Functional Materials, 2013. 23(8): p. 970-986.

23. Kumar, S. and S. Jayanti, *Effect of flow field on the performance of an all-vanadium redox flow battery.* Journal of Power Sources, 2016. 307: p. 782-787.

24. Chen, J.Q., B.G. Wang, and H.L. Lv. *Numerical simulation and experiment on the electrolyte flow distribution for all vanadium redox flow battery*. in *Advanced Materials Research*. 2011. Trans Tech Publ.

25. Zhang, C., et al., *Effects of operating temperature on the performance of vanadium redox flow batteries.* Applied Energy, 2015. 155: p. 349-353.

26. Aaron, D., et al., *Polarization curve analysis of all-vanadium redox flow batteries.* Journal of Applied Electrochemistry, 2011. 41(10): p. 1175-1182.

27. Shao, Z.-G., et al., *A tubular direct methanol fuel cell with Ti mesh anode.* Journal of Power Sources, 2006. 160(2): p. 1003-1008.

28. Ward, T., X. Li, and A. Faghri, *Performance characteristics of a novel tubular-shaped passive direct methanol fuel cell.* Journal of Power Sources, 2011. 196(15): p. 6264-6273.

29. ZIMMERMAN, N., *VANADIUM REDOX FLOW BATTERY Sizing of VRB in electrified heavy construction equipment.* 2014.

30. Houser, J., et al., *Influence of architecture and material properties on vanadium redox flow battery performance.* Journal of Power Sources, 2016. 302: p. 369-377.

31. Zhang, Y., C.-Y. Wang, and X. Tang, *Cycling degradation of an automotive LiFePO4 lithium-ion battery.* Journal of Power Sources, 2011. 196(3): p. 1513-1520.

32. Ebner, M., et al., *Visualization and quantification of electrochemical and mechanical degradation in Li ion batteries.* Science, 2013. 342(6159): p. 716-20.

33. Pan, F. and Q. Wang, *Redox Species of Redox Flow Batteries: A Review.* Molecules, 2015. 20(11): p. 20499-20517.

34. Liu, Q., et al., *Non-aqueous vanadium acetylacetonate electrolyte for redox flow batteries.* Electrochemistry Communications, 2009. 11(12): p. 2312-2315.

35. Brushett, F.R., J.T. Vaughey, and A.N. Jansen, *An All-Organic Non-aqueous Lithium-Ion Redox Flow Battery.* Advanced Energy Materials, 2012. 2(11): p. 1390-1396.

36. Palomares, V., et al., *Na-ion batteries, recent advances and present challenges to become low cost energy storage systems.* Energy & Environmental Science, 2012. 5(3): p. 5884-5901.

37. Watt-Smith, M.J., et al., *The importance of key operational variables and electrolyte monitoring to the performance of an all vanadium redox flow battery.* Journal of Chemical Technology and Biotechnology, 2013. 88(1): p. 126-138.

38. Skyllas-Kazacos, M., et al., *Characteristics and performance of 1 kW UNSW vanadium redox battery.* Journal of Power Sources, 1991. 35(4): p. 399-404.

39. Baccino, F., et al., *Experimental testing procedures and dynamic model validation for vanadium redox flow battery storage system.* Journal of Power Sources, 2014. 254: p. 277-286.

40. Rahman, F. and M. Skyllas-Kazacos, *Vanadium redox battery: Positive half-cell electrolyte studies.* Journal of Power Sources, 2009. 189(2): p. 1212-1219.

41. Shah, A.A., et al., *A dynamic unit cell model for the all-vanadium flow battery.* Journal of the Electrochemical society 2011. 158(6): p. A671-A677.

42. Xiao-gang, L., et al., *Electrochemical behavior of diverse vanadium ions at modified graphite felt electrode in sulphuric solution.* Journal of Central South University of Technology, 2007. 14: p. 51-56.

43. Al-Fetlawi, H., A.A. Shah, and F.C. Walsh, *Non-isothermal modelling of the all-vanadium redox flow battery.* Electrochimica Acta, 2009. 55(1): p. 78-89.

44. Jia, C., J. Liu, and C. Yan, *A significantly improved membrane for vanadium redox flow battery.* Journal of Power Sources, 2010. 195(13): p. 4380-4383.

45. Mai, Z., et al., *Nafion/polyvinylidene fluoride blend membranes with improved ion selectivity for vanadium redox flow battery application.* Journal of Power Sources, 2011. 196(13): p. 5737-5741.

46. Qiu, G., et al., *3-D pore-scale resolved model for coupled species/charge/fluid transport in a vanadium redox flow battery.* Electrochimica Acta, 2012. 64: p. 46-64.

47. Shah, A.A., H. Al-Fetlawi, and F.C. Walsh, *Dynamic modelling of hydrogen evolution effects in the all-vanadium redox flow battery.* Electrochimica Acta, 2010. 55(3): p. 1125-1139.

48. Xu, W., et al., *Membranes with well-defined ions transport channels fabricated via solvent-responsive layer-by-layer assembly method for vanadium flow battery.* Sci Rep, 2014. 4: p. 4016.

49. Hwang, G.-J. and H. Ohya, *Crosslinking of anion exchange membrane by accelerated electron radiation as a separator for the all-vanadium redox flow battery.* Journal of Membrane Science, 1997. 132(1): p. 55-61.

50. Song, J., S. Cha, and W. Lee, *Optimal composition of polymer electrolyte fuel cell electrodes determined by the AC impedance method.* Journal of Power Sources, 2001. 94(1): p. 78-84.

SECTION

2. SUMMARY AND FUTURE WORK

2.1. SUMMARY

The interest in electrical energy storage has grown substantially in the last few decades. Industry, research, and also communities have been triggered by the growing demand of energy, the finite sources of fossil fuels, and the increasing pollution caused by fossil fuels to develop and improve electrical energy storage from renewable power sources. Electrical storage systems can be categorized in three major sections: a) mechanical b) capacitative (no redox couples involved) and c) electrochemical systems (Table 2.1).

Table 2.1 Energy Storage Systems.

Mechanical	**Capacitative**	**Electrochemical**
Pumped Hydro	Super Capacitors	Batteries
Compressed Air		Redox Flow Batteries
Fly Wheels		Fuel Cells

Only the electrochemical section can be implemented to both mobile and stationary applications with large energy storage capabilities. However, the existing systems show several major drawbacks that need to be solved. Some of these drawbacks are the small amount of energy density that can be utilized, the weight and the limited space of the system (regarding mobile applications), and the costs of some components.

In this work, new cost-effective and efficient designs (a PVC-based flow field plate and distributed VRFB system of tubular-shaped cells) have been evaluated to develop a suitable energy storage system with highly improved components for stationary energy storage applications and for portable purposes at specific geometric conditions.

- Chapter 1 discusses the need of energy storage systems and their types. Among the many available technologies, VRFB is an attractive solution, both economically and technically, for large stationary storage applications. Also, fundamental electrochemistry, VRFB component materials, system design, and the governing equations of the multiphysics model are discussed.
- Chapter 2 presents a 3D multidisciplinary detailed model based on electrochemistry and fluid mechanics by including a single passage of serpentine channel at different heights. Then, the single pass model is verified with a whole flow field serpentine channel model at different ranges of operating conditions, volumetric flow rates, and applied currents. In general, the convective mass transport improves as the flow velocity increases. This model is able to investigate the impact of channel height on the system performance and overall battery efficiency at different load conditions. Thickness of the flow channel on the mass flow penetration into the porous layer is discussed as well.
- Chapter 3 introduces a new cost-effective and efficient single-cell VRFB design with an embedded serpentine flow field channel, which is fabricated and tested experimentally in our laboratory. The new design is safe, lightweight, requires less number of components (i.e., no need for gaskets, insulators, graphite plates, and end plates), and easy to assemble, with zero electrolyte permeation. In this

design, a new thermoplastic material, PVC (polyvinyl chloride), is used to replace the brittle and porous graphite flow field plate in the traditional VRFB. The cell performance is conducted under many tests such as cycling at different range of currents, polarization analysis, and electrochemical impedance spectroscopy (EIS) for resistance analysis. Then, the results are compared with the traditional VRFB cell, and it shows better columbic and energy efficiencies with less capacity degradation for the new design in addition to other benefits such as handling the cost and leakage issues.

- Chapter 4 develops for the first time two new types of distributed flow battery for transport systems (tubular-shaped and long PVC cells) that can be installed in electric vehicles or any other type of transport system that requires a clean power source. The length of both reaction cells is substantially greater than their width and it can be looped throughout the transport system in a serpentine configuration. In the tubular design, the membrane within the reaction cell has a length substantially equal to the length of the reaction cell such that surface area of the membrane is maximized relative to volume of the reaction cell to increase electrical power provided to an electrical load of the transport system. An analytical analysis of the two designs shows that the tubular design can result in larger active surface area than the long PVC cell for the same total volume and under specific geometric conditions, producing more output power. Different types of tests are conducted to study the cell's performance, and the results from the executive tests showed that both designs reflect the normal qualitative behavior of the traditional VRFB cell.

2.2. FUTURE WORK

The work of this dissertation focused on studying the channel height impact of the flow field on the overall performance of VRFB energy storage systems numerically, but also on investigating and developing new feasible design configurations as additional and/or alternative designs to the traditional VRFB. As a continuation of the present study, the following recommendations can be considered:

- A 3D non-isothermal model with different flow channel fields such as serpentine, interdigitated, and parallel should be developed to study the uniformity distribution of the electrolyte and the temperature distribution inside the porous electrode (it is important to avoid any kind of hotspots inside the electrode, which come from the uneven distribution of the electrolyte, where hotspots mean the temperature of the cell overcomes a limit value, then the vanadium ions start to precipitate, making the cell useless). Also, an experimental study of VRFB with flow field can be conducted to guarantee an even and homogeneous distribution of the electrolyte into the cell.
- Continuous numerical and then experimental work is required to design innovative flow cell configurations for uniform solution distribution at lower pressure drop to obtain higher limiting current density, power density, and overall efficiency, which means reducing the three sources of overpotential losses (activation, ohmic, and mass transport losses).
- The flow regime impact (laminar, transition, and turbulent) should be simulated at different Reynold number values on the mass transfer enhancement inside the porous electrode and the final VRFB performance.

- Despite the observed benefits of the new PVC-based cell and the tubular design, they still require additional work to minimize the contact resistance area between the current collector and the porous electrode. Reducing the contact resistance can be performed by either coating the rib area (space between channels) with a suitable composite and good electric conductive materials (carbon black or nano fiber composites) to enhance the electron movement externally and the electrochemical reaction internally, or by investigating a new configuration of the current collector that ensures lower contact resistance area. Improving the contact area produces higher current density and subsequently higher output power.
- A 3D numerical model of the tubular-shaped geometry design should be evaluated with and without including the flow field to study the VRFB cell performance. Also, a numerical comparison study of the planar and tubular VRFB cells can be investigated at different operating and geometry conditions to determine the optimal voltage performance and output power for both stationary and mobile purposes.
- Improving the performance of the current tubular-shaped design in such a way that more electrode area can be utilized (to produce larger power) by altering the orientation of the cell into vertical position or at specific angle degree. Also, a numerical and/or experimental study of adding flow field channels (to distribute the electrolyte in a uniform way along the inner (anode) and outer (cathode) cell sides) on the overall battery performance can be conducted.

REFERENCES

1. Dresselhaus, M. and I. Thomas, *Alternative energy technologies.* Nature, 2001. 414(6861): p. 332-337.

2. Reuters, T., *ISI web of knowledge.* Available in the internet at: http://apps. isiknowledge. com, 2011.

3. Chalk, S.G. and J.F. Miller, *Key challenges and recent progress in batteries, fuel cells, and hydrogen storage for clean energy systems.* Journal of Power Sources, 2006. 159(1): p. 73-80.

4. Blanc, C. and A. Rufer, *Understanding the vanadium redox flow batteries*. 2010: INTECH Open Access Publisher.

5. Blanc, C., *Modeling of a vanadium redox flow battery electricity storage system.* 2009.

6. De Leon, C.P., et al., *Redox flow cells for energy conversion.* Journal of Power Sources, 2006. 160(1): p. 716-732.

7. Moore, M., et al. *Sensitivity Analysis of Design Variables of an All-Vanadium Redox-Flow Battery*. in *Meeting Abstracts*. 2011. The Electrochemical Society.

8. Dunlap, R., *Sustainable energy*. 2014: Cengage Learning.

9. Ito, H., et al., *Effect of through-Plane Polytetrafluoroethylene Distribution in a Gas Diffusion Layer.* ECS Transactions, 2014. 64(3): p. 501-508.

10. Heinzel, A., et al., *Injection moulded low cost bipolar plates for PEM fuel cells.* Journal of Power Sources, 2004. 131(1): p. 35-40.

11. Mehta, V. and J.S. Cooper, *Review and analysis of PEM fuel cell design and manufacturing.* Journal of Power Sources, 2003. 114(1): p. 32-53.

12. Bullock, K.R., *Lead/acid batteries.* Journal of power sources, 1994. 51(1-2): p. 1-17.

13. Sudworth, J., *The sodium/sulphur battery.* Journal of power sources, 1984. 11(1-2): p. 143-154.

14. Scrosati, B. and J. Garche, *Lithium batteries: Status, prospects and future.* Journal of Power Sources, 2010. 195(9): p. 2419-2430.

15. Weber, A.Z., et al., *Redox flow batteries: a review.* Journal of Applied Electrochemistry, 2011. 41(10): p. 1137-1164.

16. de Boer, P. and J. Raadschelders, *Briefing Paper–Flow Batteries.* Leonardo Energy. Available on line at http://www. leonardo-energy. org/webfm_send/164, 2007.

17. Nguyen, T. and R.F. Savinell, *Flow batteries.* Electrochem. Soc. Interface, 2010. 19(3): p. 54.

18. de Boer, P. and J. Raadschelders, *Flow batteries.* Leonardo Energy, 2007: p. 1-9.

19. Kuan, H.-C., et al., *Preparation, electrical, mechanical and thermal properties of composite bipolar plate for a fuel cell.* Journal of Power Sources, 2004. 134(1): p. 7-17.

20. Alotto, P., M. Guarnieri, and F. Moro, *Redox flow batteries for the storage of renewable energy: A review.* Renewable and Sustainable Energy Reviews, 2014. 29: p. 325-335.

21. Tang, A., J. Bao, and M. Skyllas-Kazacos, *Dynamic modelling of the effects of ion diffusion and side reactions on the capacity loss for vanadium redox flow battery.* Journal of Power Sources, 2011. 196(24): p. 10737-10747.

22. Kjeang, E., et al., *High-performance microfluidic vanadium redox fuel cell.* Electrochimica Acta, 2007. 52(15): p. 4942-4946.

23. Rahman, F. and M. Skyllas-Kazacos, *Vanadium redox battery: Positive half-cell electrolyte studies.* Journal of Power Sources, 2009. 189(2): p. 1212-1219.

24. Larminie, J., A. Dicks, and M.S. McDonald, *Fuel cell systems explained*. Vol. 2. 2003: J. Wiley Chichester, UK.

25. Xi, J., et al., *Nafion/SiO 2 hybrid membrane for vanadium redox flow battery.* Journal of Power Sources, 2007. 166(2): p. 531-536.

26. Skyllas-Kazacos, M. and F. Grossmith, *Efficient vanadium redox flow cell.* Journal of the Electrochemical Society, 1987. 134(12): p. 2950-2953.

27. Rychcik, M. and M. Skyllas-Kazacos, *Characteristics of a new all-vanadium redox flow battery.* Journal of Power Sources, 1988. 22(1): p. 59-67.

28. Aaron, D., et al., *Polarization curve analysis of all-vanadium redox flow batteries.* Journal of Applied Electrochemistry, 2011. 41(10): p. 1175-1182.

29. Aaron, D., et al., *Dramatic performance gains in vanadium redox flow batteries through modified cell architecture.* Journal of Power sources, 2012. 206: p. 450-453.

30. Kaneko, H., et al., *Vanadium redox reactions and carbon electrodes for vanadium redox flow battery.* Electrochimica Acta, 1991. 36(7): p. 1191-1196.

31. Rychcik, M. and M. Skyllas-Kazacos, *Evaluation of electrode materials for vanadium redox cell.* Journal of Power Sources, 1987. 19(1): p. 45-54.

32. Zhou, H., et al., *A comparative study of carbon felt and activated carbon based electrodes for sodium polysulfide/bromine redox flow battery.* Electrochimica Acta, 2006. 51(28): p. 6304-6312.

33. Sun, C., et al., *Investigations on transfer of water and vanadium ions across Nafion membrane in an operating vanadium redox flow battery.* Journal of Power Sources, 2010. 195(3): p. 890-897.

34. Shah, A., H. Al-Fetlawi, and F. Walsh, *Dynamic modelling of hydrogen evolution effects in the all-vanadium redox flow battery.* Electrochimica Acta, 2010. 55(3): p. 1125-1139.

35. Fabjan, C., et al., *The vanadium redox-battery: an efficient storage unit for photovoltaic systems.* Electrochimica Acta, 2001. 47(5): p. 825-831.

36. Kong, C.S., et al., *Influence of pore-size distribution of diffusion layer on mass-transport problems of proton exchange membrane fuel cells.* Journal of Power Sources, 2002. 108(1): p. 185-191.

37. Larsson, A., *Evaluation of flow battery technology: An assessment of technical and economic feasibility*. 2009, Massachusetts Institute of Technology.

38. Yin, C., et al., *A coupled three dimensional model of vanadium redox flow battery for flow field designs.* Energy, 2014. 74: p. 886-895.

39. Qiu, G., et al., *Pore-scale analysis of effects of electrode morphology and electrolyte flow conditions on performance of vanadium redox flow batteries.* Journal of power sources, 2012. 219: p. 223-234.

40. Knehr, K., et al., *A transient vanadium flow battery model incorporating vanadium crossover and water transport through the membrane.* Journal of The Electrochemical Society, 2012. 159(9): p. A1446-A1459.

VITA

Mohammed Al-yasiri was born in Qulaat Sukar in Thi-Qar province, Republic of Iraq. He attended school in Qulaat Sukar before entering University of Science and Technology in Baghdad, Iraq. Mohammed earned his Bachelor (B.Sc.) and Master (M.Sc.) of Science degrees in Mechanical Engineering from University of Science and Technology/Baghdad, Iraq in May 2002 and 2005, respectively. His master's study focused on designing thermal energy storage in air-conditioning and refrigeration applications. In July 2006, he joined the Mechanical Engineering Department at Wassit University/Iraq. afterwards, he worked as a lecturer until December 2011. In Spring 2012, Mohammed went to Missouri University of Science and Technology in the United States, and in Spring 2013 started as a graduate student in the Mechanical and Aerospace Engineering Department. Mohammed joined the research group of Dr. Jonghyun Park in Spring 2015 to work under his supervision as a Ph.D. candidate. For his Ph.D. dissertation, Mohammed focused on building a 3D numerical model and developing new novel single cell designs of vanadium redox flow batteries (VRFBs) to improve their performance and to reduce the capital costs, which can help with their widespread commercialization. Mohammed was granted his second Master of Science (M.Sc.) degree in Mechanical Engineering from Missouri University of Science and Technology in Fall 2016. He received Doctor of Philosophy (Ph.D.) in Mechanical Engineering by the same University in May 2017. Mohammed Al-yasiri became a member of the Iraqi Engineers Association (IEA) in 2002. He also became a member of the American Society of Mechanical Engineers (ASME) and American Chemical Society (ACS) in 2014 and 2015, respectively.